Université de Lille 1 SCIENCES ET TECHNOLOGIES

THÈSE

Presentée en vue d'obtenir le grade de

DOCTEUR DE l'UNIVERSITE DE SCIENCE ET TECHNOLOGIES DE LILLE

Spécialité : **Génie Électrique**

Présentée par

Eric VEZZOLI

Thèse dirigée par **Betty LEMAIRE-SEMAIL et** codirigée par **Frédéric GIRAUD**

préparée au sein du **Laboratoire L2EP et de l'equipe INRIA-MINT** dans **l'École Doctorale Science pour L'Ingénieur ED SPI 72**

Tactile feedback devices: friction control and texture generation

Thèse à soutenir publiquement le **22 Septembre 2016** devant le jury composé de:

Pr. Edward COLGATE
Northwestern University, Evanston, USA, Rapporteur
Pr. Vincent HAYWARD
UPMC, Paris, Rapporteur
Pr. Betty LEMAIRE-SEMAIL
Université de Lille, Directrice de Thèse
Dr. Frédéric GIRAUD
Université de Lille, Co-directour de Thèse
Pr. Michael ADAMS
Birmingham University, UK, Examinateur
Pr. Hannes BLEULER
EPFL, Suisse, Examinateur
Pr. Skandar BASROUR
Polytech Grenoble, Examinateur
Pr. Laurent GRISONI
Université de Lille Examinateur

LILLE UNIVERSITY

Résumé

L2EP - Laboratoire d'électrotechnique et d'électronique de puissance de Lille

Doctor en Sciences pour l'ingńieur

Surfaces à retour tactile : controle du frottement et génération de textures

by Eric Vezzoli

L'usage des systèmes tactiles est omniprésent dans le monde d'aujourd'hui, où le principal moyen d'interaction est la pression d'un doigt sur l'écran de l'appareil, par exemple un smartphone ou une tablette. La capacité de ces interfaces pour rendre différentes sensations tactiles est assez limitée actuellement, et repose principalement sur la vibration de l'ensemble du dispositif, ce qui limite ses capacités de rendu tactile. Dans le domaine de l'haptique, peu de technologies sont compatibles avec les techniques d'acquisition de position capacitives ; parmi elles, on trouve les techniques de modulation de friction: electrovibration et vibrations ultrasoniques. L'electrovibration augmente la friction entre le doigt et une surface par l'attraction électrostatique créée par la mise sous haute tension de cette surface. Les vibrations ultrasoniques permettent de réduire le frottement en fonction de l'état vibratoire de la surface explorée. Dans cette thése, une modélisation physique des deux techniques est développée et validée expérimentalement ; les règles de conception pour les systèmes tactiles exploitant ces techniques en sont déduites. De plus, l'indépendance physique et perceptive ainsi que la compatibilité des deux techniques sont prouvées par la mise au point d'un stimulateur couplé. Enfin, le développement d'un nouveau dispositif tactile, appelé E-VITA, élaboré en accord avec les règles de conception déduites, est décrit. Sur ce dispositif, une nouvelle stratégie de controle prenant en compte les caractéristiques perceptives du doigt, est intégrée, permettant l'augmentation des capacités de rendu tactile de ces dispositifs à friction modulable.

LILLE UNIVERSITY

Abstract

L2EP - Laboratoire d'électrotechnique et d'électronique de puissance de Lille

Doctor en Sciences pour l'ingńieur

Tactile feedback devices: friction control and texture generation

by Eric Vezzoli

The interaction with tactile systems is ubiquitous in todays world, where the primary mean of interaction is the touch of a finger on the screen of the device, i.e. smartphone or tablet. The ability of these interfaces to render different tactile sensations is quite limited, and mostly composed by the vibration of the whole device, which restrain their rendering abilities. Few haptic technologies show the promising opportunity to be coupled with capacitive position acquisition techniques. Among them, there are the friction modulation techniques, also called surface haptic techniques: electrovibration and ultrasonic vibrations. The former increases the friction between the finger and a high voltage supplied surface by the induced electrostatic attraction, whereas the second reduces the friction in function of the vibrational state of the explored surface. In this thesis, for both techniques, a precise physical modelling is developed, and assessed by the comparison with experimental results; thus, design rules for these tactile devices are deduced to optimize the tactile rendering. Moreover, the physical and perceptual independence of both techniques is proven with the development of a coupled stimulator. In the end, the development of a new tactile device, named E-ViTa, conceived following the design rules outlined, is described, and a new control strategy considering the perceptual characteristics of the finger is integrated, allowing the expansion of the rendering capabilities of the surface haptic devices.

Acknowledgements

The journey, not the goal, is what matters, at least, this is what someone says. In this case, it is quite accurate. During this three years journey, i had the luck to interact with a number of exceptional characters which, by all the means, shaped the person that I'm today.

I shall start with my project advisor, Betty, which had the great patience to listen the quite numerous stupid idea that I came up with, an gave me the freedom to understand my own stupidity by clashing against reality. She is a precise, methodic, trustable and extremely logical advisor, which was the primary companion during this project.

If Betty is Dante's Beatrix, Michel is definitely Virgil, or, as he should be named, St. Michel for his proven ability to perform miracles. He is the impersonation of reality, the real filter against stupidity. He translates ideas into real systems, and make fun of everybody on the way. The foundation of the lab by any means.

Fred and Laurent have a peculiar role into the journey, always ready to discuss on the principles and ideas, and always ready to propose advancements and implications. Sometimes they should have kicked me out of the office, but the didn't, and I'm grateful for that.

I would like also to thanks Wael, Sofiane, Clement, Christophe, Ehsan, and Yosra. All of you brought invaluable help in the multiple projects that we carried out together.

Now to Prototouch. Here things get difficult, more then a project, it is now a group of friends, and, in some cases, mostly family. We started together three years ago, and the first meeting was an explosive ensemble of egos clashing against linguistic barriers. Never thought that we could work together, but we did manage, and it seems that we also did something nice. Thanks to Thomas for the invaluable discussion and maelstrom of ideas, thanks to Zlatko for being always part of the craziness, thanks to David for teaching me what quality means, even too much, thanks to Nasia for the endless supply of origan :), thanks to Teja for the aim to aesthetics perfection, thanks to Vincenzo for the adventures together, thanks to Mariama for the great work and time spent together, and thanks to Brygida for teaching me what patience means. Thanks to all the other member in the project, Andi, Serena, Michael (ps, Happy Birthday), Mario, and Dusan. It was an invaluable meeting you.

A special mention goes to Mike Adams, for me, the impersonation of science, and to Vincent Hayward, we didn't work together, but you taught me more than you can imagine, and all the other PIs in the project, and especially to Djordje, Andre, Jean-Luis, Tomaz for being the party when it was needed.

Thanks to all the friends in Lille, the weather is bad, but the friends are great! Thanks to Francesca, Clara, Sasha, Sri and Ric to be family. I got fat with the Sunday lunches, and I'm proud of that. Thanks to all the Italians and Spanish friends, especially to Clara, Gabriele, and Riccardo. Thanks to Celine and Blandine for make me discover Bleau. I might thanks also Giulia in some way, companion for the beginning of the journey.

Last but not the least thanks to Mother, a lot of thanks to Mother, and sisters, Susy and Yvo, for supporting me during all the journey. Thanks to Dad, and especially to both of the uncles Franco and Livio to give me a clear view of both sides of the coin, and for always being there.

Contents

List of Tables

Abbreviations

LHS **L**atin **H**ypercube **S**ampling

JND **J**ust **N**oticeable **D**ifference

Physical Constants

Ambient Pressure	p_0	=	101300 Pa
Dielectric Vacuum Contant	ϵ_0	=	$8.854187 \times 10^{-}12$ Pa

Symbols

F_l	Lateral Force (Friction Force)	N
F_n	Normal Force	N
τ	Interfacial Shear Strenght	Pa
A	Contact Area	m^2
p	Pressure	Pa
τ_0	Intrinsic Value of τ	Pa
α	pressure coefficient	m^-2
k_1	Contact Area Parameter	m^2/N^m
m	Areal Load Index	
E	Young's Modulus	Pa
ν	Poisson's Ratio	
R	Radius of the Sphere	m
A_{ridge}	Contact Area of the Ridges	m^2
A_{gross}	Gross Contact Area	m^2
μ	Coefficient of Friction	
L	Period of Fingerprint Ridges	m
h_e	Amplitude of Sinusoidal Ridges	m
h	Distance Between the Plate and the Finger	m
w	Vibration Amplitude	m
h_r	Roughness of the Surface	m
r_a	Density of the Air	kg/m^3
ν	Dynamic Viscosity of the Air	km/ms
σ	Squeeze Number	
Λ	Bearing Number	
P_∞	Squeeze Film Pressure	Pa

F_s	Sustain Force	N
Φ	Phase Shift	degree
t_{sa}	Time of Maximum Skin Acceleration	s
t_{pa}	Time of Maximum Plate Acceleration	s
Φ	Phase Shift	degree
RH	*Stratum Corneum* Ridge Height	µm
SCH	inner *Stratum Corneum* Thickness	µm
EH	*Dermis* Thickness	µm
STH	Subcutaneous Tissues Thickness	µm
RW	Width of the Ridge	µm
k	Penality Parameter	MPa
E_{sc}	Young's Modulus of *Stratum Corneum*	MPa
E_{ep}	Young's Modulus of *Dermis*	MPa
E_{ep}	Young's Modulus of Subcutanous Tissue	MPa
G_{sc}	Shear Modulus of *Stratum Corneum*	MPa
r	Density	kg/m^3
τ	Retardation Time	s
ζ	Rayliegh Damping	
f	Plate Frequency	Hz
T	Vibration Period	s
F_{reac}	Plate Reaction Force	s
w	Plate Amplitude	μm
w_c	Critical Vibration Amplitude	μm
Δx_c	Critical Compression	μm
t_c	Time of Contact	s
t_s	Mobilization time	s
Ψ	Dimensionless Group	
C	Capacitance	F
d	Distance Between Capacitor's Plate	m
v	Applied Voltage	V
ϵ	Relative Permittivity	
d_{sc}	*Stratum Corneum* Thickness	m
d_i	Insulator Thickness	mm

d_a	Air Layer Thickness	mm
d_{ed}	*Epidermis* Thickness	m m
d_d	*Dermis* Thickness	mm
d_a	Air Layer Thickness	mm
ϵ_{sc}	*Stratum Corneum* Relative Permittivity	
ϵ_i	Insulator Relative Permittivity	
ϵ_a	Air Relative Permittivity	
E_e	Electrostatic Co-Energy	J
F_e	Electrostatic Force	N
a	Finger Width	mm
b	Finger Height	mm
R_{sc}	*Stratum Corneum* Resistance	Ω
C_{sc}	*Stratum Corneum* Capacitance	F
τ_d	Discharge Time	s
ρ	Resistivity	Ω/m
ρ_{sc}	*Stratum Corneum* Resistivity	Ω/m
v_e	Effective Voltage	V
v_i	Insulator Voltage	V
Q_{sc}	Charge on Stratum Corneum	C

Introduction

Context

The ability to trick our sensing into perceiving virtual sensation, which we can call illusion, has long been one of the Graal for technology developers, with the first accomplished attempt being the Phonograph by Thomas Edison. For the first, time it was possible to emit a sound partially reproducing the physical effect of something real. A similar effect was present for the visual systems through photography, but the full real convincing visual illusion was the one embodied in the cinematograph reproducing the first motion picture in the 1895 by the Lumiere Brothers. A path for reproducing virtual sensation was set for both the auditory and visual system which is continuing in these days with the enormous market of audio and visual rendering machines, such as television screens or high fidelity loudspeakers. On the other hand, both the olfactory and gustatory sensing systems are based on the detection of particular kind of chemical particles, which partially limits the ability to implement effective and dynamically convincing marketable devices.

The remaining sense is touch, and tactile signals are generated trough a mechanical displacement of the body tissues which is encoded by the mechanoreceptors and transmitted to the central nervous system. Many different approaches were developed to render different tactile sensations perceived by humans: shape, stiffness, geometry, and texture, with many different devices developed to render a particular sensation. The whole branch of research aiming to study and reproduce tactile sensations is called 'Haptic'.

Within the multiple available ways to mechanically stimulate a finger, this work is focused on friction modulation techniques: the ability to modify the sliding properties

of a surface while a finger is sliding on it. By actively modulating the friction while the finger is moving, it is generated a mechanical stimulation on the finger pad resulting from the change of the boundary condition at the skin. Two main techniques are available to actively modify the friction between a finger and a surface, which show the promising opportunity for coupling with capacitive finger position tracking sensors: electrovibration and ultrasonic vibrations. Their integration into commercial product such as smartphones or tablets currently explored by multiples companies motivates the interest in deeply understanding them, and developing efficient and efficacies way to render tactile signal. The strict energetic and integration constraints present in these competitive markets will benefit from a precise understanding of the friction modulation phenomena.

Prototouch Project

This work has to be considered in the framework of the Marie Curie ITN Protototuch project (www.prototouch.com). The project focuses on the next generation of electronic user interfaces, such as tactile displays, for the implementation of high definition haptic feedback, i.e. the simulation of the tactile sensation of a texture or a pressed button. The main research goal is to exploit multiscale multiphysics simulation software, supported by neurophysiological measurements, for the virtual prototyping and optimisation of tactile displays, which with the associated research activities, will lead to a radical understanding of the underlying design principles and hence to the development of future generation devices. This will be achieved by the deployment of an inter-disciplinary network involving experts in tactile displays, computer simulation, cognitive and neural science, psychophysics, information processing, materials science, tribology and medical rehabilitation. The inter-sectoral dimension of the consortium links fundamental and applied scientists and engineers in 7 universities,

- Birmingham University - UK
- Université Catholique de Louvain - Belgium
- Goteborg University - Sweden
- Swansea University - UK

- IDSIA - Switzerland
- UPMC - France
- Lille University - France

2 multi-national companies (Unilever - UK, and ST Microelectronics - France) and 2 SMEs (C3M - Slovenia, and Metec - Germany). 15 fellows were recruited within this project, 11 early stage researchers and 4 experienced researchers distributed between the different institutions, who followed a set of intensive training in the related research fields. These trainings allowed the development of a common communication language and the emerging of research collaborations to further explore the relevant aspects of touch interaction.

The role of this PhD thesis in the project was to supply tactile devices to the evaluating partners and implement a continuous optimization on these devices based on their feedback, either experimental either coming from numerical simulations. Another aspect of the work was the development of reliable physical models of the friction modulation techniques considering the characteristics of the finger and the tactile plate, and the implementation of efficient texture rendering strategies based on the perceptual characteristics of the tactile sensing. See appendix A and B and experimental section of chapter 2 for the description of the provided device to the partners.

Thesis Structure

This manuscript is organized as follows:

Chapter 1 is composed by an introduction on the human sensory system with a focus on the tactile sense. The anatomy of the fingertip, being the primary sensor for tactile exploration, is here depicted, and the different kinds of mechanoreceptors with a description of their role into tactile encoding and bandwidth detection are described. It is followed by a bibliographic review on the tactile signal perception and an analysis of the mechanical properties of the finger pad and the skin. In the end, a review of the characteristics of the friction force between the finger and a surface is outlined.

Chapter 2 is focused on the technique of friction modulation based on ultrasonic vibrations. In the beginning, a bibliographic review on the developed devices based on this technique and the classical explanation of the reduction of the friction is derived. The first experimental assessment questioning its robustness is presented. A mechanical model of the phenomenon is then developed, based on the experimental assessment of the contact dynamics between the finger and the vibrating plate, and the finger mechanics properties presented in chapter 1. In the end, a comprehensive experimental assessment of the developed mechanical model based on *in vivo* and probe-based tribology measurements confirms the validity of the model and suggests a set of design principles, later on applied for the development of the E-ViTa device in chapter 4.

Chapter 3 regards the second available technique to modify the friction between a finger and active plate: Electrovibration. In the beginning, a bibliographic review on the developed devices and an analysis of the theoretical model available in literature are performed. Following, the influence of the air, finger mechanics and geometry are presented, and an improved dynamical model of the effect based on non-linear electrical skin properties is shown. In the end, design rules useful to reduce the power consumption of these devices are outlined.

Chapter 4 concerns the physical and perceptual equivalence of both techniques. The concept is proven through the development of a device able to perform both stimulations at the same time. Both static and dynamic measures are performed, as well as a psychophysical experiment indicating that the perceptual results valid for one technique, may be assumed valid for the other.

Chapter 5 is about the development of a new device, named E-ViTa, taking advantages of the characteristics of texture perception depicted in chapter 1 and of the design rules suggested by the modeling in chapter 2. An efficient texture reproduction algorithm is developed on this device and systematically compared with the classic one, allowing to propose high density tactile rendering based on commercial touch screens.

In the end, the conclusion and prospective of this work are outlined.

Chapter 1

Tactile Sensing, Texture Perception, and Friction and Mechanics of the Finger Pad

1.1 Introduction

The concept of life can be described as an organismic state characterized by capacity for metabolism, growth, reaction to stimuli, and reproduction [4]. The definition of the boundaries of such state are extremely controversial, but most of the considered living being can be inscribed in this definition. The conceptualization of the own body of the living being induces a natural definition of a geometrical inner and extern to the living system, where the inner is the body itself and the extern is the environment where the living being is inscribed [5]. As the previous one, this definition is controversial in the placement of the boundaries and induces endless debates, but one thing is reasonable to accept: there is the living being placed in an extern environment. The ability to respond to extern stimulation is the forth characteristic of the reported definition of life: the ability to sense and react to an extern stimulus is deeply rooted in the nature itself of the living being. The reaction to an extern stimulus is the first glimpse of sensing and it is clear that to be able to react it is necessary to have a system able to perceive the environmental changes. Where the analysis of the former three concepts is not the

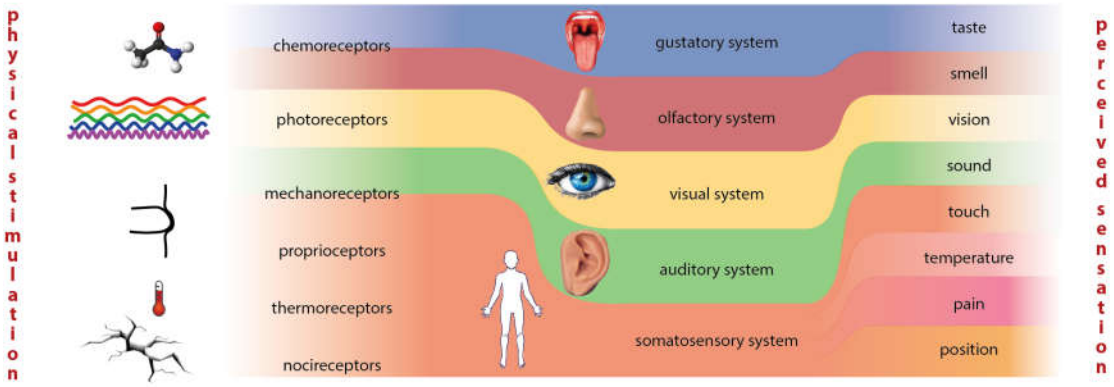

FIGURE 1.1: The general organization of the sensing system in humans. On the left are represented the different classes of receptors linked to the detected stimulus, in the center the division of the sensing systems and on the right the perceived sensation encoded.

concern of the current work, some words can be spent on the implications of the reaction to stimuli in Humans.

Classically, the human sensing system is divided in 5 systems, gustatory, olfactory, visual, auditory and somatosensory. All of them are composed of a set of sensors able to perceive a determined physical stimulus and they are connected to a central unit, the brain, organizing and processing the acquired informations, Fig. 1.1. The physical stimulus perceived by the sensor varies in function of the system involved: visible light is sensed by the cone cells in the eyes, whereas a chemical interaction is the activating stimulus for the chemoreceptors in the nose and on the tongue. In the four former systems, the receptors are concentrated in a determined part of the body: i.e. in the eyes for the visual system or mainly on the tongue for the gustatory system. On the other hand, the somatosensory system is organized in a different manner, it features a set of sensors spread with different concentrations along all the body. If the sensors of the former four systems were mainly susceptible to one kind of stimulation, the somatosensory system includes different kinds of receptors: the nociceptors, responsible for the pain sensation, the thermoreceptors, sensitive to the temperature, the proprioceptors, responsible for the geometrical placement information of the body, and the mechanoreceptors, encoding a mechanical stimulation. Whereas the former four sensing systems are relatively well understood, the somatosensory system still have some shades, mostly due to the relatively low density of its receptors in the human body and the vast quantity of information that it encodes.

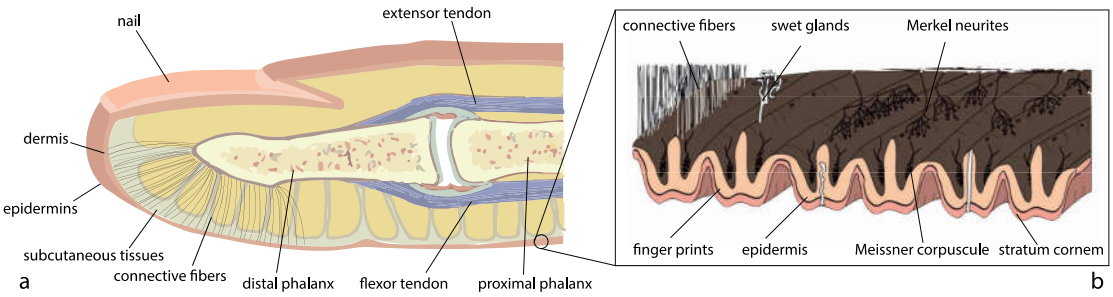

FIGURE 1.2: (a), general model of the anatomy of the finger pulp, and (b) zoom on the anatomical structure of the glabrous skin, adapted from [11].

Through the somatosensory system, the fifth Aristotelean sense is encoded: the sense of touch. It provides information on the contact of the human body with external objects which are encoded by the mechanoreceptors and transmitted to the brain. Most of everyday touch interaction is performed trough the hand fingertips due to their particular mechanical behavior, geometry, mechanoreceptor density, and mobility. The touch sensing provided by the finger pad provides many different classes of informations to the brain, it gives information of the shape of the object [6], the texture of the touched surface [7], the grip of an handled object [8], the force applied by the finger [9], and the vibrational state of the surface [10].

As this thesis is focused on the techniques to virtually render tactile sensation, an introduction on the anatomy and mechanics of the finger tip, on the perception of textured surface, and on the characteristics of the friction force experienced by the human finger will be the topic of the next sections.

1.2 Anatomy of the Finger

An introduction on the anatomy of the finger pad and the characteristics of the mechanoreceptors is presented in this section.

1.2.1 Anatomy of the Finger Pad and the Skin

Firstly, this section will be focused on the general anatomy and mechanical properties of the finger pulp and the *glabrous* skin.

The manipulation and perception of objects is mainly done through the interaction with the human hand, where the finger pulp is the extreme termination of the finger phalanx. In Fig. 1.2, it is represented the general anatomy of the finger pad. It is mainly composed of adipose tissues (subcutaneus tissues) recovered by glabrous skin which is attached to the bone by connective fibers. The structure of the skin can be exemplified as follows [12]: the most extern layer of the skin is the *stratum corneum*, it is composed of roughly 15-20 layers of dead cells without nuclei and cell organellis. It is the outermost barrier of the body and it protects the inner tissues from infection, dehydration, chemical and mechanical stress. In thick skin (hands and feet palms), an intermediate layer of *stratum lucidum* is present, which is composed of dead cells undergoing the process of transformation into *stratum corneum*. Into the *stratum granulosum*, the expulsion of the inner lipid content of the dermis cell generates the hydrophobic protection layer permeating the extern layer. The *stratum spinosum* is formed by living cells migrating from the inner to the extern of the skin, and in the end, the *stratum basale* contains a layer of epidermis stem cells continuously dividing to generate *stratum granulosum* cells. Under the epidermis it is found the dermis, which is composed of fatty tissues.

In the *stratum basale* are found two of the touch sensors, Merkel and Meissner cells, which characteristics will be detailed in the next section.

1.2.2 Mechanoreceptors

In this subsection, a description of the four classically identified mechanoreceptors located in the human finger pulp is presented.

As introduced before, the mechanical displacement of the skin tissues provided by the contact with an external object is sensed by the mechanoreceptors located in the skin, Fig. 1.3. Four different classes of mechanoreceptors are historically identified: Meissner cells, Merkel cells, Pacinian corpuscles, and Ruffini endings. Their working principle is similar [15], the induced mechanical stress opens different ionic channels across the membrane of the cell, the different chemical concentration of ions in the two sides generates an osmotic current (firing). The resulting charge unbalance between the two sides of the membrane is transmitted trough the nerve ending as an action potential (nerve impulse) to the central unit. The unbalanced concentration of the ions is then re-established through active pumping by the ion pumps present on the membrane. When the ion

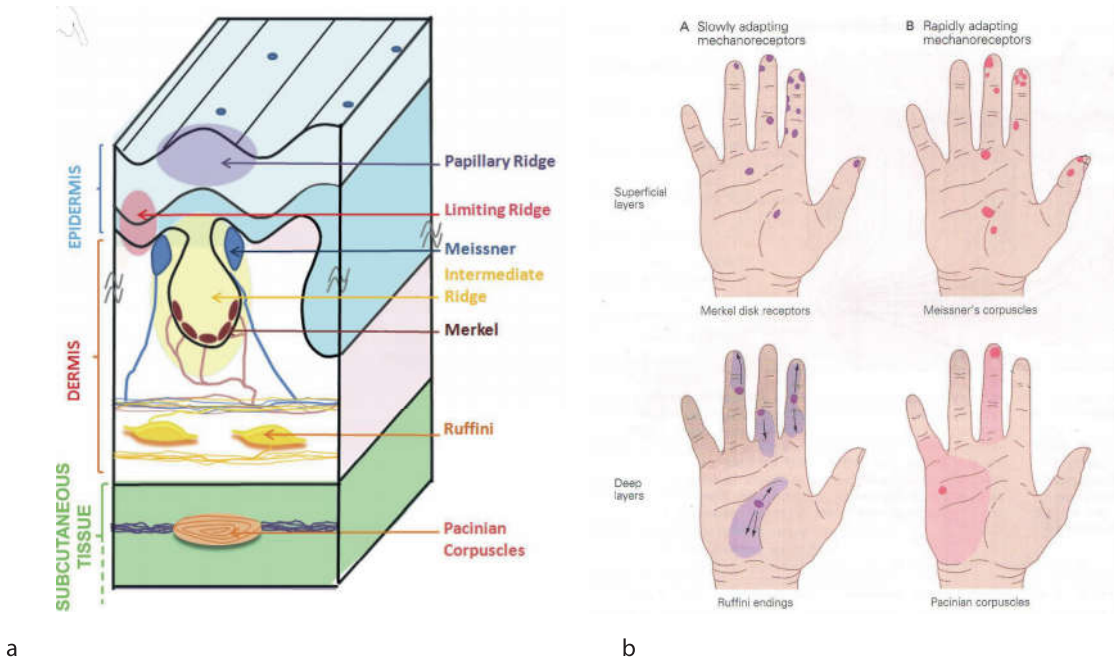

FIGURE 1.3: a, placement of the mechanoreceptors in the human skin, [13]. b, receptive field of the different classes of mechanoreceptors [14].

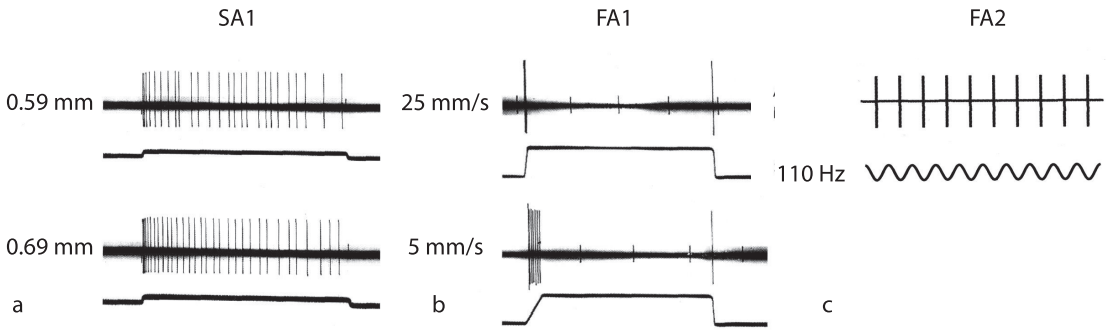

FIGURE 1.4: (a), firing in function of the time of a Merkel cell under two different indentation depths (0.59 and 0.69 mm) over the receptive field of the mechanoreceptor, the firing rate is dependent on the indentation depth. (b), firing in function of the time of a Meissner cell under two different indentation speeds. (c), firing of a Pacinian corpuscle in function of the time for a vibrational stimulus of 110 Hz. The continuous black line at the bottom of each picture represents the stimulation profile, [14].

concentration is correct, the mechanoreceptor is ready to be activated for the next stimulus. The different classes of mechanoreceptors are here described, for this purpose, the works of Johansson and Johnson will be analyzed [16–19].

Merkel cells also called first class of slowly adapting mechanoreceptors (SA1), are a set of receptors firing continuously for a continuous stimulation, Fig. 1.4. They are organized in a Neurite Complex: 25-75 Merkel cells are mechanically attached to the

intermediate ridge in the dermis and their terminations are merged in one unique nervous connection. Their firing range is localized over an area of some square mm, Fig. 1.3b. By being continuously active while mechanically stressed, they respond to the static detection of localized stimuli as edges and coarse textures, i.e. rough sandpaper. Their firing rate is dependent on the indentation depth of the external object on the skin, Fig. 1.4.

Ruffini endings also called second class of slowly adapting mechanoreceptors (SA2), are the most controversial receptors. They are often spontaneously active and are sensitive to the skin stretch over a large field, plus a smaller localized receptive field similar to the SA1, Fig. 1.3b. They are not found in monkey hands, while they are detected by microneurography in human, but rarely observed in biopsy experiments. They should be placed in the bottom part of the dermis.

Meissner cells are the first type of fast adapting mechanoreceptors (FA1). They are placed between the dermis and the epidermis at the base of the intermediate ridge. They respond to transient stimulations such as small indentations and slow skin vibrations, Fig. 1.4, and their receptive field is localized, Fig. 1.3b.

The Pacinian corpuscle is the second type of fast adapting mechanoreceptors (FA2), and is the biggest mechanoreceptor. It is deeply placed in the subcutaneus tissues, and it is strongly responsive to high frequency vibrations, Fig. 1.4. Its onion-like structure helps the filtering of different frequencies and their receptive field is extremely broad, Fig. 1.3b.

Frequency Response A comprehensive measurement of the mechanoreceptors response to different sinusoidal stimulations for different vibration amplitudes was performed by Johansson et al. in 1982 [16]. They highlighted a separation of the frequency response of the different mechanoreceptors to different periodic signals. Both the slowly adapting mechanoreceptors exhibit a frequency response in the range between 2 to 32 Hz, with maximum frequency response decreasing in when the amplitude of the stimulus rises. Note that these values were measured after a complete adaptation of the mechanoreceptors to the indentation generated by the probe. FA1 mechanoreceptors

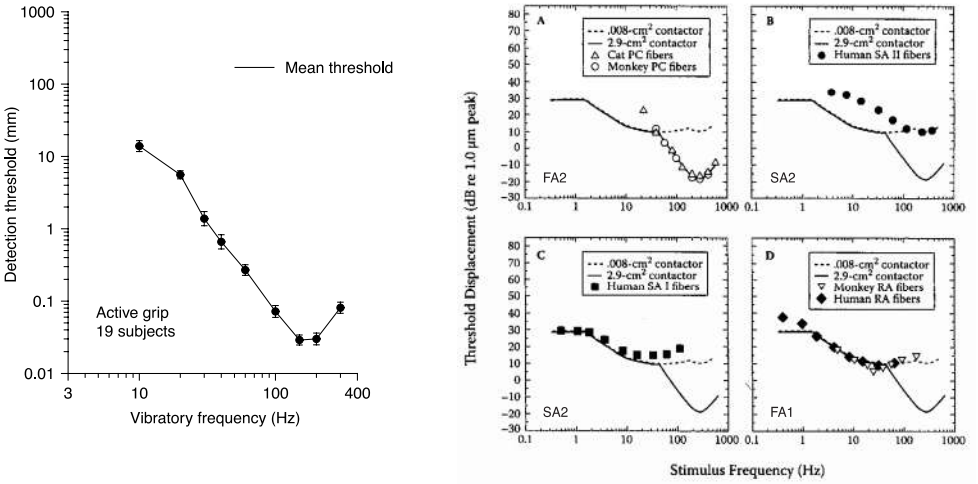

a b

FIGURE 1.5: (a), Threshold for the detection of transmitted vibration when subjects grasp a 32-mm diameter cylindrical rod. Vibrations were produced by a linear motor mounted at one end of the rod. Vibratory amplitudes were measured with a three-dimensional accelerometer mounted on the rod. The ordinate represents the mean threshold amplitude. Filled circles and solid lines represent the psychophysical thresholds. Adapted from [20]. (b), threshold displacement of the different mechanoreceptors in function of the frequency of the sinusoidal stimulation [21]. To be noted the similarity of the cumulative mechanoreceptors response (continuous line) and the psychophysical curve represented in (a).

exhibit a response between 8 and 64 Hz, again with the maximum of the firing rate decreasing when when the amplitude of the stimulation rises. Pacinan corpuscles are extremely sensitive and they are generally excited for frequencies above 64 Hz with maximal sensitivity between 128 and 400 Hz. It was reported that the smallest measured vibration amplitude necessary to generate a firing event at 256 Hz was 1 µm PTP (Peak to Peak). The sensitivity of the Pacinian corpuscles is 20 - 30 dB lower than the sensitivity of the FA1 mechanoreceptors, and the comparison of the different sensitivity and bandwidth between the different mechanoreceptors is reported in Fig. 1.5b.

1.3 Tactile Perception

In this section, the most relevant psychophysical results for vibration and texture perception will be outlined.

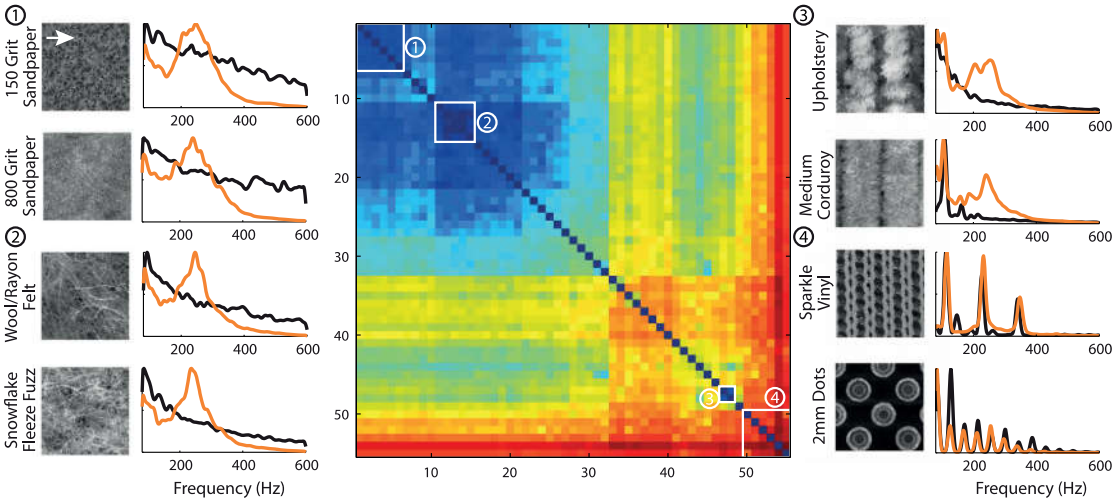

FIGURE 1.6: Distance matrix for all textures, scanned at 120 mm/s, based on vibratory spectra (distances shown on logarithmic scale). Textures are ordered such that those that yield similar spectra are close together. The white boxes highlight 4 texture sets shown to either side of the distance matrix. For each example, the image on the left shows a small patch of the texture's surface profile (5 x 5 mm), while the graph on right shows the power spectral density of the elicited vibrations at 120 mm/s (orange) and that of the corresponding surface profile (black), adapted from [22]

1.3.1 Vibration Perception

As introduced in the previous section, mechanoreceptors present in the finger have different detection bandwidth and activation thresholds, and their signals combine to give us the perception of the given stimulus. It is useful to introduce the human threshold of perception of a sinusoidal vibrating signal to have a clear view of the sensitivity of the human sense of touch along the perception bandwidth, Fig. 1.5

The threshold of perception of sinusoidal signals respects the features highlighted in [16]: the Pacinan corpuscles detection peak at ≈ 250 Hz is reflected in the higher sensitivity of the perceptual curve represented in Fig. 1.5a. The lower sensitivity of the FA1 and the SAs in the lower bandwidth is respected and confirmed by this curve. Under 10 Hz the curve flatters due to the higher sensitivity of the SA mechanoreceptors that overcome the fast adapting ones. By visual comparison of Fig. 1.5, it is straightforward to see the similarity of the psychophysical curve for the vibration perception and the summary of the contribution of the different mechanoreceptors in the human hand visualized as the continuous line in the Fig. 1.5b.

1.3.2 Texture Perception

The human ability to distinguish between different touched textures is somehow striking. We are able to discern between surface swhose features vary in the submicron scale [23], and distinguish just by a fast passage one tissue from the other, or even discern the quality of the touched silk [24]. This operation is done without any effort in everyday life. There are evidences which indicate that our perception of texture is almost completely independent on the scanning velocity [25–27], which is actually surprising if we consider the accurate temporal response that the mechanoreceptors exhibit and the great variability of the exploration velocity commonly used in exploration tasks [28]. It has been shown that the exploration of a periodical texture induces a periodical modulation pattern of the lateral force [29] and that the spatial spectrum of the skin displacement can encode tactual textures [30]. These results suggest that the mechanoreceptors will respond in a different modality when the scanning velocity is variated by the subjects, and that we are able to reconstruct efficiently the characteristics of the perceived texture based on these extremely variable data.

A lot of research was performed in the previous years about the modality of encoding of the touched textures, and how this encoding is then interpreted by the brain to reconstruct our perceived sensation. The subjective assessment of the roughness of fine but not coarse textures is greatly enhanced by sliding. This suggested fundamental difference in the perception of texture which was initially postulated by Katz, called the *duplex theory of texture perception* [31]. In [22], there is an assessment of this theory; it was suggested that just coarse textures are encoded by slowly adapting mechanoreceptors, whereas the encoding of fine stimuli is performed by the fast adapting one. That means that just the vibrational pattern induced by the surface on the skin, called *vibrotaction*, and not the spatial arrangement of the surface, determines our perception of fine texture. In Fig. 1.6, the summary of the results showed in [32] is represented. The authors analysed the vibration patterns induced in the skin for different vibration pattern elicited by natural textures passively sliding on the finger at 120 mm/s, and they categorized them in function of their vibratory spectrum distance. The results show that for each texture a quite well defined vibration spectrum elicited in the finger is associated.

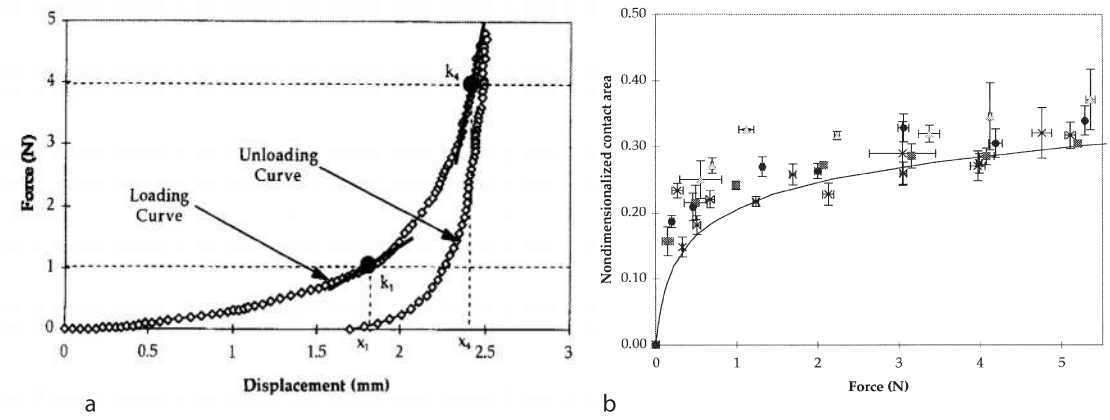

FIGURE 1.7: (a), typical fingertip pulp force-displacement curve from one subject for a single tap on a surface, from [35]. (b), Nondimensionalized contact area vs. force applied. The real contact area was computed with ink placed on the finger pad and pressed on a paper surface with different force applied, and the colored area analyzed, from [36]

This finding has a straightforward consequence: even if the finger perception is impaired, the subject ability to discriminate texture is maintained [33]. This consequence can be understood considering that the vibrations detected by the finger are transmitted up to the forearm [34] and the receptive field of the Pacinian corpuscles is quite large in the hand, Fig. 1.3. This does confirm the predominance of high vibration signals for the perception of fine textures and the concept of spatial independence of the signal induced by fine texture will be analysed in the last section. It will be applied to develop efficient algorithm for texture representation in surface haptic devices.

The proven importance of the finger sliding on a surface to perceive its features leads to the analysis of the mechanical and sliding interaction between the finger and a given surface.

1.4 Finger Mechanics and Contact Mechanisms, and Friction

In this section a brief introduction of the finger mechanics, contact mechanisms and friction of the finger pad will be introduced.

1.4.1 Finger Pulp and Skin Mechanics

As introduced in section 1.2.1, the finger pad is composed of multiple material layers and structure which deeply influence its mechanical behavior. The different composition of the layers, and their different material properties deeply characterize the response to extern stimuli. In this subsection, a description of the mechanical characteristics of the fingerpad and the skin will be presented.

Normal Displacement Early measurements analyzed the *in vivo* Force-Displacement and Force-Contact Area of the finger tip tapping against a flat surface, Fig. 1.7 [35, 36]. In these works, the authors highlighted the small stiffness of the finger tip for a force applied < 1 N and the strong, non-linear, viscoelastic behavior visible in Fig. 1.7 because of the difference between the loading and unloading phase of the finger pad. The great displacement (≈ 2 mm) necessary to induce a force reaction of ≈ 1 N of the finger pad which corresponds to almost the saturation of the contact area, is remarkable, Fig. 1.7b. From this point, a greater applied force corresponds to a smaller displacement, an almost invariable contact area and greater tissue stiffness. The authors argued that the detected mechanical properties strongly dependent on the normal force validate the effectiveness of the finger tip as a tactile sensor below 1 N of force applied. The rapid change of the contact area in function of the applied force induces a great mechanoreceptors stimulation for a small variation of force. On the contrary, a greater force applied does not result into a remarkable change in the firing rate of the mechanoreceptors in the fingertip [16].

Lateral Displacement Similar experiments were performed for the evaluation of the tangential viscoelasticity of the finger pulp. The lateral displacement of the finger tip is a fundamental information while grasping and interacting with objects. In [37], the lateral stiffness of the finger pad under load was evaluated *in vivo* for incremental tangential displacements. In the experiment, a displacement of the skin of 0.635 mm was incrementally applied and 10 s were waited to track the evolution of the lateral force in time between one increment and the other, Fig. 1.8. The relaxation of the finger pulp is evident from the behavior of the lateral force which decreases during the loaded phase. Similarly to the normal load, the behavior of the measured lateral force is non linear and decreases rapidly in the first 3-4 s.

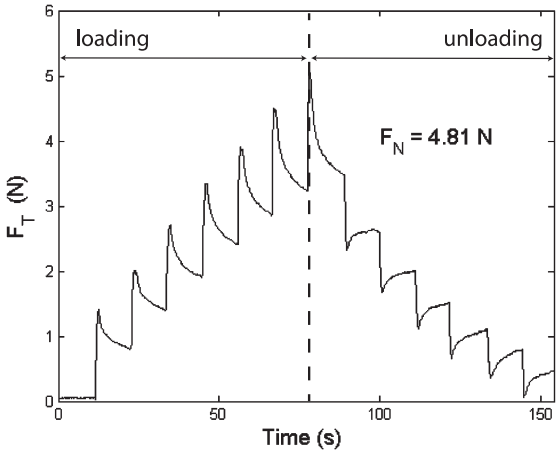

FIGURE 1.8: Raw F_t data for a trial with average F_n=4.81N, where F_t is the measured tangential force and F_n the measured normal load. The unloading increments began at approximately 80s in the trial shown [37].

Loading-unloading hysteresis confirmed the results of the work of [36], which suggested a nonlinear viscoelastic behavior of the whole finger pulp, for normal and lateral displacement.

Skin Mechanics The previous introduced experiments concerned the behavior of the whole finger pad under a normal or lateral loading. Due to the greater stiffness of the epidermis compared to the inner tissues, these experimental results reflected the mechanical characteristics of the latter. A precise evaluation of the *in vivo* skin behavior was performed by Wang et al. [38]. They measured the nonlinear behavior of the skin (epidermis) under tangential traction. A couple of piezoelectric benders were used to stretch laterally the skin in two perpendicular directions and through an isotonic (imposed force) or isomeric (imposed displacement) condition. The study enabled to model the behavior of the skin as a second order viscoelastic material; a reproduction of the relaxation behavior of the skin for the isomeric modality is reported in Fig. 1.9. As for the previous experiments, a marked relaxation behavior is observed in the performed measurements.

Summary Even if the epidermis and the inner tissues are characterized by different rigidities (higher for the epidermis), they both highlight a highly viscous behavior. This will justify the assumptions for the mechanical model of a finger interacting with an ultrasonic vibration that will be presented in the next chapter.

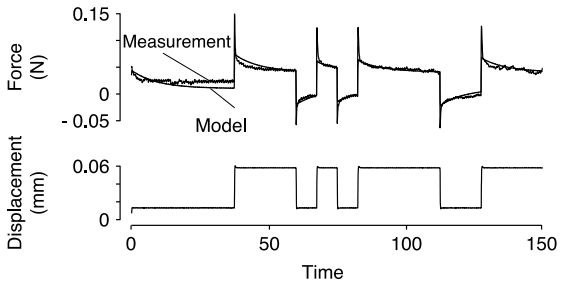

FIGURE 1.9: Relaxation behavior of the skin. For many subjects, after each displacement transient, the force dropped abruptly and then slowly relaxed over a long time period. [38].

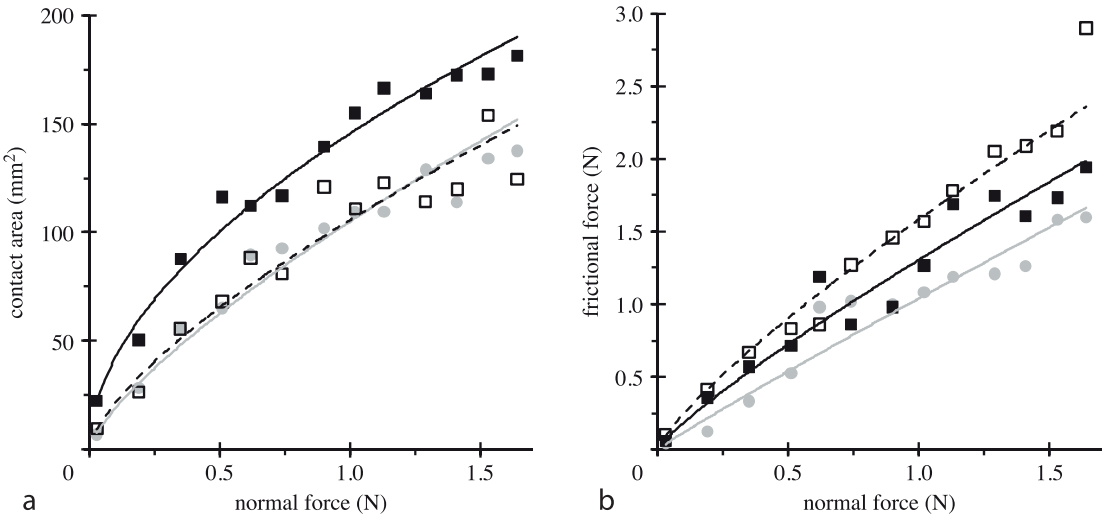

FIGURE 1.10: The relationship between (a) the contact area and (b) the dynamic frictional force of individual finger pads as a function of the applied normal force, for three different fingers held flat against an acrylic sheet. Index finger, filled black squares; middle finger, filled grey circles and thumb, unfilled black squares. The lines in (a) and (b) are the best fits to Eq. 1.4 and 1.7, respectively. Index finger, black line; middle finger, grey line; and thumb, dashed line. The data are taken from fig. 2 in the study of Warman and Ennos [39] and the figure was adapted from [40].

1.4.2 Finger Friction

In this subsection, the characteristics of the friction experienced by the finger pad while interacting with a surface will be recalled. For this section, the review of Adams et al. [40] will be considered.

1.4.2.1 Friction Dependence on Contact Area

In this subsection, the friction force between a finger sliding on a flat surface will be modelled with a theory valid for organic polymers.

The friction between two sliding bodies can be described by a *two term model* that includes an additive decomposition of an adhesion and deformation term [41]. The deformation component is mainly important for the sliding or rolling of hard lubricated probes on planar softer materials such as elastomers; however it was shown that the contribution of this term was negligible for the unlubricated skin of the inner forearm. For this reason, the friction force F_l experienced by organic polymers can be described just by the adhesion mechanism:

$$F_l = \tau A \tag{1.1}$$

where τ is the interfacial shear strength and A is the real area of contact. The relation between the friction force and the normal force applied, F_n, is the friction coefficient:

$$\mu = \frac{F_l}{F_n} \tag{1.2}$$

The parameter τ arises from the energy dissipated by the rupture of intermolecular junctions intermittently formed at the sliding interface and the deformation of a thin subsurface layer adjacent to this interface. For glassy organic polymers, the parameter τ scales in function of the mean contact pressure p [42]:

$$\tau = \tau_0 + \alpha p \tag{1.3}$$

where τ_0 is the intrinsic value of τ at zero contact pressure, α a pressure coefficient and p is given by F_n/A. For a sphere in contact with a flat surface, the contact area can be described by:

$$A = k_1 F_n^m \tag{1.4}$$

where k_1 is a parameter, and the areal load index m is equal to one if at least one of the two bodies is topographically rough [43]. In that case, that means that the contact area is linearly dependent on the normal load applied. For a sphere in contact with a flat surface, where at least one of the two bodies can be considered rigid and both of them

topologically smooth, it assumes the expression of the contact area corresponds to the Hertz equation with $m = 2/3$:

$$A = \pi \left[\frac{3R(1-\nu^2)}{4E} \right]^{2/3} F_n^{2/3} \tag{1.5}$$

where E and ν are recpectively the Young's modulus and Poisson's ratio of the deformable body, and R the radius of the sphere.

It was observed that the friction coefficient between the finger and a surface can increase with the decreasing of the normal load [44]. It is possible to account of such dependence by considering Eq. 1.1, 1.3, and 1.5.

$$F_l = (\tau_0 + \alpha p)A = \pi \tau_0 \left[\frac{3R(1-\nu^2)}{4E} \right]^{2/3} F_n^{2/3} + \alpha F_n \tag{1.6}$$

It was shown that this equation can be approximated by [45]:

$$F_l = k_2 F_n^m \tag{1.7}$$

where m is termed the frictional load index and k_2 is a load-dependent coefficient of friction, thus:

$$\mu = \frac{F_l}{F_n} = \frac{k_2}{F_n^{1-m}} \tag{1.8}$$

It has been shown that for the finger in contact with a flat surface $2/3 < m < 1$ [45] and it can be deduced from Eq. 1.6. The non linearity between the friction and the normal force was predictable because of the non linearity between the contact area and the friction force visible in Fig. 1.10.

Moreover, the human finger pad is a multilayered structure where the epidermis has greater stiffness than the inner tissue, which dominates the contribution of the changing of the contact area in function of the normal force applied. The ridged and surface topography geometry of the palmar region reduces the real contact area such as $A < A_{ridge} < A_{gross}$, where A_{gross} is the total contact area of a sphere with the mechanical

characteristics of the finger pulp, and A_{ridge} the contact area provided by the finger print.

In summary, the friction between the finger and the surface can be described by a coefficient τ summarizing the interface interaction between the two bodies, and the real contacting area A Eq. 1.1, which depends on the external structural characteristics of the finger and the surface topography. These results confirm that the friction of the finger pad can be described with a theory valid for organic polymers.

1.4.2.2 Occlusion

In this subsection the phenomenon of occlusion will be introduced.

In an early work, Smith and Scott [46] found that the friction coefficient of a subject sliding unidirectionally over a wide range of surfaces was increasing stroke after stroke. In one run of measures, they found an increase from 0.36 to 0.79. This phenomenon is called occlusion.

A more systematic work was carried by Andre et al. [44], who reported values of the coefficient of friction measured during grip studies as a function of the moisture content at the skin surface of a finger pad. The subjects exhibited moisture levels that ranged from dry to very wet and it was found that there was a maximum value of the coefficient of friction at intermediate moisture levels. It was subsequently observed that the measured moisture values either increased, remained unchanged or decreased after prolonged contact, depending on the inherent wetness exhibited by the subject at the initial contact [47]. They suggest that this was an evidence of a natural mechanism, resulting in an optimal moisture content for achieving a maximum friction between the finger pad and an object. Precise tribological measures of the evolution of the friction force in function of the time while sliding on an optically smooth surface were performed by Pasumarty et al. [48]. They explored the behavior of the friction in function of different sliding velocities and concluded that the characteristic time associated to the increase of the friction was not dependent on the velocity of exploration. These results allowed them to conclude that the frictional increase was not generated by deposited moisture on the

surface, which would lead to a decrase of the maximum friction over time, but to a similar natural effect as proposed by Andre et al [44] leading to an automatic maximization of the friction coefficient between the finger and the object, Fig. 1.11.

Adams et al. [49] suggested that this phenomenon, and the consequent increase of the contact area determining the increase of the friction, is provided by the full plasticization of the fingerprints following the secretion of moisture by the sweat pores. As introduced in the previous sections, the *stratum corneum* composes the most extern layer of the skin, and its stiffness decreases with the increasing of its water content. The softer elastic properties induced by the moisturization of the skin during sliding or gripping actions induce an increase of the real contact area, which generates the increase in friction experienced by the finger pad. However, this phenomenon has an optimum value, an excess of water content of the skin, or an addition of external liquid, determines a decrease of the τ constant compensating the increase of the contacting area, Fig. 1.11.

Speculatively, the occlusion phenomenon is well understandable by our evolutionary process: the need to interact with objects while living in an external environment induced the evolution of a mechanism to avoid as much as possible the slip of the object during the interaction. The ability to hold a tree branch along time could have determined the surviving of the living being, and the maximum exploitable friction generated by this automatic process, ensures the lowest energy consumption.

In summary the friction force between the finger modifies its value during the exploration or the interaction with the objects. This modification is determined by the increase of the real contacting area induced by the level of moisture content of the *stratum corneum*, which is automatically adjusted by body to ensure the maximum friction between the finger and the surface.

1.4.2.3 Influence of sliding velocity

Few precise experimental evaluations of the frictional force in function of the sliding velocity of the finger were performed in the literature, this is particularly relevant considering the influence of high frequency skin vibrations on the texture perception. For example, Dinc et al. [48] carried out measurements at three sliding velocities of 6, 20 and

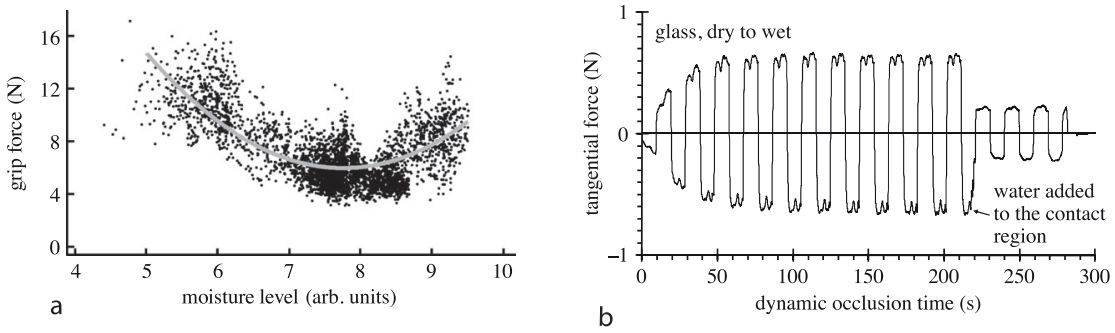

FIGURE 1.11: (a), The static grip force as a function of moisture level for the finger pads of eight subjects each involving 20 blocks of 25 trials of sequential grip procedures. The line is the best fit to the data and exhibits a minimum at approximately 7.75 arbitrary units corresponding to the optimal moisture level for grip. Adapted from Andre et al [44] in [40]. (b), Tangential force data for a dry finger pad sliding against optically smooth glass as a function of the dynamic occlusion time, followed by the addition of water in the contact (F_n = 0.2 N and V = 6 mm/s). Adapted from Pasumarty et al. [48] in [40]

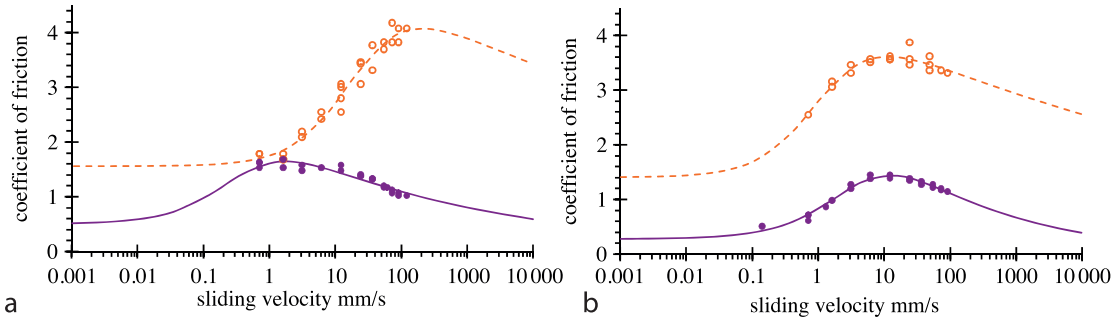

FIGURE 1.12: The dynamic coefficient of friction (F_n = 0.2 N) for a finger pad as a function of sliding velocity for (a) an optically smooth glass surface, and (b) a smooth polypropylene surface. The steady-state dry values of the coefficient of friction, μ_∞: unfilled circles and the wet values of the coefficient of friction, μ_w: filled circles. The lines are the best fits to equation (5.4) reported in [40]. The data are taken from figs 18 and 19 in the study of Pasumarty et al. [48], adapted from Adams et al. [40]

60 mm/s. They found that the coefficient of friction typically decreased with increasing velocity in this range for both smooth and rough polymeric surfaces.

Pasumarty et al. [48] carried out more detailed studies. Fig. 1.12 shows their data for smooth glass and polypropylene surfaces in the occluded and wet states; as described in the previous sections, the values are less in the wet compared with the fully occluded state. These two states are represented in Fig. 1.12 by the dashed (occluded) and continuous (wet) line. It appears that the coefficients of friction exhibit a maximum in approximately the velocity range for tactile exploration (10 - 120 mm/s), [28]. There is some evidence that the wet friction of the inner forearm also exhibits a maximum in a similar velocity range [50]. These results were interpreted by the application of the

stochastic adhesion theory valid for polymers developed by Schallamach [51], which will be qualitatively presented here.

In this paper [51], the dynamic friction between a polymer and a smooth rigid surface is computed through the interplay between two opposing phenomena: the bonding generation between the molecular chain of the polymers and the rigid surface, and the braking of these bondings. The friction between the two bodies arises from the necessary energy to brake these bondings and move the object. Being both of these thermally activated phenomenon, the latter is facilitated by the accumulation of elastic energy in the molecular chains through the relative movement of the polymeric object in respect to the surface. Both of these phenomena are governed by two characteristics times, one shorter for the pinning of the molecules, and one longer for the depinning, which determines the dynamic of the friction in respect of the velocity. For low relative velocities, the faster movement determines a longer unchaining of the molecules before the disruption of the bonding. This induces a larger accumulated elastic energy due to Hook's law, resulting in an increasing friction in function of the velocity. When the velocity is fast enough that available time for the repinning doesn't allow the total bonding of the molecular population, the friction starts to decrease due to the reduction of the total pinned population, which generates the progressive reduction of friction in function of the velocity. The application of this theory allowed the engineering of low friction polymers such as Teflon having a particular chemistry and molecular surface arrangement preventing to form strong bondings at the interface.

It was introduced before that tribologically speaking, the finger pad can be treated as an organic polymer, and the application of the presented theory to the velocity dependence of the friction between the finger pad and a surface is presented in Fig. 1.12 for a fully occluded and wet case. The parameters of the function were fitted, mainly due to the absence of any experimental measurements of such quantities in literature, nevertheless, the model is able to reproduce the behavior of the experimentally gathered data.

In summary, the dependence of the friction between the finger pad and material exhibits a maximum for the range of exploration velocities commonly used for tactile interaction, and its behavior can be interpreted by the application of the stochastic adhesion theory of the friction which predicts such dependence.

1.5 Conclusion

In this chapter, the relevant characteristics of the tactile exploration were outlined with respect of the finger pad. Its peculiar anatomy and the characteristics of the mechanoreceptors response were introduced with a focus on the vibration and texture detection. The mechanics of the finger pad plays a fundamental role in the human ability to handle and perceive surfaces and objects, and its qualitative characteristics were reported. They will be useful for the developing of the mechanical model of the interaction of the finger with an ultrasonic vibrating plate reported in the next chapter. In the end, the characteristics of the friction experienced by the human finger interpreted with a theory valid for organic polymers were presented. They will be useful to justify the conclusions of the ultrasonic friction reduction model introduced in the next chapter.

Chapter 2

Friction Control by Ultrasonic Vibrations

2.1 Introduction

A finger sliding on an ultrasonic vibrating plate experiences a modification of the friction accordingly to the vibration amplitude of the surface. This phenomenon was firstly described by Watanabe et al. [52]. In this fundamental paper, the authors highlighted the perception change of different surfaces characterized by multiple roughnesses, accordingly to the amplitude of vibration. They suggested a first explanation of the phenomenon based on the *squeeze film* effect, which relies on the cyclical compression and decompression of the air trapped between the finger and the vibrating surface, that generates an overpressure sustaining the finger and reducing the friction. Based on this hypothesis, an analytical model predicting the behavior of the friction in function of surface roughness, vibration amplitude, and geometry of the finger has been developed by Biet et al. [53]. An evolution of this analytical model was proposed by Winter et al. [54] with a more refined Finite Element approach, concluding that the analytical modelling was fundamentally valid, provided some correction considering the border effects, which were neglected on the analytical model. Both of these works were fundamentally focused on a plane actuator without the consideration of the contact between bodies. Aside of the modelling, the ultrasonic friction reduction gave birth to a vibrant development of haptic devices, and gave a fundamental contribution to the generation of the

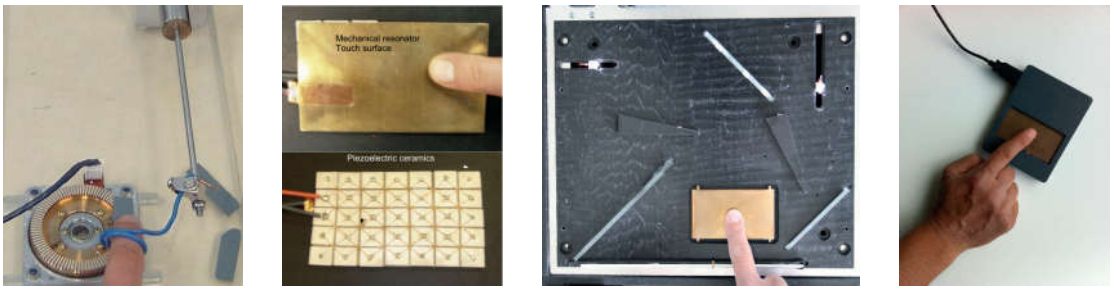

FIGURE 2.1: evolution of the ultrasonic vibration interface in the L2EP laboratory. 1D prefiguration (2004), 2D feedback (2007), 2D input and feedback (2008) and compact USB prototype (2010) [56]

Surface Haptic Community. Two groundbreaking works need to be recalled, introducing the first haptic devices based on this concept: the T-Pad by Winfield et al. [55] and the STIMTAC by Amberg et al. [56], associated with the work on texture reproduction by Biet et al. [57]. In these works, the vibration amplitude was changing in function of the finger position. The generation of the relation between the finger position and the generated friction level opened the way to the generation of virtual textures with friction modulation devices by changing the boundary condition at the bottom of the finger tip. In Fig. 2.1 is represented the evolution of the structure of the friction modulation device STIMTAC since its first discovery by the exploration of a rotor of a piezoelectric motor, to a compact USB prototype. In these devices, the finger position tracking was performed with force-based or optical solutions. In the recent years, a lot of efforts was posed to propose a suitable industrialization process involving ultrasonic vibrating devices, where Casset et al [58] managed to produce a prototype of a device actuated by deposited AlN piezoelectric film material on a glass substrate, and integrated it with a classic capacitive sensing system. A potential application of ultrasonic device is for the study of the sense of touch in fMRI environment, due to the absence of ferromagnetic components involved in the stimulations, they could be coupled with existing system [59] to expand the rendering and stimulation capability.

Since the increase of the market of smarthphones and tablets, the democratization of capacitive based finger tracking technique and small LCD screen, the development of visual-tactile co-stimulation became a fundamental challenge, Fig. 2.2.

The ability of the ultrasonic vibrations to modify the friction perception of the user is well accepted by the community, however, a little effort has been put on the validation of the squeeze film effect assumption. Multiple advantages may arise from a reliable

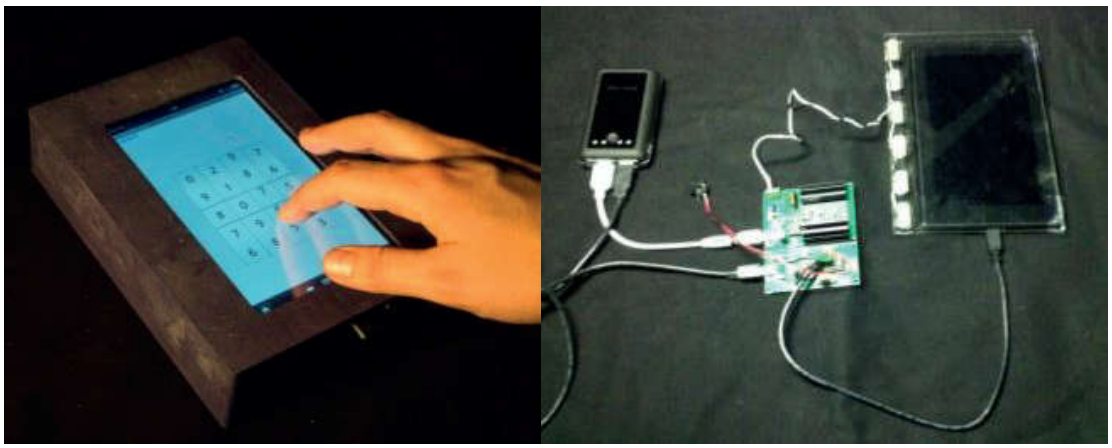

FIGURE 2.2: Representation of the TPad Fire with a tactile-visual coupling

model of the interplay between the finger sliding on an ultrasonic vibrating plate, to optimize the design of the devices, as well as reduce their power consumption.

The aim of this chapter is to propose an accurate explanation and an associated modelling or the reduction of friction experienced by the finger sliding on an ultrasonic device, an it is organized as follows: firstly the classic explanation of the reduction of friction by the squeeze film effect will be recalled. Following, different experimental validation questioning its robustness will be shown. Later on, a Finite Element mechanical model of the interplay between the finger and the plate will be described and calibrated with experimental data. The developed model will allow to mechanically predict the reduction of friction without the need to invoke an aerodynamic approach. An elastic spring slider will help the understanding of the interaction, and a dimensionless factor regrouping the variables playing a role in the reduction of friction will be proposed. A set of tribological experiments with artificial and real fingertips will prove the validity of the proposed mechanical model and a set of design rules for ultrasonic devices will be derived.

2.2 Classic Explanation of Friction Reduction

2.2.1 Squeeze Film Effect Model

This section describes the analytical model of acoustic levitation firstly proposed to explain the reduction of friction provided by the ultrasonic vibrating devices. The principle relies on the generation of an ultra-thin film of air (air gap) in the contact region by

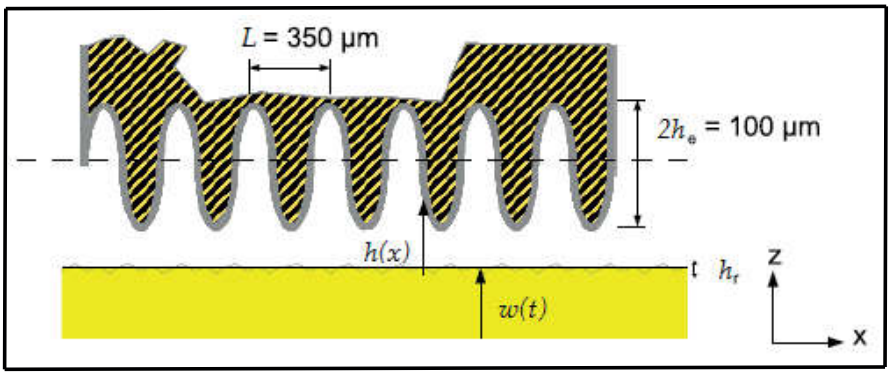

FIGURE 2.3: Approximation of the fingerpad for the analytical resolution of the Reynolds equations for ultrasonic devices [53]. L is the period of the fingerprint ridges, h_e the amplitude of the sinusoidal ridges, h is the distance between the plate and the finger, w is the vibration amplitude and h_r is the roughness of the surface.

the compression-decompressing cycle of the gaseous media. The film is subject to compression and rarefaction at high frequencies in phase with the relative displacement of the surfaces. This principle was firstly modelled by Biet et al. [53] and in the following subsection the keypoints of the modelling will be recalled.

In Fig. 2.3 is represented the modelling of the finger pad used to derive the model. The finger pad is represented in 1 dimension and the ridges are approximated by a cosine function. They are considered to be rigid, or at least extremely stiff, at these frequencies. With h_{vib} being the amplitude of vibration and h_r the surface roughness, the thickness of the air film can then be expressed by:

$$h(x,t) - h_r + h_{vib}[1 + cos(\omega t)] + h_e\left[1 + cos\left(\frac{2\pi}{L}x\right)\right] \tag{2.1}$$

where the pulsation of the vibrating plate is given by ω. The relationship between the thickness, h, of the air-gap and the pressure between the plates, p, can be described by the Reynolds equations:

$$\frac{\partial}{\partial x}\left(\frac{h^3 r_a}{\eta}\frac{\partial p}{\partial x}\right) + \frac{\partial}{\partial y}\left(\frac{h^3 r_a}{\eta}\frac{\partial r_a}{\partial y}\right) = 6v\frac{\partial}{\partial x}(hr_a) + 12\frac{\partial}{\partial t}(hr_a) \tag{2.2}$$

here r_a and η are respectively the density and dynamic viscosity of the air. The parameter v is the tangential velocity of the surface (exploration velocity of the participant finger). A normalized version of Eq. 2.2 is commonly used to describe the squeeze film effect. The new equation introduces the squeeze number σ and the bearing number Λ:

$$\frac{\partial}{\partial X}\left(H^3 P \frac{\partial P}{\partial X}\right) + \frac{\partial}{\partial Y}\left(H^3 P \frac{\partial P}{\partial Y}\right) = \Lambda \frac{\partial}{\partial X}(HP) + \sigma \frac{\partial}{\partial T}(HP) \tag{2.3}$$

where:

$$\Lambda = \frac{6\eta v l_0}{h_0^2 p_0}, \quad \sigma = \frac{12\eta\omega_0 l_0^2}{h_0^2 p_0}, \quad X = \frac{x}{l_0}, \quad Y = \frac{y}{l_0}, \quad H = \frac{H}{l_0}, \quad \text{and} \quad P = \frac{P}{p_0}, \tag{2.4}$$

This equation is solved in [60] with the assumption of a very large value of σ ($\sigma \to \infty$) by applying the previous mean amplitude Eq. 2.1 to this configuration. The resulting differential equation leads to the new local pressure p_∞ of the thin film:

$$P_\infty = p_0 \frac{\Big(1 + \delta cos(kX)\Big)\sqrt{\Big(1 + \delta cos\big(\frac{k}{2}\big)\Big)^2 + \frac{3}{2}\epsilon^2}}{\Big(1 + \delta cos\big(\frac{k}{2}\big)\Big)\Big(1 + \epsilon cos(T) + \delta cos(kX)\Big)} \tag{2.5}$$

where:

$$\epsilon = \frac{h_{vib}}{h_0 + h_e} \quad , \quad \delta = \frac{h_e}{h_0 + h_e} \quad \text{and} \quad k = \frac{2\pi l_0}{L} \tag{2.6}$$

TABLE 2.1: Squeeze Film Model Parameter Values

ridges amplitude	h_e	50 µm
fingerptint period	L	350 µm
surface roughness	h_r	1.2 µm
contact length	l_0	$1cm$
normal force applied	F_n	$0.1 - 0.5N$
dynamic viscosity of the air	η	1.85x10^{-}5 Pa s
atmospheric Pressure	p_0	$0.1MPa$

By integrating Eq. 2.5 in time and position, the mean force applied to the finger pad by the squeeze film effect can be determined. F_s is the force applied per unit length in continuous mode.

$$F_s = \frac{1}{2\Pi}\int_0^{2\pi}\int_{-\frac{1}{2}}^{\frac{1}{2}}(p_\infty - 1)dXdT \tag{2.7}$$

The solution to Eq.2.5 assumed that $\sigma \to \infty$. Nevertheless it is generally admitted that this condition can be restricted to $\sigma > 10$, which is applicable for a vibrational frequency $> 25kHz$ [53] (above the human maximum hearing range). It is then possible to calculate μ', which is given by the coefficient of friction under actuation, $\mu(w)$, relative to that at rest, μ_0, at an amplitude of vibration of 0 µm.

$$\mu' = \frac{\mu(w)}{\mu_0} = 1 - \frac{(p_\infty - 1)}{p_0} \tag{2.8}$$

The parameters in Table 2.1 are then applied to calculate the relative dynamic friction coefficient, μ', for a given surface roughness of the vibrating plate.

As can be seen in Fig. 2.4, this squeeze film model predicts a reduction to zero of the dynamic friction coefficient when the amplitude of vibration increases. Moreover, the model is also dependent on the surface roughness of the plate, which would induce a different friction reduction behavior for different surface finishes.

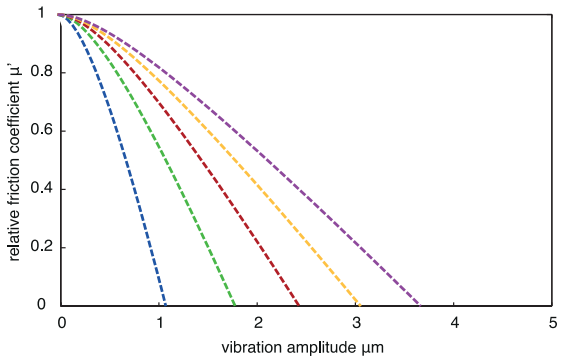

FIGURE 2.4: Modeling of the relative friction coefficient for different normal loads between 0.1 N (left dashed line) and 0.5 N (right dashed line) for the parameters' value reported in Table 2.1.

2.2.2 Preliminary Experimental Evaluation

To investigate the validity of the proposed squeeze film model, a preliminary experiment has been developed. The aim of the experiment is to compare the reduction of the friction tribologically measured with the one predicted by the squeeze film model during active exploration.

2.2.2.1 Experimental Setup

To measure the normal and lateral forces felt by the finger, a tribometer has been developed, Fig. 2.5a. It features a normal force sensor (Nano43, ATI, USA) and a floating table equipped with a force sensor (FSG, Honywell, USA) coupled with a conditioner (max4209H, Maxim Integrated, USA) to gather lateral force data. In Fig. 2.5b is represented the ultrasonic vibrating plate used for this experiment: it is a $14 \times 40 \times 1$ mm aluminum plate equipped with 5 piezoceramics, 4 used as motors and 1 used as sensor to acquire the vibration amplitude of the plate. The resonance frequency of the plate is around $36kHz$ and the relation between the voltage of the sensor piezoceramic and the vibration amplitude has been calibrated with a vibrometer (OVF-5000, Polytech, Germany). A waveform generator (33120A, Agilent, USA) provides the input signal amplified by a high bandwidth amplifier (HSA 4052, NF, Japan) powering the plate. The acquisition of the lateral and normal force signals as well as the vibration amplitude is provided by an oscilloscope (3014B, Tektronix, USA). The data are acquired and elaborated in a post-process with Matlab.

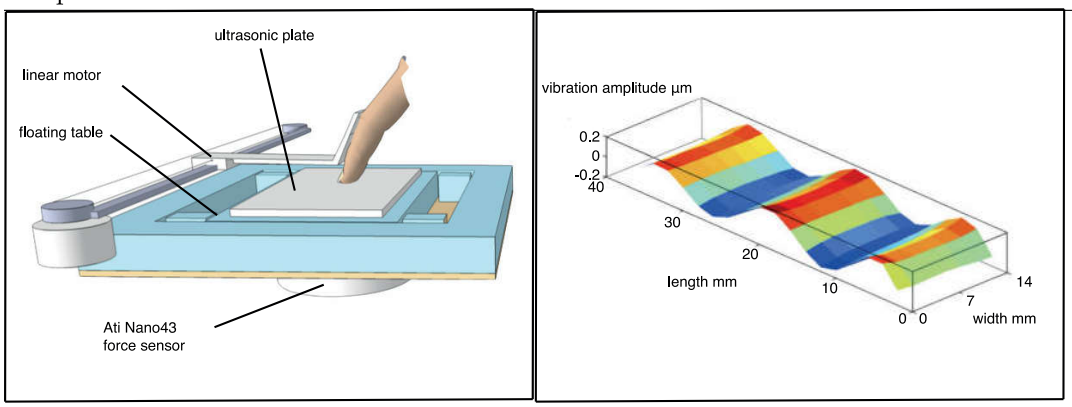

a b

FIGURE 2.5: (a), Structure of the tribometer developed to measure the force between the finger sliding on a surface, and (b) representation of the vibrational mode of the ultrasonic plate employed for the preliminary experiment.

2.2.2.2 Experimental Protocol

The measure was performed by the author of this Thesis. Before the beginning of the experiment, the participant's finger was washed with commercial soap, dried with absorbent paper and let equilibrate for 10 minutes, and the plate was cleaned with alcohol before. The experiment was performed in free exploration by the user, and some training was necessary to ensure that the normal force applied by the participant was stable along the exploration. The vibration amplitude of the plate was changed within a stroke of the user at the midpoint of the plate and maintained till the end of the exploration. The vibration amplitude level on the active side of the plate was varied between 0 up to 4.3 µm to search for the total acoustic levitation. The friction coefficient was computed as the ratio between measured lateral and normal forces for each part of the run:

$$\mu(\omega) = \frac{F_l}{F_n} \tag{2.9}$$

following, the relative friction coefficient was computed through Eq. 2.8.

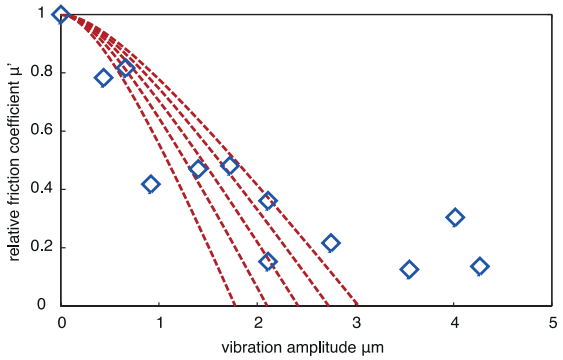

FIGURE 2.6: Comparison between the preliminary experimental results (blue diamonds) and the prediction of the squeeze film model (red dashed lines) of the reduced friction for the range of the experimentally applied normal forces, the left line is for 0.2 N applied, whereas the right line corresponds to 0.4 N applied.

2.2.2.3 Experimental Results

In Fig. 2.6 are reported the experimental results compared with the predicted reduction by the squeeze film effect for the range of normal force applied by the user, $0.3N \pm 0.1$. The comparison shows the impossibility to obtain experimentally a perfect acoustic levitation for high vibration amplitude and the tendency of the friction to reach an asymptote not predicted by the squeeze film model. These preliminary results justified the developing of the following evaluation of the squeeze film hypothesis through the modification of the ambient pressure described in the next section.

2.2.3 Conclusion

In this first experimental assessment, a deviation of the measured tribological data from the prediction of the squeeze film effect model was recorded. This experiment motivated the design of the set of experiment in the following section to quantify the contribution of the squeeze film effect to the total friction modulation in ultrasonic devices.

2.3 Pressure Dependence of Friction Reduction for Ultrasonic Devices

In this section, a tribological assessment of the reduction of the friction between the finger, or the probe, and the plate in a reduced pressure environment is proposed. The

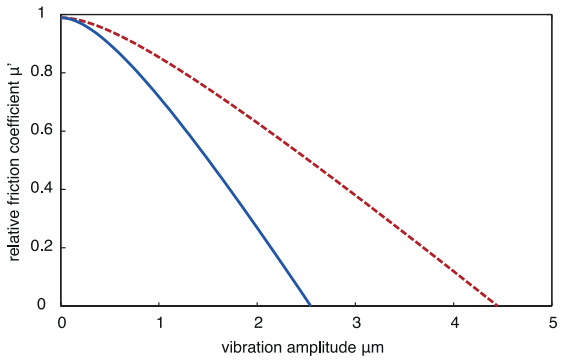

FIGURE 2.7: Predicted reduction of the friction for p_0 (continuous line) and $0.5p_0$ (dashed line)

aim of the experiment is to quantify the contribution of the squeeze film effect to the reduction of the friction in ultrasonic devices.

2.3.1 Pressure Dependence of Squeeze Film Assumption

As introduced in the previous section, the sustain force provided by the squeeze film effect depends on the total ambient pressure, Eq. 2.5. The dependence of the friction modulation predicted by the squeeze film model with the ambient pressure is represented in Fig. 2.7 and it can be exemplified by the parameter γ defined as:

$$\gamma = \frac{1 - \mu'(\omega, p)}{1 - \mu'(\omega, p_0)} \tag{2.10}$$

where p is the environmental pressure for the reduced pressure environment. The parameter γ identifies the expected variation of the amount of reduced friction in function of the atmospheric pressure, i.e. for a pressure of $0.5p_0$, the squeeze film model predicts $\gamma = 0.5$. This means that for $p = 0.5p_0$, half of the modulation of friction is expected if the squeeze film assumption is valid. This parameter gives a quantifiable parameter of the contribution of the squeeze film effect in the ultrasonic devices.

2.3.2 Finger Measurements

In this subsection, an experiment developed to quantify the influence of the squeeze film effect in ultrasonic device for a reduced pressure environment and a finger sliding on an ultrasonic plate is presented.

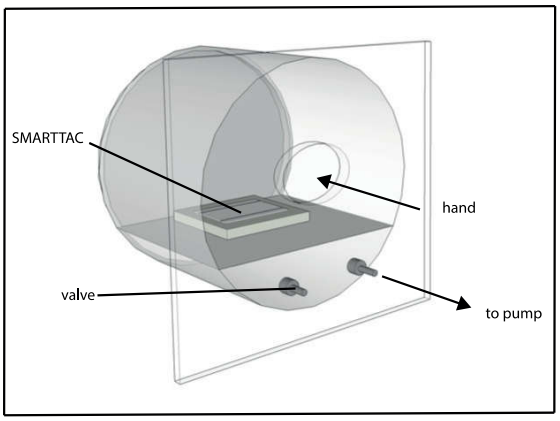

FIGURE 2.8: Representation of the experimental setup able to provide a reduced pressure environment for tribological experiment between the finger and the ultrasonic vibrating plate.

2.3.2.1 Experimental Setup

To investigate the influence of the pressure on the friction reduction performed by ultrasonic devices, a low-pressure chamber has been developed, Fig. 2.8. The necessity to ensure freedom of motion to the user finger while exploring the device in low-pressure leads to the implementation of a rubber glove inserted into the chamber. The index finger of the glove was cut and a custom made silicon joint between the finger and the glove was implemented to maintain the pressure gradient. The pressure reduction to $0.5p_0$ was provided by a pump (Piccolo, Thomas, Germany). The pressure was maintained stable with a valve. The first test showed the impossibility to perform the measure with a voltage controlled tactile stimulator, the reduction of the air damping in low-pressure environment made the variability of the stimulus too important. To solve this problem, a custom stimulator named SMARTTAC [61] was used. This device is controlled in closed loop in vibration amplitude to ensure the stability of the stimulus in the different operating conditions. It is also equipped with normal and lateral force sensors to measure in real time the friction between the finger and the plate. Its surface is made of plastic and can be considered topologically rough from a tribological point of view.

2.3.2.2 Experimental Protocol

To investigate the detectable range of vibration usually performed by ultrasonic devices, four different experimental conditions were tested; the plate was set to a vibrational amplitude between 0.5 and 2 µm with a step of 0.5 µm . For each trial, the friction was

TABLE 2.2: Normal force and Velocity Values

Vibration Amplitude	0.5 µm	1 µm	1.5 µm	2 µm
F_n for $P = p_0$	0.67 N	0.64 N	0.64 N	0.67 N
F_n for $P = 0.5p_0$	0.66 N	0.66 N	0.67 N	0.6 N
v for $P = p_0$	15.6 mm/s	15.7 mm/s	22.3 mm/s	17.6 mm/s
v for $P = 0.5p_0$	22.9 mm/s	24.0 mm/s	21.5 mm/s	21.0 mm/s

modulated at 2 Hz and the resulting force collected. The measurement was performed on the author of the thesis, who gave his informed consent at the participation to the experiment, a similar preparation procedure for the finger and the plate as reported in section 2.2.2.2 was employed. He was asked to explore the surface of the plate by maintaining constant normal force and constant exploration velocity, helped with a metronome. A lot of training was necessary before the starting of the experiment to obtain a similar exploration technique in low and ambient pressure.

2.3.2.3 Experimental Results

The lateral and normal force were analyzed similarly to the previous experiment to recover the relative friction coefficient in function of the pressure and the vibration amplitude. Due to the great variability of the applied normal force and exploration speed in the two different conditions of pressure, a window of normal force between 0.6 and 0.7 N was considered.

In Fig. 2.9a is reported the relative reduction of the friction coefficient in function of the vibration amplitude for the two ambient pressures analyzed. In Fig. 2.9b, the experimental γ parameter vs the theoretical one are compared in function of the vibration amplitude.

2.3.2.4 Discussion

In the performed experiment, a strong discrepancy of the expected γ parameter between the theoretical and experimental tribological measurement is highlighted. This suggest that others phenomena than the squeeze film effect may concur to the generation of the modulation of the friction. It is not possible to definitely conclude the quantitative contribution of the squeeze film effect on the total friction modulation based on this

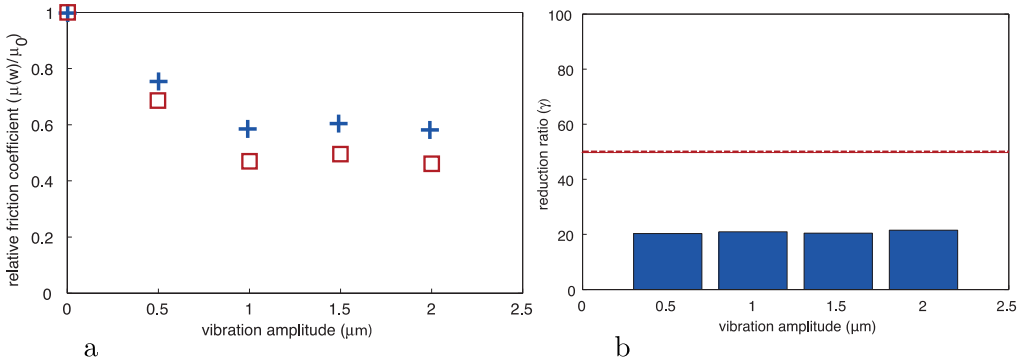

FIGURE 2.9: (a), Evolution of the relative friction coefficient as a function of the vibration amplitude for the two pressure values p_0 (squared) and $0.5p_0$ (cross). (b) Experimental γ parameter vs expected for the considered vibration amplitude.

experiment due to the impossibility to exactly reproduce the velocity of exploration, the normal force between the finger and the plate and the finger orientation for the two cases; moreover, it was shown in chapter 1 the dramatic changes that the frictional force between the skin and the surface undergoes for different environmental condition which may have affected the results. Being the experiment quite uncomfortable for the user and particularly challenging in the realization, a more systematic approach based on a tribometer developed for the reduced pressure environment was performed.

2.3.3 Probe Assessment

To address the problematics of the tribological investigation of the finger in a reduced pressure environment, a similar experiment employing a tribometer and an artificial probe is hereby described.

2.3.3.1 Experimental Setup

Tribometer To quantify the influence of the squeeze film mechanism, a special tribometer and a low-pressure chamber were designed in order to investigate the evolution of the frictional modulation as a function of the ambient pressure, Fig. 2.19a. The tribometer incorporated a 6-axis force sensor (nano 43, ATI, USA) that provides both lateral and normal force monitoring. The preloading of the axis can be tuned with a magnetic levitation system, and the lateral motion of the probe is provided by a linear ultrasonic motor (M-663, PI, Germany) coupled with a driver (C-184, PI, Germany). The vibrating device is a glass plate of 120 mm × 21 mm × 2 mm equipped with three

piezoceramic actuators used as a driver and one as a sensor; the resonant frequency is 27 389 Hz with a stable maximum in the centre. The pressure system consists of a cylindrical steel chamber with a removable transparent side. It was equipped with a vacuum pump (Piccolo, Thomas, Germany) and the inner pressure was measured by a manometer and regulated by a valve. It was necessary to implement a vibrational amplitude control system for the plate, which was similar to that described in [62], in order to ensure the consistency of the measurement condition between the different atmospheric pressures. Without the control system, the reduction in the air damping on the resonator generated a significant change in the Q factor of the vibrating system. This reduction, coupled with the mechanical noise induced by the frictional measurements resulted in an extremely unstable vibrational amplitude of the plate. The closed-loop control implemented on the plate stabilised the amplitude with a spatial resolution of 50 nm during the frictional measurements.

Ultrasonic Probe Due to the extreme difficulty of performing tribological measurements in controlled conditions for a finger sliding on an ultrasonic device in a reduced pressure environment, a probe exhibiting frictional modulation similar to that of a human fingertip was developed. It has a core of silicone rubber with dimensions of 16 mm × 13 mm × 10 mm, a Young's modulus of 1 MPa and rounded edges. In order to simulate the inner fingertip tissues, the contacting region was covered with a surgical tape having mechanical properties (Young's modulus of 20 MPa) and spatial periodicity similar to that of the fingerprint ridges. To establish that the behaviour of the probe is similar to that of a human finger pad, a tribometer (TRB, CSI, Switzerland) was used to record the frictional modulation experienced by the probe sliding on the ultrasonic device at an amplitude of 2.5 µm, a normal force of 0.5 N and an approximate sliding velocity of 17 mm/s. In addition, the velocity and acceleration of the probe and the finger pad under ultrasonic vibration were measured using the equipment described in the next sub-section for a vibration amplitude of 1.35 µm and an applied normal force is 0.25 N. Details about the finger pad and cleaning procedure are given in section 2.4.

2.3.3.2 Experimental Results

Probe Validation Fig. 2.11a shows that the reduction of the frictional force for the probe when subjected to ultrasonic vibration has reduced by a factor of ∼4. It also shows

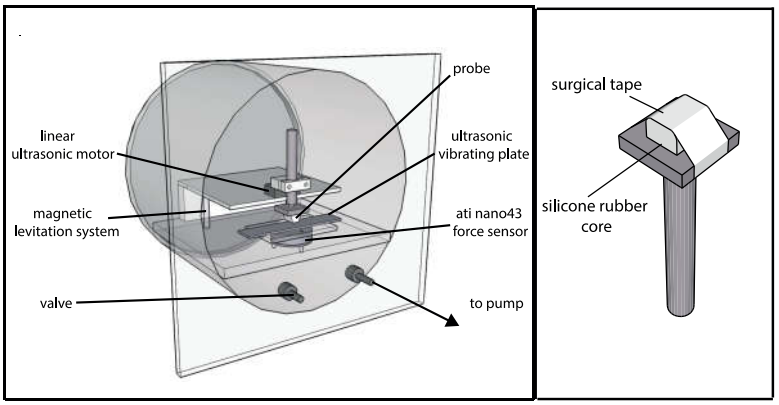

FIGURE 2.10: (a) Representation of the probe exhibiting friction reduction in the ultrasonic domain, (b) Schematic diagram of the tribometer in the pressure chamber.

data for the human finger pad acquired in the pre-experiment and for an another probe called Tango plus [63] which were both acquired under approximately similar conditions to those employed for the current probe. Tango plus has an external layer mimicking the *stratum corneum* and a porous inner structure exhibiting similar viscoelastic behavior to that of the inner tissues of the fingertip. The figure demonstrates that the probe exhibits a similar reduction in friction to the one observed for the human finger pad and Tango Plus. Fig. 2.11b shows a comparison of the velocity and acceleration of the plate, probe and finger pad. In terms of the phase shift relative to the plate and the magnitudes, the results are similar, see the next section for details on the concept of phase shift.

Tribological Results The frictional force of the probe as a function of the vibrational amplitude is given in Fig. 2.12 for the two normal forces investigated. The decrease in the frictional force with increasing amplitude is similar within experimental uncertainty for both the measurements carried out at atmospheric and reduced pressure. If the squeeze film effect was responsible of the reduction of friction at ambient pressure, a smaller modulation would be expected in the reduced pressure environment with a $\gamma = 0.5$ corresponding to the $p = 0.5p_0$. Moreover, the reduction in the frictional force at the reduced pressure is greater than that calculated based on the squeeze film mechanism.

2.3.4 Discussion

Based on these experimental assessment, a strong discrepancy between the predicted friction modulation by the squeeze film effect and the tribological assessment was found.

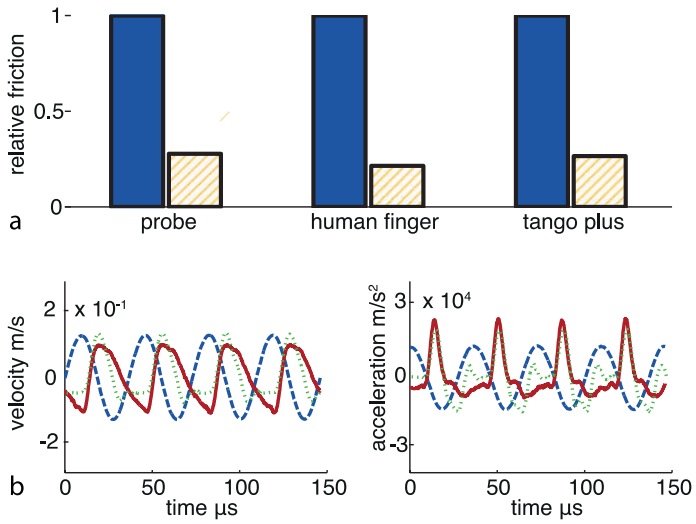

FIGURE 2.11: (a), Comparison between the relative friction reduction of the probe, human finger and the Tango plus due to ultrasonic vibration where the filled and dashed bars correspond to vibration off and on respectively. (b) The velocity and acceleration of the ultrasonic vibrating plate (dashed line), probe (dotted line) and the finger pad (continuous line) for a vibrational amplitude of 1.35 µm and applied normal force of 0.25 N.

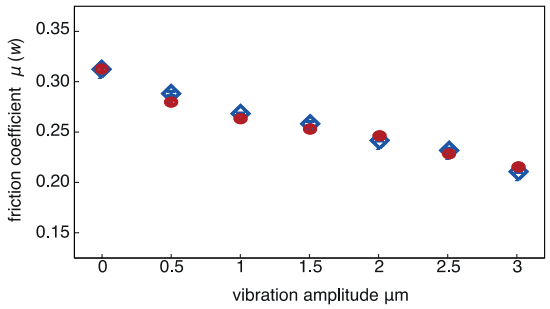

FIGURE 2.12: The coefficient of friction of the probe as a function of the vibrational amplitude under atmospheric (blue diamonds) and reduced (red circles) pressure. A normal force of 0.78 N was applied during these tribometric measurements.

In the next section, an investigation of the contact dynamics between the finger and the ultrasonic plate will be carried on, followed by the development of a finite element model of the fingerprint able to predict the experimental data. In the end, a mechanical explanation of the friction reduction in ultrasonic device is introduced through a simple ideal elastic model.

2.4 Skin-Plate Contact Dynamics

As said before, it seems necessary to have a good idea of the contact mechanisms between the plate and the finger. For this reason, in this section, the experimental setup developed to measure the skin-plate contact dynamic will be described.

2.4.1 Description of the Experimental Setup

The experimental equipment developed to measure the dynamics of the finger pad-plate contact in the ultrasonic domain is shown Fig. 2.13. The aim was to record the local velocity of the fingerprint ridges while in periodic contact with the ultrasonically vibrating plate. This was achieved using a laser Doppler vibrometer (OVF-5000, Polytech, Germany) that was focused on the surface of the finger pad across a transparent vibrating plate. The diameter of the laser focus spot was 120 µm, which is comparable with that of a fingerprint ridge ($\sim$ 300 µm); the ridges were coloured with reflective paint to enhance the signal-to-noise ratio. The procedure is similar to that described in [64]. The applied normal force between the finger and the plate was recorded by a force sensor (nano43, ATI, USA) mounted beneath the plate holder. The height of the whole structure could be adjusted using two micro-positioners (M-SDS40, Newport, USA) in order to control the normal force with an angle between the finger and the plate of 45°. The vibrational amplitude of the plate and the surface velocity of the fingerprint ridges were monitored by an oscilloscope (3014B, Tektronix, USA) and the applied force was acquired simultaneously through serial communication with a computer.

2.4.2 Measurement Protocol

The measurements were performed on the index finger of a male subject (age 26 years) who gave his informed consent. For each acquisition, the plate was cleaned with alcohol, and the finger washed with commercial soap, rinsed with water and dried with absorbent paper. There was a minimum delay of 3 min before performing any measurements to allow the finger and plate to equilibrate. The mean skin humidity of the finger pad was 35 a.u. as measured with a corneometer (CM 825, Courage + Khazaka electronic GmbH, Germany); this is defined as the humid condition. A dry condition was achieved by washing the finger pad with acetone using a similar procedure described

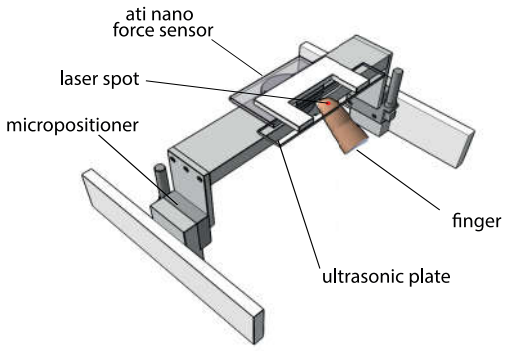

FIGURE 2.13: Schematic diagram of the equipment used to measure the contact dynamic between a finger pad and vibrating plate. The finger is inclined at an angle of 45° to the plate and the focus spot is visible on the skin surface.

previously [65, 66]. It may be noted that the different humidity conditions will influence the mechanical properties of the *stratum corneum*, allowing a parametric analysis. The dynamic behaviour of the skin in contact with the plate was recorded for different peak-to-peak amplitudes in the range 0 - 2.5 µm, which is generally implemented in ultrasonic displays [67]. The applied normal force on the finger was 0.25 ± 0.05 N. The required amplitude of vibration of the plate was initiated before contact with the finger pad was made, which was for a duration of 20 s. The measurements were performed multiple times for the two different humidity conditions of the finger. Each experimental point corresponds to 10 measurements in order to ensure the repeatability of the results.

2.4.3 Experimental Results

Typical experimental data for the displacement, velocity and acceleration of the finger pad and plate at peak-to-peak vibrational amplitudes of 0.42, 1.35 and 2.5 µm are presented in Fig. 2.14. The displacement values are calculated from the integration of the velocity measurements as a function of time, and thus it is not possible to specify an absolute value of the detachment time; the corresponding separation distances between the finger pad and plate are also shown. At an amplitude of 0.42 µm, the data for the plate and finger pad are in phase with identical amplitudes so that contact is completely maintained; this has been referred to as the *sticking regime* [63]. There is a phase lag of $\sim 90°$ at an amplitude of 1.35 µm that is accompanied by a significant period for which the finger pad is not in contact with the plate; this has been referred to as the

bouncing regime [63]. At the amplitude of 2.5 µm, the period of the finger displacement has doubled. The trends in the results may be quantified by calculating the phase shift $\Phi(w)$:

$$\Phi(w) = 360\frac{\mid t_{pa}(w) - t_{sa}(w) \mid}{t_c} \tag{2.11}$$

where w is the amplitude of vibration, t_{pa} and t_{sa} are the times of the maximum acceleration of the plate and the skin of the finger pad respectively, and the vibrational period.

The origin of the phase shift may be understood by considering the behaviour corresponding to the vertical dashed line in Fig. 2.14 that intersects the peak in the acceleration of the skin as it is impacted by the plate. Following such an impact, the skin will continue to be displaced away from the plate as the plate retracts. Eventually, the stored elastic energy in the skin will cause it to unload and re-contact the plate. The greater peak acceleration at the amplitudes of 1.35 and 2.5 µm results in larger deformations and impact displacements of the skin and hence a greater phase shift. Both the velocity and acceleration peaks for the skin are asymmetric and this arises from significant retardation during unloading, which could arise from either viscoelastic or inertial damping, or a combination of both effects. The dependence of the phase shift on the vibrational amplitude is shown in Fig. 2.16a. It evolves from a low value, corresponding to full contact between the finger pad and plate, to a saturated mean value, corresponding to intermittent contact, under high vibrational amplitudes for both the dry and humid conditions.

2.5 Finite Element Model

2.5.1 Introduction

To model the behaviour of the fingerprint ridges interacting with an ultrasonically vibrating plate, an FE model is developed. It was necessary to take into account the different characteristics of the tissues, the viscosity of the materials, and the dynamic contacting phenomenon. This work was performed in collaboration with Zlatko Vidrih and Vincenzo Giamundo, post-doc in the framework of the Prototouch Project.

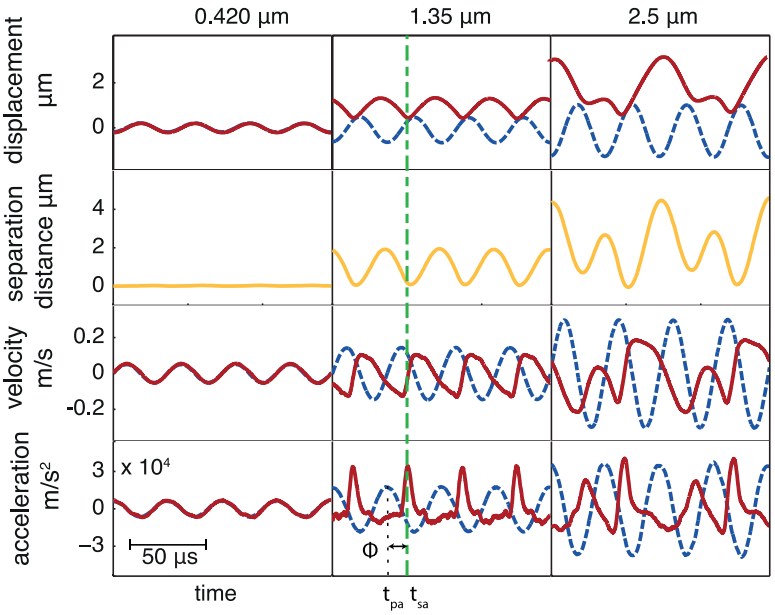

FIGURE 2.14: Displacement, separation distance, velocity and acceleration of the skin of the finger pad in the dry condition (continuous lines) interacting with an ultrasonic vibrating plate for three peak-to-peak vibrational amplitudes of 0.420, 1.35 and 2.5 µm; the data for the plate are shown as dashed lines. The applied normal force between the finger pad and the plate is 0.25 N. The green vertical dashed line indicates the concomitance of the peak of the acceleration with the beginning of contact between the finger pad and the plate once the intermittent contact is established.

A 2D linear viscoelastic model of a fingerprint ridge was generated to represent the three most external layers of the skin: the *stratum corneum*, *dermis* and subcutaneous tissues. Periodical boundary conditions were applied to the sides of the model in order to reproduce the periodicity of the fingerprint ridges on the human finger pad. A rigid boundary condition was set in the upper part of the model since the inner finger pad was considered to be immobile during the timescale of the vibrations as discussed in the introduction. The selected model parameters are presented in Table 2.3. The load applied on the single ridge was calculated by the pressure corresponding to an applied force of 0.25 N, assumed constant over the contact area. The gross contact area was calculated according to the relation reported in [40], and rescaled on the 2D model. A schematic diagram of the implemented example together with the boundary conditions is shown in Fig. 2.15.

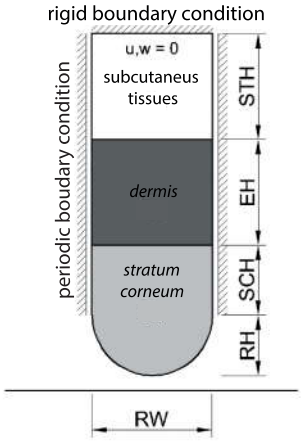

FIGURE 2.15: Schematic representation of the FE model of a fingerprint ridge. RW is the width of the ridge, RH the height of the ridge, and SCH, EH and STH are the thicknesses of the *stratum corneum*, *dermis* and subcutaneous tissues.

TABLE 2.3: Input material parameters for the FE model; common values of the Poisson's ratio, density and retardation time were assigned to the three domains of the skin [1–3].

Parameter	Description	Input Value or Optimization Range
RH	*stratum corneum* ridge height	200 µm
SCH	inner *stratum corneum* thickness	100 µm
EH	*dermis thickness*	600 µm
STH	subcutaneous tissues thickness	1800 µm
RW	width of the ridge	500 µm
μ_0	coefficient of friction without vibration	0.1 - 2.0
k	penality parameter	(10-1000) E_sc
E_{sc}	Young modulus of *stratum corneum*	10-1000 MPa
E_{ep}	Young modulus of *dermis*	1.5 MPa
E_{ep}	Young modulus of subcutanous tissue	0.02 MPa
G_{sc}	shear modulus	$E_{sc}/2(1+\nu)$
ν	Poisson's ratio	0.33
r	density	750 kg/m^3
τ	retardation time	$0-10s$
ζ	Rayliegh damping	1
f	plate frequency	27500 Hz
w	plate amplitude	$0.05-2.5$ Hz
F_n	normal force applied by the fingerpad	0.25 N

2.5.2 Implementation

The explicit solver version of the commercially available FE analysis software Elfen (Rockfield Software Ltd., Swansea, UK) was employed. Four-noded plane strain quadrilateral hourglass elements [68] with strain stabilization were utilized to discretise the geometry. These 2D continuum elements are based on the standard isoparametric approach where the same shape functions are used to interpolate both the displacements and the geometry. The strain-displacement relationship was formulated using a velocity-strain measure, from which the incremental strains were evaluated. The elements use one-point integration, consequently the four-noded elements have stabilization terms to limit zero-energy or hourglass deformations. The elements also utilise an artificial bulk viscosity to smooth shock discontinuities that may occur during impact problems. The contact between the skin and the plate was modelled using the penalty method with Columbic friction [69], where the plate was assumed to be rigid in comparison with the fingerprint ridge. This boundary condition was applied globally rather than locally and thus the ridge may be regarded as having a sufficiently fine-scale roughness that it exhibits Hertzian deformation to a close approximation [70]. If the boundary condition was applied locally, the ridge would exhibit the characteristics of a smooth Hertzian contact such that the coefficient of friction would decrease with increasing normal force [71]. The influence of the penalty parameter, k, was investigated for optimisation purposes since it introduces an additional stiffness in the dynamic model. It was estimated that for $k > 80E_{sc}$, its influence on the model dynamics is negligible. The viscoelastic properties of the skin were parameterized by a retardation time, τ. The analyses were implemented in parallel with a Matlab code on multiple cores of a desktop computer (Intel i7 Six Core Processor, 3.4 GHz, and 16 GB RAM, DDR3 2400 MHz). Matlab was used to generate the input files for Elfen and for reading and post-processing the output files.

2.5.3 Inverse Analysis

The complex nature of biological tissues results in a huge variability in the mechanical properties of the skin. Moreover, FE modelling requires additional numerical parameters that are not physically related. In order to find reliable model parameters that lead to an accurate simulation of the experimental phenomena, an inverse modelling procedure was

adopted [72–74]. In particular, the procedure aims to identify a set of parameters that, according to the chosen accuracy, allows the numerical model to fit the experimental behaviour. Here, the fitted parameters were the viscoelastic behaviour of the model (the retardation time), and the Young's modulus of the *stratum corneum* to reproduce the two conditions experimentally studied. These parameters are highly variable or unknown in the ultrasonic range. Moreover, the k parameter, which has no physical meaning, is also fitted, but it has to fulfill the requirements previously expressed. This goal is achieved by minimizing a function (i.e. an objective function) that returns the difference between the experimental and the numerical data (i.e. the misfit).

Theoretically, the associated optimization problem can be written as:

$$\text{minimize } f(p_1, ..., P_n) \tag{2.12}$$

$$\text{subject to } c_1 \leq b_1, ..., c_m \leq b_m \tag{2.13}$$

The elements of the vector $p = (p_1, ..., p_n)$ are the unknown parameters, the function f is the objective function and the functions $(c_1, ..., c_m)$, are the constraint functions and $(b_1, ..., b_m)$ are the limits, or bounds for the constraint functions.

The phase shift parameter, Φ, was selected as a fitting function since it effectively characterises the skin behaviour accordingly of the vibrational amplitude. The objective function to be minimised is:

$$\text{Objective } = \sum_{i=1}^{N} \left[\Phi(w)^{FEM}(E_{sc}, k, \tau) - \Phi(w)^{expt}\right]^2 \tag{2.14}$$

where N is the number of experimental points included; $\Phi(w)^{FEM}(E_{sc}, k, \tau)$ is the phase shift calculated at the amplitude w and $\Phi(w)^{expt}$ is the experimental phase shift measured at the same amplitude. The model was implemented with an initial dwell time between the finger pad and plate, t_{press}, then held in position until a time, t_{on}, when the vibrational amplitude of the plate was increased to the first value assumed in the experimental evaluation and maintained for a time, t_{step}. The dynamics of the contact nodes in terms of displacements, velocity and accelerations were recorded in output files and post-processed to calculate the phase shift, Φ, for a given amplitude using Eq. (2.11). The procedure was repeated for all vibrational amplitudes measured to compute $\Phi(w)^{FEM}(E_{sc}, k, \tau)$ for a given set of parameters. Then, the objective function was

TABLE 2.4: Inverse Analysis Results

Parameter	Description	Wet	Dry
E_{sc}	Young's modulus of *stratum corneum*	28.3 MPa	202.4 MPa
τ	retardation time	0 s	0 s
k	penalty parameter	93.8 MPa	144.6 MPa

evaluated and the procedure was terminated in case of convergence or repeated with a different set of parameters.

The convergence parameters obtained by the inverse analysis method for both humidity conditions of the finger pad are reported in Table 2.4. For both skin conditions, it was found that the retardation time did not significantly affect the results. Consequently, the simple elastic case ($\tau = 0$) was selected. The comparison between experimental and simulated phase shift data for the best-fit parameters is reported in Fig. 2.16a and the surface profile of the phase shift as a function of the vibrational amplitude and the Young's modulus of the *stratum corneum* is shown in Fig. 2.16b. The comparison between the experimental data and those calculated by the FE analysis using the optimised data for the dry case and the vibrational amplitude of 1.35 µm is illustrated in Fig. 2.17; the trends are similar for the humid case. In the case of the measured data (Fig. 2.14), the asymmetry of the calculated velocity peak is also evident. Since the model is elastic rather than viscoelastic the asymmetry is due to inertial damping (mass) only; in the absence of inertial damping the linear sloping component of the unloading phase would be horizontal. The difference between the measured and modelled data arises by the reporting of the velocity of one node of the model, whereas the measured data is the result of integrating along all the area of the ridge.

2.5.4 Results of the Finite Element Analysis in Sliding Conditions

The previous paragraphs allowed the parameterization of the FE model based on experimental data, in this section the model will be used to study the sliding condition.

To investigate the friction between the ultrasonically vibrating plate and the fingerprint model, the following procedure was adopted: (i) from 0 to t_{press} a constant normal load is applied to the finger pad as a boundary condition and the contact with the plate is fully established, and it is allowed to stabilise until $t = t_{slide}$, (ii) an additional boundary

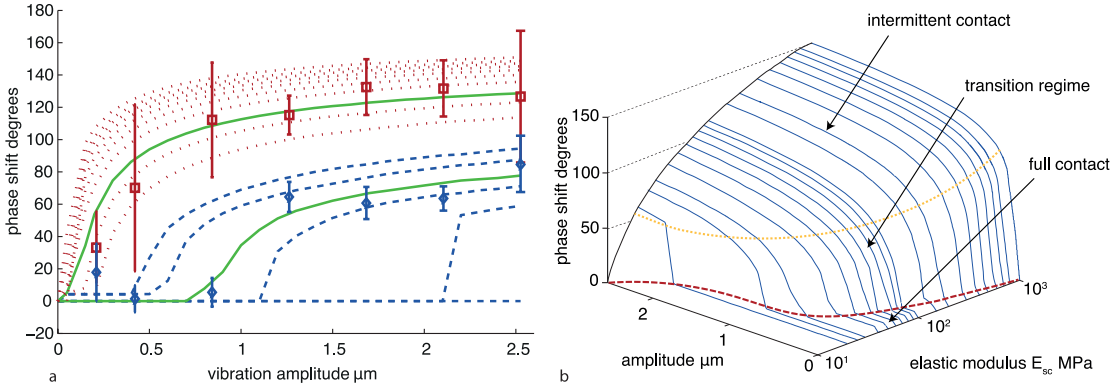

FIGURE 2.16: (a) The measured phase angles as a function of the vibrational amplitude under dry (red squares) and humid (blue diamonds) conditions. The corresponding calculated values using the FE modelling are also shown as the blue dashed and red dotted lines respectively. Each line corresponds to a different value of the Young's modulus of the *stratum corneum* varying, for the humid condition, between 20 (lower line) to 50 MPa (upper line). The Young's modulus for the dry condition varies between 100 (lower line) to 1000 MPa (upper line) [2]. The continuous green lines are the best fits of the calculated values to the measured results and correspond to Young's moduli of 28.3 and 202.4 MPa respectively. (b) Phase shift as a function of the Young's modulus of the *stratum corneum* and the vibrational amplitude calculated by the FE analyses. The lowest region corresponds to continuous full contact between the finger pad and plate (sticking). The intermediate region refers to the transition phase, where the skin and the plate start to exhibit intermittent contact that is fully developed in the upper region (bouncing).

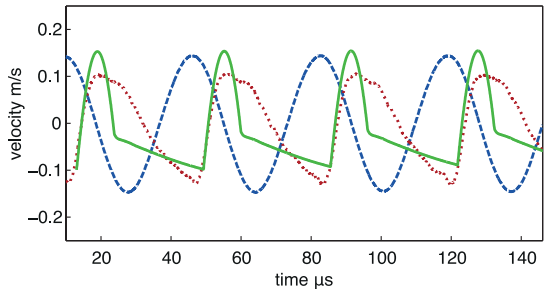

FIGURE 2.17: Comparison between simulated (continuous green line) and measured (dotted red line) velocities of the finger print ridge (dry case) for a vibrational amplitude of 1.35 µm; the plate velocity is plotted as a dashed blue line; the velocity corresponds to one node at the base of the ridge.

condition is then imposed corresponding at $t = t_{slide}$ corresponding to a lateral velocity, U, and (iii) at $t = t_{on}$ the plate is vibrated with a given amplitude, as shown in Fig. 2.18.

The integral mean coefficient of friction, $\mu(w)$, derived from the finite element simulations is calculated as the ratio of the mean values of the lateral force, F_l, and the normal force between the skin and the plate , F_{reac}, over a vibrational period T:

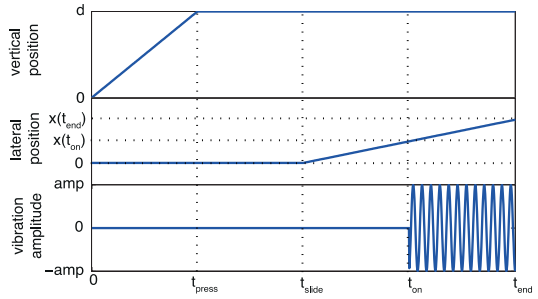

FIGURE 2.18: Loading conditions for the FE examples.

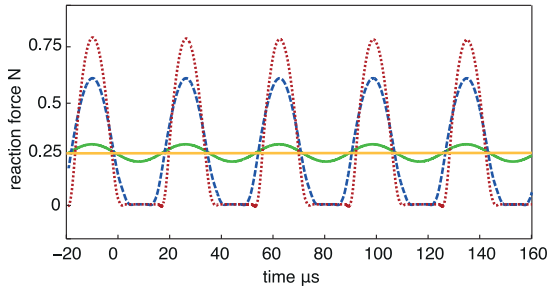

FIGURE 2.19: Reaction force between the plate and the ridge calculated using the FE analysis under a normal force of 0.25 N applied without vibration (horizontal fawn line) and with different peak-to-peak vibrational amplitudes of 0.1 (continuous green line), 1 (dashed blue line) and 2 (red dotted line) µm.

$$\mu(w) = \frac{\int_t^{t+T} F_l(w)dt}{\int_t^{t+T} F_{reac}(w)dt} \tag{2.15}$$

Fig. 2.19 shows the plate reaction force as a function of time for three vibrational amplitudes calculated by the FE model. The data are consistent with the measured values of the separation distances shown in Fig. 2.14. That is, at an amplitude of 0.1 µm, the force is always positive since the finger pad remains in contact with the plate. At an amplitude of 1 µm, there is a significant period when $F_{reac} = 0$ corresponding to a loss of contact. In addition, the maximum normal force exceeds the applied value and this arises because there are an impacts between the plate and the finger pad, which is modelled as a fingerprint ridge of finite mass, as discussed in the context of the bouncing regime in section 2. The duration of non-contact increases at an amplitude of 2 µm and the maximum reaction force is also greater than at the amplitude of 1 µm. However, when calculating the integral mean value of F_{reac} over a vibration cycle, it is found to be constant for all three amplitudes and it is equal to the applied normal force of 0.25

N. This results confirms the statement in the introduction section and as a consequence:

$$\mu(w) = \frac{\int_t^{t+T} F_l(w)dt}{\int_t^{t+T} F_{reac}(w)dt} \tag{2.16}$$

The integral mean coefficient of friction, $\mu(w)$, derived from the FE simulations is calculated as the ratio of the mean values of the lateral force (friction force), F_l, and the normal force between the skin and the plate , F_{reac}, over a vibrational period T:

$$\int_t^{t+T} F_{reac}(w)dt = \int_t^{t+T} F_{reac}(0)dt \tag{2.17}$$

Thus the mean relative coefficient of friction, $\mu(w)' = \mu(w)/\mu_0$, can be calculated as:

$$\mu(w)' = \frac{\int_t^{t+T} F_l(w)dt}{\int_t^{t+T} F_{reac}(w)dt} \frac{\int_t^{t+T} F_{reac}(0)dt}{\int_t^{t+T} F_l(0)dt} = \frac{\int_t^{t+T} F_l(w)dt}{\int_t^{t+T} F_l(0)dt} \tag{2.18}$$

where μ_0 is the intrinsic coefficient of friction when $w = 0$. Fig. 2.20 shows (i) F_{reac} as a function of time for a single period from the data in Fig. 2.19 with an amplitude of 1.35 µm and (ii) the frictional force, $\mu_0 F_{reac}$, assuming that slip occurred directly after contact. However, the value calculated by the FE analysis is much less than $\mu_0 F_{reac}$ since when contact is made, the ridge deforms laterally rather than slips. The deformation is Hertzian so that initially, just after the contact, the lateral force is small since the contact area is small. With increasing normal load, the contact area increases and thus the lateral force increases until it is equal to $\mu_0 F_{reac}$, and then slip will be initiated. In principle, the subsequent time evolution of the lateral force should be governed by $\mu_0 F_{reac}$ but it continues to be greater than the slip value because of inertial overshoot, and the value slowly decreases until it becomes zero when contact is lost. The reduction of friction arises by the reduced area under the frictional curve represented in Fig. 2.20.

To investigate the influence of the various parameters on the attenuation of the friction, multiple simulations were performed under the loading conditions represented in Fig. 2.20 as function of the vibration amplitude. The influence of the vibrational frequency, Young's modulus of the *stratum corneum*, intrinsic coefficient of friction, normal load and exploration velocity on the frictional force were evaluated. The results of the parametric studies are shown in Fig. 2.21. The reduction in the friction is particularly sensitive to the vibrational frequency, intrinsic coefficient of friction and the sliding velocity. The

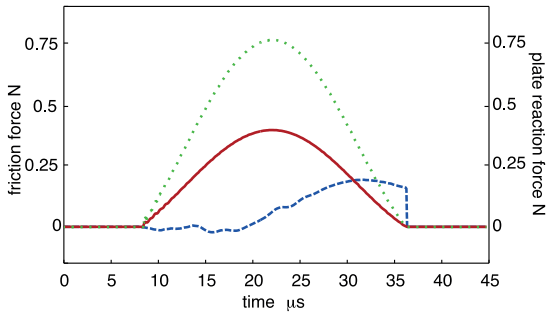

FIGURE 2.20: FE results for the friction between a ridge in contact with an ultrasonic vibrating plate for one period of vibration. The dotted green line is the plate reaction force F_{reac}, the continuous red line is the value of $\mu_0 F_{reac}$ with μ_0= 0.5, and the dashed blue line is the lateral force acting on the ridge nodes in contact with the plate. The simulation has been carried for a vibrational amplitude of 1.35 µm, an applied normal force of 0.25 N and a sliding velocity of 20 mm/s.

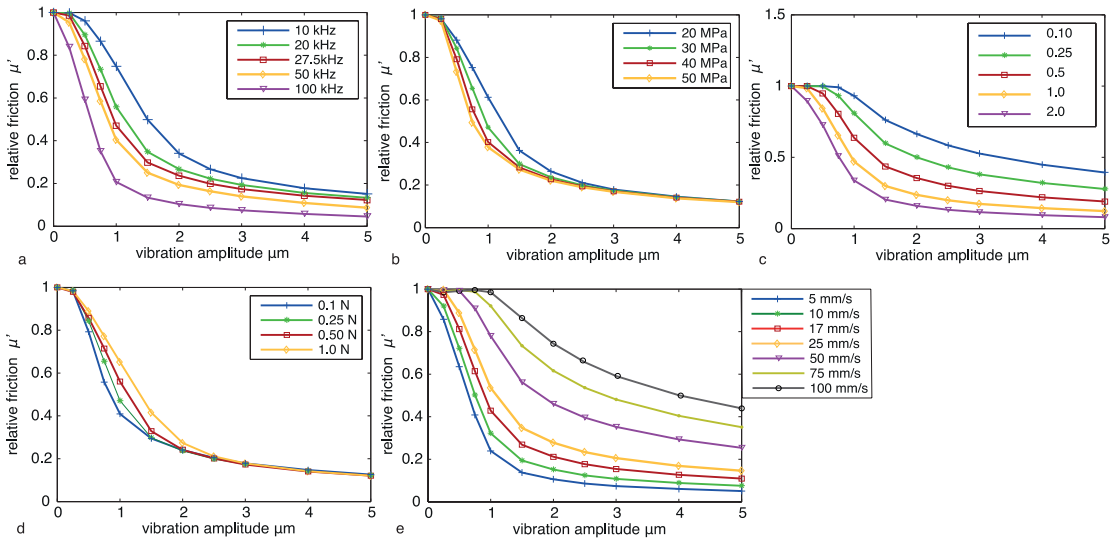

FIGURE 2.21: The relative coefficient of friction as a function of the vibrational amplitude for a range of the following parameters: (a) vibrational frequency, (b) Young's modulus of the *stratum corneum*, (c) intrinsic coefficient of friction, (d) applied normal force, and (e) exploration velocity. These data were calculated by the FE analysis and, unless stated otherwise, the material input parameters are those identified through the inverse analysis for the humid case (Table 2); the exploration speed is 20 mm/s, the applied force is 0.25 N, μ_0 = 0.5 and the vibrational frequency is 27.5 kHz.

origins of these trends will be considered in the next section assisted by a spring-slider model that assists the interpretation.

2.5.5 Discussion

A combination of experiment and modelling was employed in the current work to investigate the role of intermittent contact. Laser Doppler vibrometry data, which quantified the velocity of displacement of a finger pad and an ultrasonic device, showed that there

was an increase in the phase shift, $\Phi(w)$, with increasing vibrational amplitude. At small amplitudes, the finger pad and plate are in phase but there is an increase in the phase shift with increasing amplitude. For extreme vibrational amplitudes (2.5 µm peak-to-peak in the current work), a doubling of the contact period was observed, in accordance with the measurements performed by Dai et al [64]. The effect is more pronounced for the finger pad in the dry state for which the *stratum corneum* is less plasticised by moisture and hence stiffer than in the humid state. The analysis of the period doubling is outside of the scope of this chapter, which is focussed on the main mechanism leading to the friction modulation. The transition from persistent or sticky contact to intermittent or bouncing contact in the state occurs at a peak-to-peak amplitude range of 0.4 - 0.8 µm compared with 0.8 - 1.3 µm for the humid state. The FE simulations involved a larger value of the Young's modulus of the *stratum corneum* for the dry compared with the humid state. On this basis it was possible to capture the observed trends of the measured phase shift data as shown in Fig. 2.16(a). The developed model assumed that a rigid upper boundary condition could be applied. Recent studies suggested that the viscoelasticity of the subcutaneus tissues plays a fundamental role in reducing the friction [63, 75], while the behaviour as a function of vibrational frequency suggests an effectively rigid response of the finger pad at the high frequencies associated with ultrasonic devices [76]. This is consistent with the assumption made in the current work that the preloading of the inner tissue is treated as irreversible within the timescale of the vibrations.

The input parameters for the FE model were optimised to reproduce the behaviour on the finger pad as represented by the measured phase shift data. The sliding results confirmed that the developed model exhibits a reduction of friction while sliding on an ultrasonic vibrating plate. For these reasons, a fully mechanical interaction can explain the friction reduction in ultrasonic device.

The squeeze film effect is the classic explanation of the friction modulation for ultrasonic devices. It relies on a net increase in the air pressure to decrease the friction. The limitations of this mechanism have been discussed in [67] with respect to the prediction that the friction tends to zero with increasing vibrational amplitude at a value of ~ 2 µm rather than to the finite value that is observed experimentally at a corresponding amplitude and frequency. Moreover, (i) it would be expected that the reduction in friction would be independent of the sliding velocity, which contradicts the results of the

current modelling (Fig. 2.21(e)) and the experimental data reported in part 2 and (ii) the current work provides more direct evidence than the squeeze film mechanism since no friction increase is observed under a reduced atmospheric pressure. To highlight the governing parameters of the interaction, a massless spring-slider model is hereby introduced.

2.6 Spring Slider Model

In this section, a simplified ideal elastic model is introduced to highlight the keys elements underlying the friction reduction for ultrasonic devices. The mechanical principle may be interpreted by such a model based on a Coulombic slider attached to lateral and normal linear springs, with stiffnesses k_l and k_n respectively. As proposed in [77], the slider may be considered to represent a fingerprint ridge that is attached to a rigid finger pad. It is assumed that the static compression of the normal spring is less than that of the vibrational amplitude. If the slider has finite mass, this coupled spring system requires a numerical solution. However, the aim of the model is to provide a qualitative interpretation that facilitates an explanation of the underlying physics. Thus it is sufficient to treat the slider as having zero mass, which only influences the second order effects of inertial damping and overshoot. Given an applied normal force, F_n, between the slider and plate, the normal preloading can be calculated as:

$$h = \frac{F_n}{k_n} \tag{2.19}$$

When the plate is vibrating with a sinusoidal profile, the amplitude of vibration, w must be greater than h in order to induce detachment of the spring. It is then possible to define a critical vibrational amplitude, w_c, corresponding to a normal force F_{nc}:

$$w_c = \frac{F_{nc}}{k_n} \tag{2.20}$$

For $w < w_c$, the spring and plate are in full contact over the whole vibrational period, whereas for $w > w_c$ the contact is intermittent. At equilibrium, the mean integral of the imposed force by the normal spring must be equal to the total reaction force of the

plate over a vibration cycle by analogy with Eq. 2.16:

$$\int_t^{t+T} F_{reac}(w)dt = \int_t^{t+T} F_{reac}(0)dt = F_n T \tag{2.21}$$

where T is the period of vibration. For any given sliding velocity, U, the out-of-contact coefficient of friction is zero and it is equal to μ_0 when contact is made. Initially, after contact is re-established, the lateral displacement of the plate is accommodated by compression of the lateral spring and thus the frictional force will increase linearly with the compression until the spring force is equal to the frictional force. Thus slip will occur at a critical compression, Δx_c:

$$\Delta x_c(w,t) = \frac{\mu_0 F_{reac}(w,t)}{k_l} \tag{2.22}$$

For a given vibrational amplitude, the time at which the slip occurs, t_s, can be defined as:

$$t_s = \frac{\Delta x_c(t_s)}{U} \tag{2.23}$$

Provided that $t_c > t_s$, where t_c is the total contact time, it is possible to recover the frictional force as function of time, $F_l(t)$, for each vibrational period:

$$F_l(t) = U t k_l \quad \text{if} \quad 0 < t < t_s \tag{2.24}$$

$$F_l(t) = \mu_0 F_{reac} \quad \text{if} \quad t_s < t < t_c \tag{2.25}$$

$$F_l(t) = 0 \quad \text{if} \quad t_c < t < T \tag{2.26}$$

The preloading of the lateral spring is removed when it detaches from the plate and thus it is fully unloaded when contact is re-initiated. The visualization of this simple model for an established intermittent contact is shown in Fig. 2.22 The periodicity of the contact generates the reduction in friction that is experienced while interacting with ultrasonic devices. This figure reproduces the trends calculated from the FE analysis shown in Fig. 2.20 except that the loading is linear rather than Hertzian and that inertial overshoot is absent.

In order to be a realistic representation, the spring-slider model should be able to reproduce the measured trends in the vibrational amplitude dependence of the phase shift as shown in Fig. 2.17a. The period of vibration of the plate is defined as $[w/2\sin(2\pi f t)]$

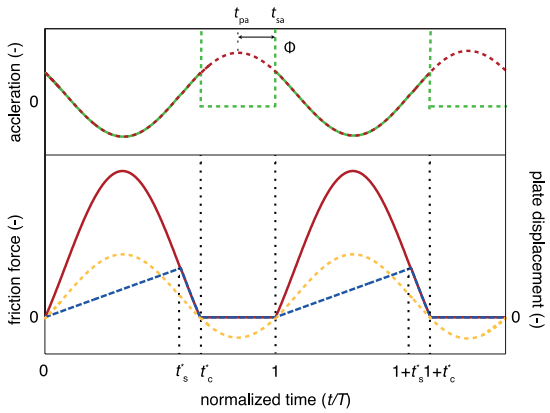

FIGURE 2.22: Explanation of the reduced friction of an elastic body periodically in contact with a vibrating plate; the frictional force as a function of time was calculated using the spring-slider model where $t^*_s = t_s/T$ and $t^*_c = t_c/T$. The continuous red lines are determined by $\mu_0 F_{reac}$ i.e. the frictional force that would be generated if Coulombic slip occurred throughout each cycle. The dashed blue lines correspond to the lateral force on the elastic body at the interface with the vibrating plate. The dotted black vertical lines denote the duration for which there is Coulombic slip. The dashed red line is the acceleration of the plate as a function of time. The dashed green line is the acceleration of the elastic body; the acceleration has a maximum value at a time just before it separates from the plate and then the value is instantaneous zero since the body has zero mass. The phase shift is defined as the lag of the peak acceleration of the elastic body relative to that of the plate.

where f is the frequency and the time interval for a single period is $T = 1/f$. The plate reaction force was calculated for a single period as the sum of the elastic preloading of the normal spring, h, and the elastic force induced by the vibration of the plate:

$$F_{reac}(t) = k_n w \sin(2\pi f t) + k_n h \tag{2.27}$$

such that $F_{reac}(t) > 0$ when the plate is in contact and $F_{reac}(t) = 0$ when the plate is out of contact. Eq. 2.21 may be written in the following form:

$$\int_0^{t_c} F_{reac}(t)dt = F_n T \tag{2.28}$$

The integral in Eq. 2.28 was evaluated numerically for different values of h using the Newton-Cotes method until there was convergence to the value of the right-hand side. The time required for contact, t_c was determined by substituting the converged value of h in Eq 2.27 and this corresponds to that for the maximum acceleration of the slider. The phase shift was calculated from Eq. 2.11 with t_{sa} being the time of contact between the plate and the slider; the results are shown in Fig. 2.23. In order to obtain values that were comparable to those measured (Fig. 2.16), it was necessary to input a range of

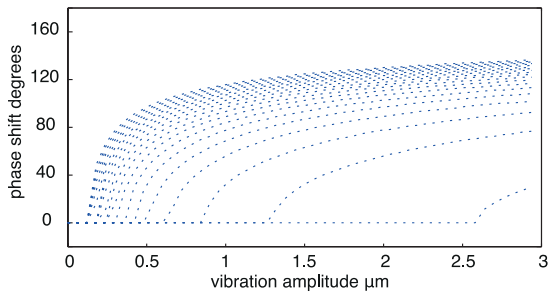

FIGURE 2.23: Phase shift calculated using the spring-slider model for spring stiffnesses in the range from 0.2 (lower line) - 4 MN/m (upper line) for an applied normal force of 0.5 N.

normal spring stiffnesses (0.2 - 4 MN/m) that is orders of magnitude greater than those measured ($\sim$ 2 kN/m) for the finger pad at much lower frequencies [76]. This reflects the much more rigid response at ultrasonic frequencies.

2.6.1 Parametric Analysis

The spring-slider model is able to provide a simple rationalisation of the FE data shown in Fig. 2.21. It demonstrates that the main mechanism leading to friction modulation for ultrasonic devices is analogous to a frictional ratchet in which periodic engagement and escape are induced by the normal vibration. The displacement of the slider is initially accommodated by compression of the lateral spring so that the frictional force is less than the sliding value. In summary, the friction increases in proportion to the compression of the lateral spring but the maximum force that can be generated depends on the frictional mobilisation time, t_s, which depends on the duration of contact, t_c. Consequently, the frictional force decreases with increasing frequency (Fig. 2.21a) due to the reduction in t_c. It increases with increasing sliding velocity (Fig. 2.21e) since the lateral deformation rate, and hence that of the lateral force, increases. The relative friction decreases as μ_0 increases (Fig. 2.21c) since the time to satisfy the slip condition increases.

For a given normal force, the static compression of the normal spring will increase with decreasing stiffness so that the value of t_c will increase. However, the lateral force depends on the shear elastic modulus of the stratum corneum, which is related to the Young's modulus by $G = E_{sc}/2(1+\nu)$. Thus the reduction in t_c is partly compensated by a relative increase in lateral stiffness that increases the rate of increase of the lateral force. Fig. 2.21b suggests that this is approximately the case for $>$ 2.5

µm, which corresponds to the asymptotic region of the phase shift in Fig. 2.16a. Thus provided that intermittent contact is fully established at large vibrational amplitudes, the data suggests that the friction is relatively independent of the absolute value of the Young's modulus. However, at smaller vibrational amplitudes, an increase in t_c due to a reduction in the normal stiffness is more important than the corresponding reduction in the lateral stiffness. A similar explanation is applicable to the normal force dependency (Fig. 2.21d). An increase in the normal force increases the lateral force required to induce slip. However, the increase of the static compression of the normal spring with increasing normal load causes an increase in t_c, which is a more dominant effect for vibrational amplitudes < 2.5 µm.

2.7 Dimensionless Group

2.7.1 Dimensionless Group

A dimensionless group is useful for summarising the governing parameters of a system and allowing data superposition. A necessary condition for $\mu' < 1$ is that $t' < 1$ where $t' = t_c/T$. Then μ' depends on the ratio $\Psi = t_c/t_s$ such that $\mu' = 0$ when $t_s = t_c$, and $\mu' = 1$ when $t_s = 0$. It is not possible to write a closed-form solution for the current system and thus any dimensionless group that is derived will be accurate to first order, such as $t_c \approx F_{reac}/(k_n w)T = F_{reac}/(k_n w f)$ and $t_s \approx F_{reac}\mu_0/k_l U$. Thus the dimensionless group Ψ may be written as:

$$\Psi = \frac{F_{reac}}{k_n w f}\frac{k_l U}{F_{reac}\mu_0} = \frac{k_l U}{k_n w f \mu_0} \tag{2.29}$$

Since for a finger pad, a common contact area for the two springs is involved [77], Eq. 2.29 may be written as:

$$\Psi = \frac{G_{sc}U}{E_{sc}wf\mu_0} \sim \frac{U}{wf\mu_0(1+\nu)} \tag{2.30}$$

A first order rate equation exponential function provides the simplest scheme for data superposition:

$$\frac{d\mu}{d\Psi} = b(\mu_0 - \mu) \tag{2.31}$$

where b is a system constant. Eq. 2.31 may be written in terms of the relative coefficient of friction as follows:

$$\frac{d\mu'}{d\Psi} = b(1-\mu') \tag{2.32}$$

By integrating subject to the boundary condition $\mu' = 0$ at $\Psi = 0$, the solution may be written in the following form:

$$\mu' = [1 - exp(\Psi/\Psi^*)] \tag{2.33}$$

where Ψ^* is the characteristic value of Ψ . The data in Fig. 2.21 change systematically with the independent variables except for the Young's modulus of the *stratum corneum* (Fig. 2.21b) and the applied normal force (Fig. 2.21d) which converge to single trend lines with increasing amplitude. At smaller amplitudes, it may be concluded that the relative friction is sensitive to the compressive displacement, as governed by the normal stiffness or applied normal force, since the intermittent contact is in the transition regime. Fig. 2.24 shows a plot of μ' as a function of Ψ and the best fit to Eq. 2.33 with $\Psi^* = 2.38 \pm 0.21$. The data correspond to those in Fig. 2.21 for a range of vibrational amplitudes, frequencies, exploration velocities, and intrinsic coefficients of friction. It also includes data for the Young's moduli and applied normal forces for amplitudes > 1 µm; the data at smaller amplitudes diverge from the correlation since there is a significant dependence on these parameters that is not taken into account in the definition of the dimensionless group. Thus Eq. 2.33 provides a reasonable representation of the data in reduced variables, particularly given the wide range of each variable that has been included.

Fig. 2.24 provides fundamental design guidelines for ultrasonic tactile devices. To obtain a large reduction of friction, small values of the dimensionless group are required. Thus, accounting for (19), it is possible to understand that the relevant parameters are (i) the vibrational amplitude as is well known, but also (ii) the vibrational frequency, and (iii) the intrinsic friction coefficient. The other parameters, exploration velocity, skin parameters, and normal load, are not controllable by a device designer.

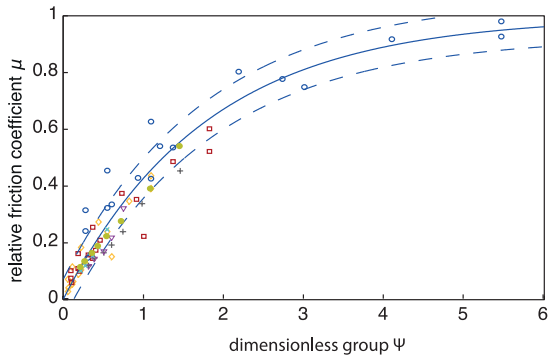

FIGURE 2.24: Relative coefficient of friction as a function of the dimensionless group, $U/wf\mu_0(1+\nu)$, for peak-to-peak vibrational amplitudes, w, of 1 (blue circles), 3 (red squares), and 5 µm (yellow diamonds), applied normal forces, F_n, of 0.1 (full green dots) and 1 N (light blue crosses), Young's moduli, E_{sc}, of 20 (purple triangles) and 50 MPa (grey crosses) frequencies in the range f =10 - 100 kHz, sliding velocities in the range U = 5 - 100 mm/s, and intrinsic coefficients of friction in the range = 0.1 - 2 . Unless indicated, $\mu_0 = 0.5$, $U = 20$ mm/s, $f = 27.5$ kHz, $E_{sc} = 28.3$ MPa and $F_n = 0.5$ N. The dashed lines correspond to the RMSE of the fit. The data are taken from Fig. 9 with those for the Young's modulus and applied normal force at amplitudes > 5 µm being omitted.

2.7.2 Influence of the Viscoelasticity

Both the current FE and spring-slider models demonstrate that it is not necessary to invoke viscoelastic deformation of the ridges to account for the reduction in friction. However, the optical measurements and the FE results (Fig. 2.17) show that inertial damping has a significant effect on the unloading and it may be speculated that a component of the measured damping arises from viscoelasticity, which could also retard the lateral recovery of the ridges following loss in contact. The aim of this section is to examine the influence of viscoelasticity on the reduction of friction. While a spring-dashpot-slider model could be developed, albeit with the introduction of increased complexity and additional input parameters, it is straightforward to examine the effect of retarding the recovery of the lateral spring by incorporating a constant unloading velocity as shown in Fig. 2.25. Initially, the effect is relatively large but there is an accumulation of the pre-contact unloaded lateral displacement that results in a transient increase in the friction to an asymptotic value that is slightly less than that corresponding to slip for the whole contact duration, $\mu_0 F_{reac}$. These calculations were extended to a range of exploration velocities. The results show that the steady state relative coefficient of friction decreases with increasing unloading velocity at a given vibrational amplitude (Fig. 2.26). This is expected since the steady state pre-contact residual deformation

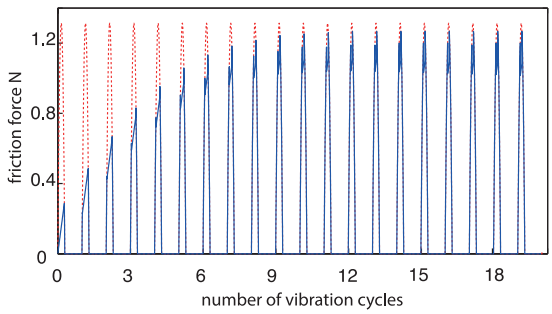

FIGURE 2.25: The frictional force as a function of the number of vibrational cycles with a lateral skin recovery speed of 1.5 mm/s (continuous blue line) as calculated by the spring-slider model with normal and lateral spring stiffnesses of 3.9 and 1.5 MN/m, a vibrational amplitude of 5 µm, a normal load of 0.5 N, static friction coefficient of μ_0 = 0.5 and plate sliding velocity of 20 mm/s. The dotted red line shows the results for an infinitely fast recovery speed as calculated from $\mu_0 F_{reac}$.

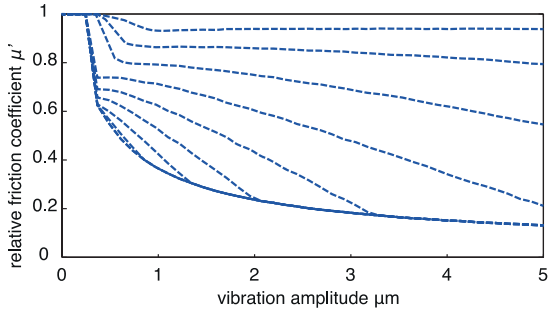

FIGURE 2.26: The steady state relative coefficient of friction as a function of the vibrational amplitude calculated using the spring-slider model with the input parameters equal to those in Fig. 13 except that lateral recovery velocity of the skin was varied between 1.5 (top line) to 15 mm/s (lower line).

will also decrease with increasing unloading velocity. Thus, although gross viscoelastic damping of the finger pad is a necessary condition to achieve a friction modulation, lateral damping of the external layers of the skin causes a reduced modulation. The results of this analysis are in agreement with the inverse analysis performed on the FE model which confirmed that the external layer of the skin can be considered elastic in the ultrasonic regime.

2.8 Experimental Assessment

In this section, a set of experimental assessment of the proposed mechanical model for both *in vivo* and probe tribological data are reported. This work was carried on in collaboration with Thomas Sednaoui and Brygida Dzidek, PhD student in the framework of the Prototouch project.

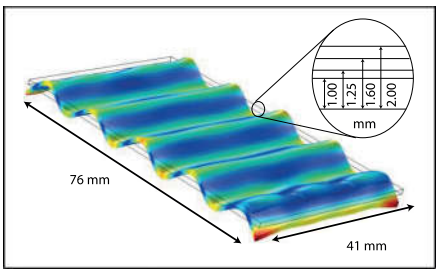

FIGURE 2.27: Finite element representation of the vibrational mode of the aluminum plates developed for the frequency dependent study.

2.8.1 Measurement of the Velocity and Frequency Dependence

A tribometer (TRB, CSI, Switzerland) was used to quantify the influence of the exploration velocity and vibrational frequency of the plate on the friction reduction. The plate employed for the pressure experiments was reused to measure the influence of the scanning velocity of the probe on the reduction in friction. Four different aluminium ultrasonically vibrating plates were designed by FE modelling (Salome-Mecha) to study the influence of the vibrational frequency on the reduction in friction. The plates have identical surfaces and employ the same vibrational mode but the thickness was varied in order to obtain different vibrational frequencies. Their dimensions are 41 x 76 mm with thicknesses of 1, 1.25, 1.6 and 2 mm and resonant frequencies of 36.6, 43.3, 53.7 and 66.1 kHz respectively. All the plates exhibited the same vibrational mode with a spatial wavelength of 16 mm (Fig. 2.27). A similar closed-loop control of the vibrational amplitude was implemented for all the plates to maintain stability of the amplitude under the range of measurement conditions investigated. A similar rough plastic film was attached to the plates in order to obtain a uniform surface roughness of 1.23 ± 0.03 µm Ra.

2.8.2 Real Finger Pad Friction Measurements

2.8.2.1 Passive Tribometer

Previous studies of the squeeze film effect have reported measurements of the friction between a plate and a finger pad in active touch [55]. In this configuration, the finger is voluntarily exploring the surface and thus the subject is responsible for the speed of exploration and the normal force adjustment. In order to precisely control these two

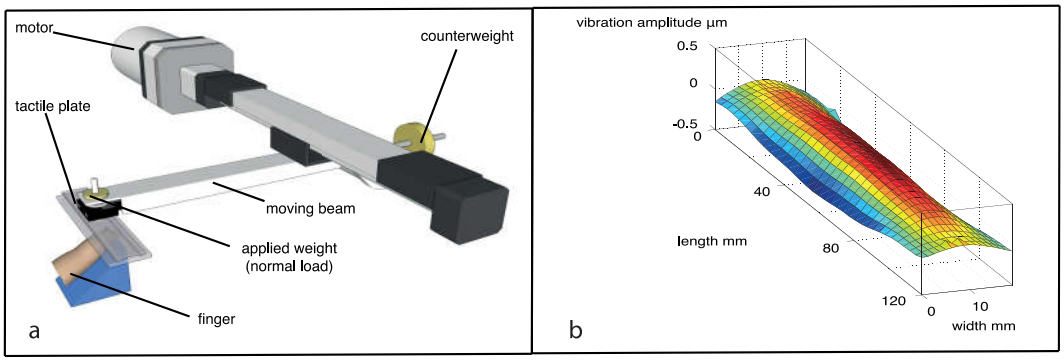

FIGURE 2.28: (a) Schematic diagram of the reciprocating passive tribometer, (b) cartography of the vibrating steel plate as measured by an interferometric vibrometer.

parameters, a passive touch based tribometer was adapted (Longshore System Engineering, Cornwall, UK) (Fig. 2.28a). A beam with a bearing acting as a pivot to allow free rotation is displaced laterally with a reciprocating velocity controlled by a DC motor. There is a 2-axis strain gage sensor at one end of the beam below which the vibrating plate is attached. A counterweight on a screw thread at the other end of the beam allows it to be balanced. Weights are placed on the sensor assembly to vary the normal force that is applied to the finger. An arm support provides user comfort and ergonomic control with secure wrist and hand support to allow precise finger pad positioning. A wedge-support is provided to position the finger at an angle of 30° to the plate. The tangential and normal forces are measured using two strain gauge ADC interfaces with 16-bit precision and a sampling frequency of 100 kHz implemented on a NI ADC system. The force measurements, amplitude data and position of the beam were then stored on a Windows computer using Labview and re-sampled using Matlab. Windowing was done to extract only the forces while the finger pad was located in the central region of the moving plate; data from the borders of the plates were removed to reduce the noise in the dynamic friction imposed by the saw tooth displacement profile of the tribometer beam.

2.8.2.2 Vibrating Plate

The vibrating device is a steel plate with dimensions 120 x 22 x 2 mm, equipped with 15 piezoceramic actuators used as a driver and one as a sensor; the resonant frequency is 25.1 kHz with a stable maximum in the centre. The relationship between the voltage applied to the ceramic transducer and the generated vibrational amplitude for the mode

TABLE 2.5: Summary of the participants for the *in vivo* friction measurements

Participant	p1	p2	p3	p4	p5	p6
Age	27	26	32	35	30	27
Gender	F	F	F	F	M	M

selected was calibrated by using an interferometric vibrometer (OV-5000, Polytech, Germany) (Fig. 2.28b). A closed-loop system was implemented to control the vibrational amplitude of the plate to ensure the stability of the acquired data for applied normal forces of $\leq$ 2 N and vibrational amplitudes of $\leq$ 2.5 µm. The mean roughness of the steel plate is 0.36 $\pm$ 0.03 µm Ra as characterised using a Surface Profiler (MicroXAM 100HR, KLA-Tencor, Belgium).

2.8.3 Experimental Protocol

Table 2.5 summarises the details of the participants for the *in vivo* friction measurements; all participants gave their informed consent. It should be noted that the measurements can be quite long and exhausting for a participant since completing a full 3D matrix for a range of velocities and loads takes a minimum of 5 h. To prevent any change in the finger pad characteristics and possible artefacts due to movements of the finger, the participants were only subjected to one parameter (velocity or normal force) for a given session. The finger to be studied was initially cleaned with a commercial soap and water and, after thorough rinsing with water, it was allowed to equilibrate for at least 10 min under ambient conditions of 16 °C and a relative humidity of 50%. The arm of the participant was positioned in the holder for the most comfortable position. The right hand index finger pad was supported by the wedge support at 30° to the horizontal and additionally adjusted by using a tape on the second phalange to prevent rotation of the finger under the high loads. Each session was initiated by automatic load calibration after which standard calibrated weights were placed on the sensor/ultrasonic plate assembly for applying the required normal force. The vibrational amplitude was increased by a staircase function in steps of 0.1 - 0.2 µm for every three full sliding cycles.

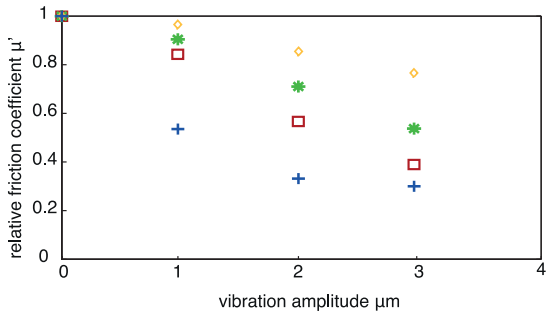

FIGURE 2.29: The relative coefficient of friction for the probe sliding on an ultrasonic vibrating plate for an applied normal force of 1.0 N and an exploration velocity of 30 mm/s, and for vibrational frequencies of 36.6 (yellow diamonds), 43.3 (green stars) 53.7 (red squares) and 66.1 kHz (blue crosses).

2.8.4 Experimental Results

2.8.4.1 Results for Articficial Fingertips

Frictional Data as a Function of the Vibrational Frequency, Velocity and Normal Force Plots of the relative coefficient of friction as a function of the vibrational amplitude for the different resonant frequencies of the aluminium plates are shown in Fig. 2.29. The data exhibit the expected reduction in μ' with increasing amplitude. For a given amplitude, the value of μ' decreases systematically with increasing frequency and, at an amplitude of 3 µm, the value at a frequency of 66.1 kHz is $\sim$ 40% of that at 36.6 kHz. Fig. 2.30 shows plots of the relative coefficient of friction as a function of the vibrational amplitude for exploration velocities in the range 25 - 100 mm/s and an applied normal force of 0.5 N. Again the data exhibit the expected reduction in μ' with increasing amplitude. For a given vibrational amplitude, the value of μ' decrease systematically with decreasing exploration velocity and, at an amplitude of 3 µm, the reduction of the friction at a velocity of 25 mm/s is a factor of $\sim$ 4 greater than that at 100 mm/s. Fig. 2.31 shows that the relative coefficient of friction is independent of the applied normal force for the three values examined.

2.8.5 *In Vivo* Friction Results

2.8.5.1 Frictional Load Index

Fig. 2.32 shows a plot of the frictional force for a finger pad (p1) as a function of the applied normal force at an exploration velocity of 40 mm/s measured using the

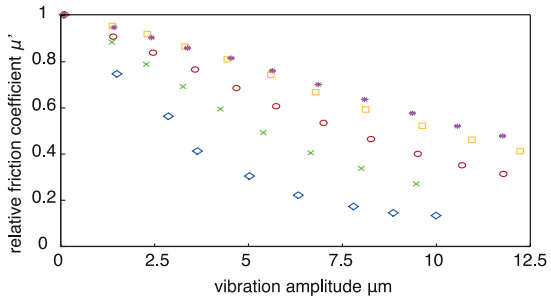

FIGURE 2.30: The relative coefficient of friction for the probe sliding on an ultrasonic vibrating plate as a function of the vibrational amplitude for an applied normal force of 0.5 N and vibrational frequency of 25.1 kHz. The exploration velocities are 10 (blue diamonds), 25 (green crosses), 50 (red circles), 75 (yellow squares) and 100 mm/s (purple stars).

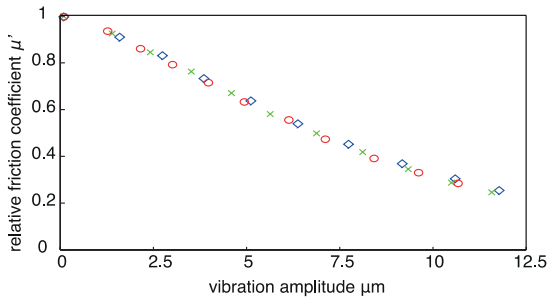

FIGURE 2.31: The relative coefficient of friction for the probe sliding on an ultrasonic vibrating plate as a function of the vibrational amplitude for applied normal forces of 0.25 N (blue diamonds), 0.5N (green crosses), and 0.75 N (red circles), with an exploration velocity of 25 mm/s, and vibrational frequency of 25.1 kHz.

passive tribometer with the plate not being vibrated. Data for the 1st cycle are shown in Fig. 2.32(a) and for the 10th cycle in Fig. 2.32(b). These preliminary results confirm that the friction coefficient between the non vibrated ultrasonic plate and the finger is independent on the normal load.

2.8.5.2 Influence of the Vibration

Fig. 2.33 shows data for the coefficient of friction as a function of the vibrational amplitude at a frequency of 25.1 kHz and an exploration velocity of 17 mm/s for three different participants and a similar applied normal force of $\sim$ 0.1 N. It exemplifies the wide variation in the absolute coefficients of friction for different participants.

Similar data measured in the current work are presented in Fig. 2.34(a) for one participant (p5) with an applied normal force of 0.5 N, and a vibrational frequency of 25.1 kHz for three exploration velocities of 20, 40 and 80 mm/s. The reduction in the friction

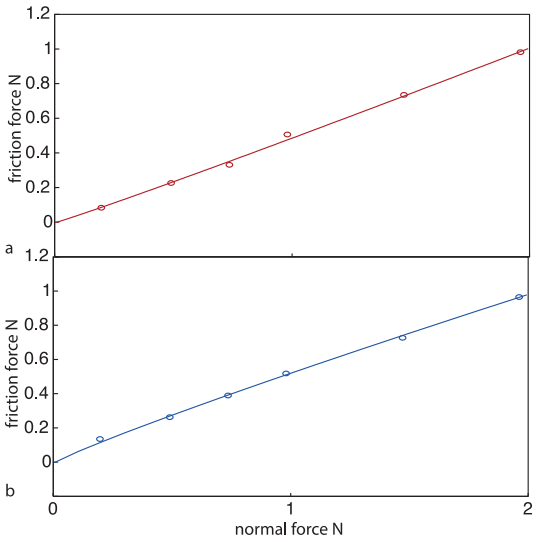

FIGURE 2.32: The frictional force as a function of the applied normal force for a finger pad with an exploration velocity of 40 mm/s for (a) for the 1st exploration cycle and (b) the 10th cycle. The lines are the best fit to the power law expression Eq. 1.8.

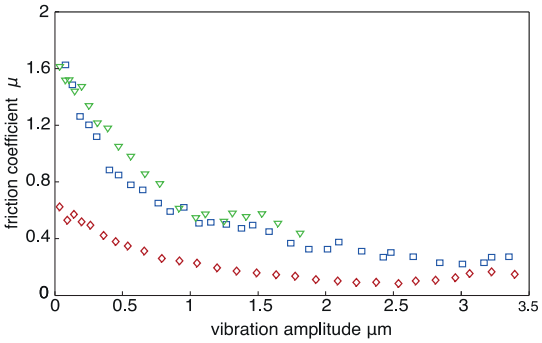

FIGURE 2.33: Coefficient of friction as a function of vibrational amplitude at a frequency of 25.1 kHz and an exploration velocity of 17 mm/s for three different participants with applied normal forces of 0.087 (red circles), 0.093 (blue squares) and 0.099 N (green diamonds).

is systematically greater with decreasing exploration velocity. Comparable trends for the dependency of the vibrational amplitude are evident in Fig. 2.34(b) from a normalization of the data shown in Fig 2.33, but this was for a single exploration velocity of 17 mm/s. An important point about Fig. 2.34(b) is that normalisation results in an approximate superposition of the data.

The mean values of the relative coefficient of friction as a function of the vibrational amplitude for all participants are presented in Fig. 2.35. There is not a systematic dependence on the applied normal force for the range examined.

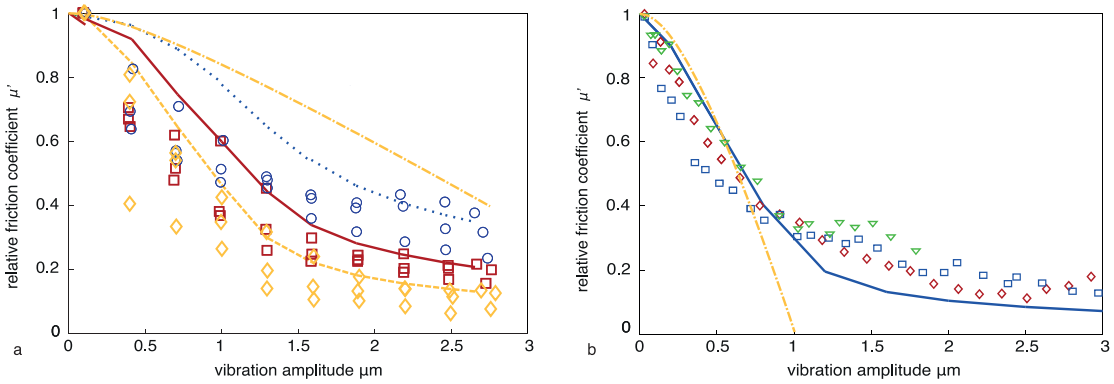

FIGURE 2.34: (a) The relative coefficient of friction for p5 as a function of the vibrational amplitude at a frequency of 25.1 kHz, an applied normal force of 0.5 N and the following exploration velocities: 20 (yellow diamonds - dashed line), 40 (red squares - continuous line) and 80 (blue circles - dotted line) mm/s, and (b) literature data for applied normal forces of 0.087 (red diamonds), 0.093 (blue squares - continuous line) and 0.10 N (green triangles); the exploration velocity is 17 mm/s and the vibration frequency is 25.1 kHz. The yellow chain line was calculated using the squeeze film model [60]. The other lines were calculated using the FE model with the input parameters for the humid case.

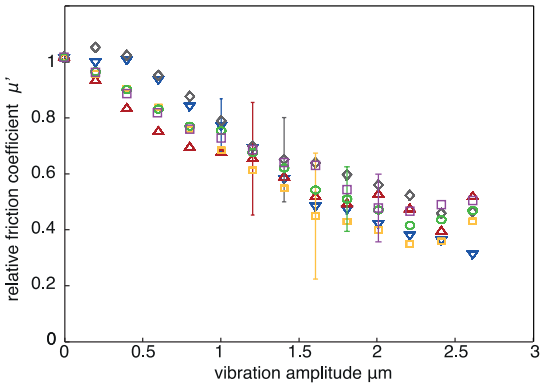

FIGURE 2.35: Mean relative coefficient of friction for all participants (p1 - p6) as a function of the vibrational amplitude for the following applied normal forces: 0.2 (blue down triangle), 0.5 (red up triangle), 0.75 (grey diamonds), 1.0 (yellow squares, 1.5 (green circles), and 2 N (purple left triangles). The error bars indicate the mean standard deviation between the participants.

2.9 Discussion

On the basis of FE modelling, it was argued that the reduction in friction for ultrasonic haptic displays could be ascribed to a ratchet mechanism in which engagement induces lateral deformation of the fingerprint ridges until the frictional mobilisation criterion is satisfied. Thus during any vibration cycle, the friction is either (i) zero when there is a loss of contact or (ii) less than the slip value. The model was evaluated in the current work by calculating the influence of the vibrational amplitude for a range of exploration velocities and normal forces for *in vivo* and probe frictional data.

2.9.1 Squeeze Film Effect

The calculated values of μ' with the FE model are compared with the experimental data in Fig. 2.34 and the trends in the numerical values are reasonably similar to those measured despite the model being relatively simple. The values of μ' calculated using the squeeze film model [60] are also shown in this figure. The experimental data fit less closely and the model cannot account for the friction being a function of the exploration velocity. Thus, these findings are consistent with the observation that the friction is not influenced by a reduced ambient pressure (Fig. 2.12), which would be expected if squeeze film levitation was significant.

2.9.2 Mechanical Model Validation

2.9.2.1 Velocity and Frequency Influence

The self-consistency of the FE results and the dimensionless group derived from the spring-slider model was demonstrated by showing that this group could be used to satisfactorily superimpose the numerical results applied to a finger pad. However, at vibrational amplitudes smaller than ~ 1 µm the intermittent contact may be insufficiently developed for the friction not to be influenced by the Young's modulus of the *stratum corneum* and the applied normal force, depending on the vibrational frequency. This is the case for the reduced variables plot of the *in vivo* data given in Fig. 2.36. There is reasonable data superposition for amplitudes of > 1 µm and these data were fitted to the exponential function Eq. 2.11 with $\Psi^* = 4.69 \pm 0.32$ as shown in the figure. This value of Ψ^* is greater than that (2.38 ± 0.21) for the FE analysis of a finger pad but it reflects the greater scatter of *in vivo* measurements of ultrasonic displays and, in particular, the small range of the dimensionless group that could be fitted. In comparison, using the probe, it is possible to achieve data superposition for a range of vibrational frequencies, and exploration velocities as well as vibrational amplitudes (Fig. 2.37) since the minimum vibrational amplitude is 1 µm. In this case, the value of is 0.70 ± 0.04.

It is of interest that the boundary condition assumption of $\mu = 0$ when $\Psi = 0$ in the derivation of Eq. 2.11 seems to satisfy the experimental data rather than a finite value of μ at $\Psi = 0$. This suggests that the performance of ultrasonic displays could be

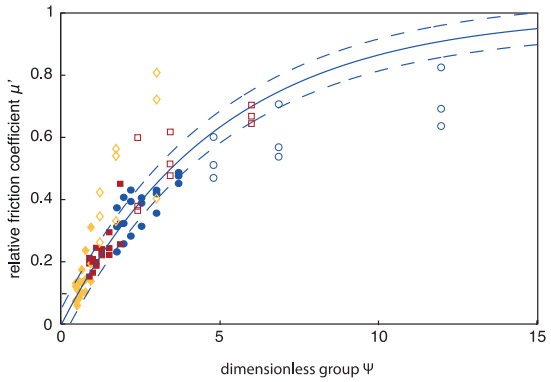

FIGURE 2.36: Relative friction for participant p5 with an exploration velocity of 20 (yellow diamonds), 40 (red squares) and 80 mm/s (blue circles) as a function of the dimensionless group; the data are taken from Fig. 11(a). The full line is the best fits of the filled points to Eq. (2) and the value of Ψ^* is 4.69 ± 0.32; the unfilled points correspond to $w < 1\,\mu m$ and were not included in the fit. The dashed lines show the RMSE variation of the fit.

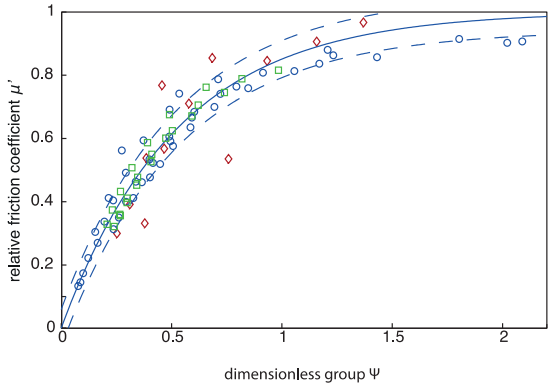

FIGURE 2.37: The relative coefficient of friction as a function of the dimensionless group for the probe sliding on an ultrasonic vibrating plate with a range of vibrational frequencies (red diamonds), exploration velocities (blue circles) and applied normal forces (green squares) the data are taken from Figs 6, 7 and 8 respectively. The full lines are the best fits to Eq. (2) and the value of Ψ^* is 0.70 ± 0.04; the dashed lines correspond to the RMSE variation.

improved further by increasing the vibrational frequency to values that are greater than those examined in the current work, due to the dependence of Ψ with this variable.

2.9.2.2 Influence of the Applied Normal Force

Fig. 2.31 and the fit reported in Fig. 2.37 show that for the artificial fingertip there is no influence on μ' of the applied normal force, and consequently for the value of Ψ^*. However, as discussed previously, *in vivo* data are considerably more scattered and less reproducible as exemplified in Fig. 2.38 for two of the participants and a range of applied normal forces. A possible contributory factor is that the finger pads exhibited a

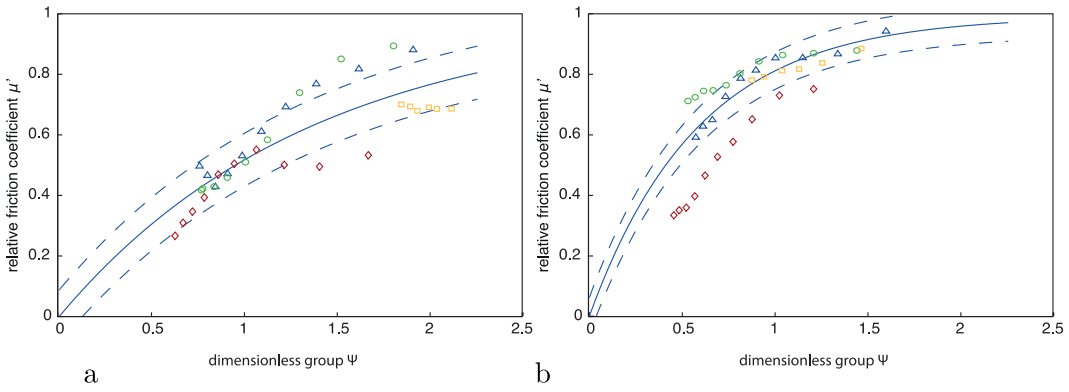

FIGURE 2.38: The relative coefficient of friction as a function of the dimensionless group measured for two participants with an exploration velocity of 40 mm/s and a range of normal forces. (a) p2: 0.75 (red diamonds), 1 (blue triangle), 1.5 (green circles) and 2 N (yellow squares). (b) p3: 0.2 (red diamonds), 0.75 (blue triangle), 1 (green circle), and 2 N (yellow squares). The full lines are the best fits to Eq. 2.11 and values of Ψ^* equal to 1.89 ± 0.18 and 0.78 ± 0.046 respectively; the dashed lines correspond to the standard deviation of the fit to the exponential function Eq. 2.11.

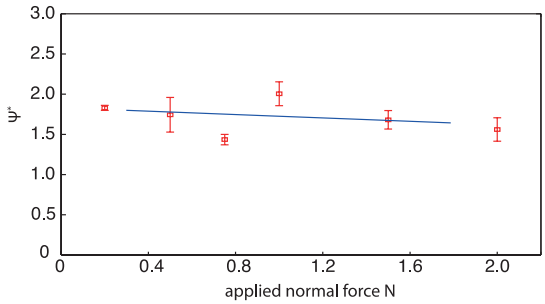

FIGURE 2.39: The characteristic value of the dimensionless group as a function of the applied normal force calculated by fitting Eq. 2.11 to the data in Fig. 2.35. The line is the best linear fit to the data.

wide range of Young's moduli so that not all the data corresponded to the intermittent contact being sufficiently well developed. In such cases, the dimensionless group approach becomes inapplicable at smaller vibrational amplitudes. However, by taking mean values of the data for all participants (Fig. 2.35) and fitting to the exponential function, mean values of Ψ^* as a function of the applied normal force were obtained (Fig. 2.39). The figure shows the best fit to a linear relationship with a slope of -0.094 with 95% confidence bounds of -0.49 and 0.30 and an intercept of 1.80 with 95% confidence bounds of 1.34 and 2.27. Thus it may be concluded from these data that Ψ^* is not a strong function of the applied normal force and that the mean value of Ψ^* is reasonably consistent with that of the numerical data for which $\Psi^* = 2.38 \pm 0.21$.

Previously, the FE model employed a Coulombic boundary condition:

$$F_l = \mu_0 F_{reac} \tag{2.34}$$

where F_l is the lateral force and F_{reac} is the normal reaction force of the vibrating plate. However, a finger pad exhibits non-Coulombic friction against smooth surfaces [40, 78]:

$$F_l = k_f F_{reac}^n \tag{2.35}$$

where k_f is the friction factor and n is the frictional load index with $2/3 \leq n \leq 1$. Consequently, Eq. 2.30 could be generalised as follows:

$$\Psi = \frac{U F_{reac}^n}{k_f w f \mu_0 (1+\nu)} \tag{2.36}$$

where k_{f0} is the intrinsic value of k_f. The data in Fig. 2.32 were fitted to Eq. 2.35 with $F_{reac} = F_n$ since the plate was in a static state, with $k_f = 0.49 \pm 0.02$ and $n = 1.05 \pm 0.08$ for the 1st cycle and $k_f = 0.52 \pm 0.01$ and $n = 0.91 \pm 0.05$ for the 10th cycle. The dependence of the friction on the applied normal force may be understood because the friction of human skin is described by the adhesion mechanism [40].

In principle, the dimensionless group should be modified according to Eq. 2.36 but the current data strongly suggest that the *in vivo* and the artificial fingertip friction modulation is not a function of the applied normal force. Thus Eq. (1) is the better descriptor of the phenomenon for both *in vivo* and probe measurements. This is probably a consequence of the friction modulation being primarily governed by the deformation of the fingerprint ridges and the extent to which there is a loss in contact rather than being dominated by slip for which the adhesion mechanism would apply.

Finally, it is of interest that the boundary condition assumption of $\mu = 0$ when $\Psi = 0$ in the derivation of Eq. 2.33 seems to satisfy the experimental data rather than a finite value of μ at $\Psi = 0$. This suggests that the performance of ultrasonic displays could be improved further by increasing the vibrational frequency to values that are greater than those examined in this section. The benefits of a greated vibrational frequency will be applied in the E-ViTa device depiced in the last section.

2.9.3 Contribution of Other Phenomena

Another interest of the developed mechanical model is to allow the analysis of different mechanisms proposed in the literature explaining the friction reduction provided by ultrasonic devices: the de-occlusion mechanism and stochastic adhesion theory De-occlusion may result in a hardening of the skin after each loss of contact. However, the evidence from the current work suggests that any such small change in the Young's modulus would not have a major effect on the friction. It is also consistent with the findings that ultrasonic vibration reduces the friction of solids having a wide range of Young's moduli, for example, from tens of kPa [79] to hundreds of GPa [80]. The stochastic adhesion mechanism could contribute to the reduction in the friction. It relies on the regeneration of the population molecular bonds at the interface following a loss in contact and requires that the repinning time of the bonds is short compared with the smallest contact duration; more details about the stochastic adhesion theory applied to the finger pad can be found in [40]. However, the ubiquitous nature of the influence of ultrasonics on friction modulation would suggest that the contribution would be second order if it were significant.

2.10 Conclusion

In this chapter, a finite element model of the fingerprint ridges was developed and calibrated through an inverse analysis of experimental measurements. With this model the parametric dependence of the reduction of the friction generated by the mechanical interplay between the vibrating plate and the finger was highlighted. The main results of the modelling suggest that: (i) intermittent contact is the dominant mechanism for the friction modulation associated with ultrasonic displays, (ii) the reduced friction cannot attain a zero value, (iii) the phenomenon is systematically dependent on the vibrational amplitude and, on the ultrasonic frequency, on the intrinsic friction coefficient, and on the exploration velocity, and (iv) it is independent on the applied normal force and the on the mechanical properties of the skin, provided that the intermittent contact is sufficiently well developed. An analytical model was then developed to further develop the parametric analysis and introduce a dimensionless group dependent on the governing parameters to provide design guidelines and allow data superposition.

The current experimental data are consistent with the FE model developed and also the data superposition scheme derived in that work. Thus, the proposed ratchet mechanism is a satisfactory explanation for the friction modulation of ultrasonic displays and squeeze film levitation does not make a significant contribution. In particular, the friction modulation depends on the exploration velocity and is independent of the applied normal force and the ambient air pressure, which is contrary to the predicted behaviour based on squeeze film levitation. Data reduction using an exponential function of a dimensionless group shows a reasonable description of experimental data, provided that the intermittent contact is sufficiently well developed. This requires that the vibrational amplitude must be > 1 µm for the range of frequencies examined here. Another important design rule confirmed by this work is the enhanced performance of ultrasonic tactile devices employed at vibrational frequencies greater than those used in the current work. Finally, the potential contribution of the stochastic adhesion mechanism, de-occlusion mechanism, and non-Coulomb friction was analyzed.

In addition, a reliable theoretical model of the friction modulation for ultrasonic devices will have implications for control, energy consumption and performance optimisation.

In the next chapter, the second main technique, namely electrovibration, available to modify the user perception of a surface will be analyzed, and amelioration of the accepted model proposed.

Related pubblicatons to this chapter are:

- E. Vezzoli, B. Maria Dzidek, T. Sednaoui, F. Giraud, M. Adams, and B. Lemaire-Semail. "Role of Fingerprint Mechanics and Non-Coulombic Friction in Ultrasonic Devices." IEEE - World Haptics Conference 2015, Chicago.
- T. Sednaoui, E. Vezzoli, B. Maria Dzidek, B. Lemaire-Semail, C. Chiappaz, and M. Adams. "Experimental Evaluation of Friction Reduction in Ultrasonic Devices." IEEE - World Haptics Conference 2015, Chicago.
- E. Vezzoli, Z. Vidrih, V. Giamundo, B. Lemaire-Semail, F. Giraud, T. Rodic, D. Peric, and M. Adams. "Friction Reduction Through Ultrasonic Vibration Part 1: Modelling Intermittent Contact." Submitted to IEEE - Transaction on Haptics.
- T. Sednaoui, E. Vezzoli, B. Maria Dzidek, B. Lemaire-Semail, C. Chiappaz, and M. Adams. "Friction Reduction Through Ultrasonic Vibration Part 2: Experimental Evaluation of Intermittent Contact and Squeeze Film Levitation." Submitted to IEEE - Transaction on Haptics.

Chapter 3

Friction Control by Electrostatic Attraction

3.1 Introduction

In this chapter, the second main technique available to control the friction between the finger and a surface, called electrovibration, will be introduced, and its modeling analyzed. The electrovibration relies on the time modulation of the normal force imposed by a finger sliding on a surface by electrostatic attraction. The effect is known since the mid fifties [81], but the interest has raised only recently, due to the rising importance of touch based devices. Firstly, spatial division of electrode was developed to provide precise and complex stimulus pattern of conductive pads, but this solution suffered from its complexity and turned out difficult to apply [82]. Recently, electrovibration took advantage of technological improvements of fingertip's position sensor based on optical or resistive solutions. The possibility to track precisely the position of the finger leads to fine gratings simulation thanks to spatial-stimulus relation, with a similar approach to the one implemented for ultrasonic vibration based devices. With spatio-temporal transformation, the stimulator itself becomes easier to manufacture and it becomes possible to produce tactile feedback on transparent flat or curved surfaces [83] or merge it with another tactile stimulation technique [84]. A method to provide a stable sensation along the different impedance conditions generated by the environment has been developed [85].

If the efficiency of the process to provide successful tactile feedback is clear, the physical modeling of the phenomenon involving the finger is not yet satisfactory. The lacking of a reliable model of the stimulus may prevent the developing of refined stimulation pattern and induced sensation. The aim of this chapter is to investigate the modeling proposed in the literature and to suggest a modification of the current model to take into account the influence of the finger skin displacement and geometry, the air layer included between the surfaces, and the frequency dependence of the biological parameters involved in the phenomenon. Moreover, the scatter of the experimental measurements will be explained in relation with the variability of the geometric properties of the biological tissues. The chapter is organized as follows: firstly the proposed literature models of the electrostatic force are introduced, then the derivation of the electrostatic force between a double dielectric capacitor is proposed and an experimental setup able to check the validity of the classical model is presented. Following, the influence of the finger geometry and mechanics as well as the air layer are introduced. This work has been carried out in collaboration with researchers from Swansea university (UK), in the framework of the Prototouch Project. Last, a discussion of the frequency dependence of the skin material parameters is proposed, followed by an explanation of the absence of electrostatic attraction in the static regime due to the charge dynamics. Following, a digression on the most effective construction parameters will take place to suggest optimization on the construction process.

3.2 Classic Expression of the Electrostatic Force

A finger immersed an electric field experiences an induced polarization. Following the Coulomb principle, there is a polarization of the finger which, by interacting with the electric field, determines an attractive force towards the polarizing electrode. The amplitude of this interaction is small, but is comparable with the amplitude of touch-sensing action [84]. The generic working principle of electrovibration is represented in Fig. 3.1, and hystorically, it has been modelled with the electrical circuit theory. This modelling will be introduced in the following section.

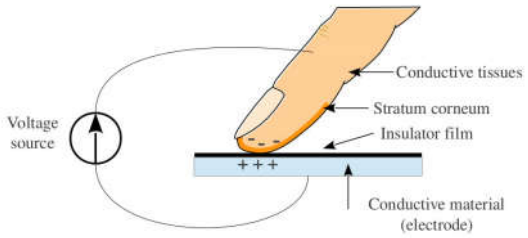

FIGURE 3.1: Working principle of electrovibration

3.2.1 Single Dielectric Capacitor:

Let us remind firstly the capacitance and the electrostatic force for a single dielectric capacitance C:

$$C = \frac{\epsilon_0 \epsilon A}{d}, \tag{3.1}$$

where ϵ_0 denotes the permittivity of vacuum, A the surface area of the plates, and ϵ and d the relative permittivity and thickness of the dielectric, respectively.

The Coulomb electrostatic force F_e between the plates of a parallel plate capacitor with a single dielectric is expressed as

$$F_e = \frac{\epsilon_0 \, \epsilon \, A \, v^2}{2d^2}, \tag{3.2}$$

where v denotes the potential difference between the plates, i.e. the voltage applied.

3.2.2 Multi Dielectric Capacitor: modeling from bibliography

Due to the discrepancies and discussions emerging in the literature, namely between [86, 87] and [82], both of the models developed in the cited works are hereby introduced and analysed. The classic representation of the electrical circuit associated with the electrovibration stimulation is presented in Fig. 3.2. It consists on the equivalent circuit made by the capacitor of the *stratum corneum* and the capacitor of the insulator connected in series.

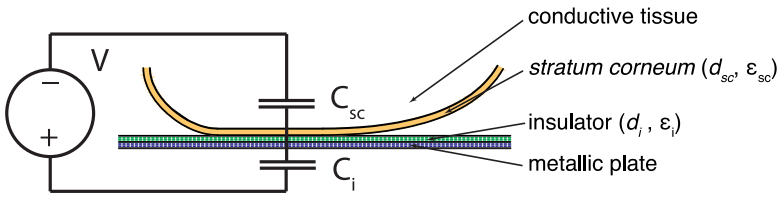

FIGURE 3.2: Classic electrical circuit scheme for the electrovibration principle, with C_{sc} and C_i the capacitance of the *stratum corneum* and of the insulator.

3.2.2.1 Strong and Troxel Model

Strong and Troxel [87] proposed the first mathematical model for electrostatic attraction between the finger pad and the charged surface based on experimental results as:

$$F_e = \frac{\epsilon_0 \, A \, v^2}{2\left(\frac{d_{sc}}{\epsilon_{sc}} + \frac{d_i}{\epsilon_i}\right)^2} \tag{3.3}$$

where d_{sc} and d_i are respectively the thicknesses of the *stratum corneum* and the insulator, and ϵ_{sc} and ϵ_i are the dielectric constants of the *stratum corneum* and the insulator.

3.2.2.2 Kaczmarek et al model

Kaczmarek et al. [82], who were investigating the effect of voltage polarity in electrovibration tactile displays, questioned Eq. 3.3 by claiming that, when either d_{sc} or d_i approaches zero, or when $\epsilon_{sc} = \epsilon_i = \epsilon$, the expression should equal Eq. 3.2. Instead, it differs by the factor ϵ, i.e.

$$F_e = \frac{\epsilon_0 \, \epsilon^2 \, A \, v^2}{2d^2}. \tag{3.4}$$

For this reason, in the next subsection the multi-dielectric expression is derived from its first principles.

3.2.3 Derivation of the electrostatic force for the Kaczmarek model

In this subsection, the electrostatic force between a double dielectric capacitor is derived through the electrostatic co-energy. The capacitance of a single dielectric k of thickness d_k and relative permittivity ϵ_k is deduced from Eq. 3.1 as follows

$$C_k = \frac{\epsilon_0 \epsilon_k A}{d_k}. \tag{3.5}$$

Since the inverse capacitance of a parallel-plate capacitor with multiple dielectrics in series is calculated as an inverse of the sum over the reciprocal dielectrics' capacitances, the capacitance C of the above-mentioned system (Fig. 3.1) is given by:

$$\frac{1}{C} = \sum_k \frac{1}{C_k} = \frac{1}{C_{\mathrm{sc}}} + \frac{1}{C_{\mathrm{i}}}, \tag{3.6}$$

where sc abbreviates *stratum corneum* and i insulator.
Let's define d the sum of thicknesses of the materials. Due to the relevant stiffness of the *stratum corneum* and the relatively small value of the electrostatic forces applied during electrovibration, the ratio between the thickness of the *stratum corneum* and the stiffness of the insulator can be considered constant when the electrostatic force is applied. It follows:

$$d = \sum_k d_k = d_{\mathrm{sc}} + d_{\mathrm{i}} = \alpha d + \gamma d, \tag{3.7}$$

where α and γ are constant. Rearranging Eq. 3.6 by substituting capacitances C_{sc} and C_{i} in accordance with Eq. 3.5, the capacitance C can be expressed as

$$C = \frac{\epsilon_0 A}{\frac{d_{\mathrm{sc}}}{\epsilon_{\mathrm{sc}}} + \frac{d_{\mathrm{i}}}{\epsilon_{\mathrm{i}}}} = \frac{\epsilon_0 A}{\frac{\alpha d}{\epsilon_{\mathrm{sc}}} + \frac{\gamma d}{\epsilon_{\mathrm{i}}}} = \frac{\epsilon_0 A}{(\frac{\alpha}{\epsilon_{\mathrm{sc}}} + \frac{\gamma}{\epsilon_{\mathrm{i}}})d}. \tag{3.8}$$

The electrostatic co-energy E_e of the system is given by the expression

$$E_e = \frac{1}{2} C v^2 \tag{3.9}$$

The derivation of electrostatic co-energy E_e with respect to separation distance d results into the well-known Coulomb's equation for electrostatic force F_e between charged plates,

$$F_e = -\frac{\partial E_e}{\partial d} \tag{3.10}$$

Hence, the expression for electrostatic force between the metallic plate and the conductive tissue layers comprising the finger pad reads

$$F_e = -\frac{\epsilon_0 A v^2 \frac{\partial}{\partial d}(\frac{1}{d})}{2(\frac{\alpha}{\epsilon_{\mathrm{sc}}} + \frac{\gamma}{\epsilon_{\mathrm{i}}})} = \frac{\epsilon_0 A v^2}{2(\frac{\alpha}{\epsilon_{\mathrm{sc}}} + \frac{\gamma}{\epsilon_{\mathrm{i}}})d^2} \tag{3.11}$$

or, in terms of dielectrics' thicknesses,

$$F_e = \frac{\epsilon_0 A v^2}{2(\frac{d_{\mathrm{sc}}}{\epsilon_{\mathrm{sc}}} + \frac{d_{\mathrm{i}}}{\epsilon_{\mathrm{i}}})(d_{\mathrm{sc}} + d_{\mathrm{i}})}. \tag{3.12}$$

This equation is the model proposed by Kaczmarek et al. in their work [82]. It may be noted that this expression implies a constant normal force F_e for a constant voltage v applied.

In terms of friction, the electrostatic force F_e contributes to the total friction F_t, assumed Coulombic, as:

$$F_t = \mu(F_n + F_e), \tag{3.13}$$

3.3 Bibliographic Review of Experimental Assessment of Analytical Models

In this section, the two proposed models will be compared with the experimental assessment data from the literature to check their validity.

3.3.1 Strong and Troxel modeling

Strong and Troxel [87] were the first to systematically analyze the effect of the electrovibration based on different parameters. They were able to extract the ratio $\frac{d_{sc}}{\epsilon_{sc}}$ from the perceptual threshold voltage identified, v_2 and v_3, when exploring two different electrostatic devices. These devices were designed with two different insulators thicknesses,

d_{i2} and d_{i3}, to induce a different dependence of the electrostatic force in function of the voltage. By equating the tangential forces at threshold they were able to reconstruct the ratio $\frac{d_{sc}}{\epsilon_{sc}}$ thanks to Eq. 3.3 and 3.13.

$$\frac{\epsilon_0 \, A \, {v_2}^2 \mu}{2\left(\frac{d_{i2}}{\epsilon_i} + \frac{d_{sc}}{\epsilon_{sc}}\right)^2} = \frac{\epsilon_0 \, A \, {v_3}^2 \, \mu}{2\left(\frac{d_{i3}}{\epsilon_i} + \frac{d_{sc}}{\epsilon_{sc}}\right)^2}. \tag{3.14}$$

The results of the above-mentioned experiment were reported for a single trained subject, although Strong and Troxel asserted that another subject gave similar results in terms of forces, but different effective thickness of the *stratum corneum*. It is interesting to note that, in their experiment, they did not use a tribometer, but rather relied on the psychophysical report of the user.

To go further in the analysis, we postulate $d_i = 2d_{i2} = d_{i3}$, expressing ratio from Eq. 3.14, and replace the parameters with the numerical values reported by Strong and Troxel [87],
namely $v_2 = 73\text{V}$, $v_3 = 110\text{V}$, $d_{i2} = 0.5\mu\text{m}$ and $d_{i3} = 1.0\mu\text{m}$, $\epsilon_i = 4.5$, Eq. 3.14 yields

$$\frac{d_{sc}}{\epsilon_{sc}} = \frac{d_i}{\epsilon_i} \cdot \frac{2\,v_2 - v_3}{v_3 - v_2} = 2.74\mu\text{m} \tag{3.15}$$

Considering $\epsilon_{sc} \approx 2000$ at 200Hz [88], it follows that the *stratum corneum* thickness should equal $d_{sc} = 5.48\text{mm}$, which is an unrealistic value, an order of magnitude larger than the one generally accepted, i.e. ≈ 300 µm in palmar regions [40, 89].

On the other hand, if the *stratum corneum* thickness is derived from Eq. 3.12, i.e.

$$\frac{\epsilon_0 \, A \, {v_2}^2 \mu}{2\left(\frac{d_{i2}}{\epsilon_i} + \frac{d_{sc}}{\epsilon_{sc}}\right)(d_{i2} + d_{sc})} = \frac{\epsilon_0 \, A \, {v_3}^2 \mu}{2\left(\frac{d_{i3}}{\epsilon_i} + \frac{d_{sc}}{\epsilon_{sc}}\right)(d_{i3} + d_{sc})}, \tag{3.16}$$

by making the same postulates and using the same numerical values as in Eq. 3.14, it follows that the *stratum corneum* thickness should equal 76.2 µm. This value is lower than the reported average, but plausible nonetheless.

3.3.2 Meyer et. al experimental study

Meyer et al. [90] performed a rigorous experimental parametric study in which the electrostatic force was measured as a function of voltage and frequency of the input signal.

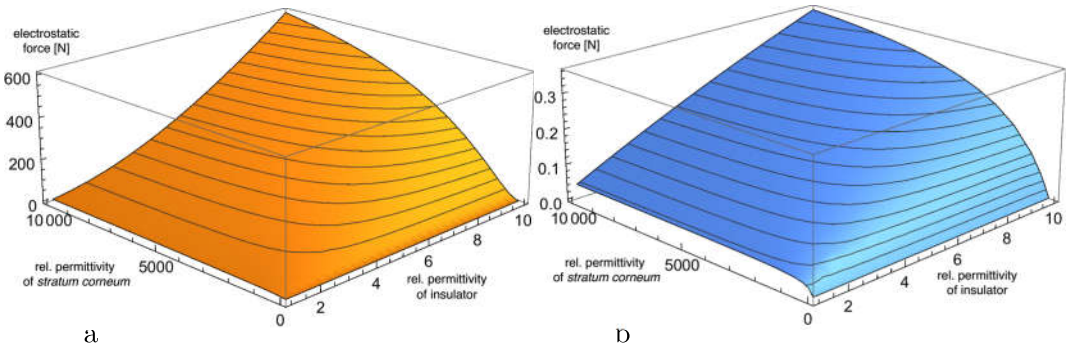

FIGURE 3.3: Computed electrostatic force F_e as a function of ϵ_{sc} and ϵ_i for a typical range [a] using Eq. 3.3, and [b] using 3.12. Contact area A is assumed 100mm^2, thicknesses of *stratum corneum* and insulator are 0.200 and 0.001mm, respectively, and voltage v is 140V. Note the scale difference on z-axis.

By considering their experimental conditions we calculated the induced electrostatic force considering both the presented models.

Friction A relationship between the lateral and the normal force acting on a sliding finger with and without electrovibration was presented for a single subject, indicating that the imposed electrostatic force was 0.25N with a standard error 0.01N.

Eq. 3.3 and 3.12 were utilised using the parameter values as presented in Table 3.2. The contact area A was assumed to be 100mm^2. The relative permittivities of *stratum corneum* and the insulator were varied; ϵ_{sc} was varied from 10^3 to 10^4, corresponding to the relevant frequency range and obtained from [88, 91], while ϵ_i varied from 1 to 10, covering a range of values for typical insulator materials.

Calculating the electrostatic force using Eq. 3.12 gives the values that are of the same order as forces measured in the above-mentioned experiment ($0.05 - 0.35$N), whereas Eq. 3.3 predicts values that are up to three orders of magnitude greater ($10 - 600$N), as depicted in Fig. 3.3.

Voltage dependence The values of the electrostatic force F_e in relationship to applied voltage v, experimentally obtained by [90], are juxtaposed with the analytical results obtained using Eq. 3.3 and 3.12. Again, the area $A = 100$mm^2 was assumed and *stratum corneum* thickness was varied from 0.1 to 0.5mm in steps of 0.1mm. Results are

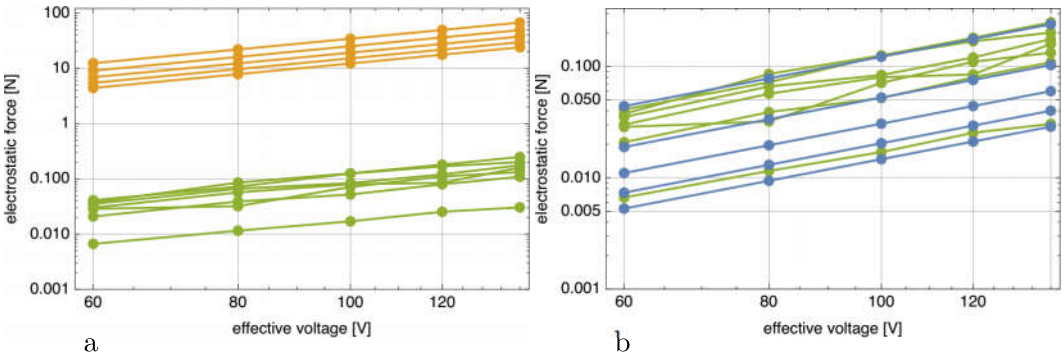

FIGURE 3.4: Computed electrostatic force F_e as a function of applied voltage v calculated [a] using Eq. 3.3 – *orange*, and [b] using Eq. 3.12 – *blue*, for varying thickness of *stratum corneum* (from 0.1 to 0.5 in steps of 0.1mm) and juxtaposed with experimental measurements reported by Meyer et al. [90] – *green*. Contact area A is assumed 100mm^2, all other parameters as in Table 3.2. Note the log plot.

presented in Fig. 3.4. Despite the large person to person variability, explained by *stratum corneum* thickness variability, it is once again obvious that Eq. 3.3 overestimates the values by orders of magnitude.

3.3.3 Conclusion

By the theoretical assessment and bibliographic comparison presented in the previous section, the model proposed by Kaczmarek et al. Eq. 3.12 was chosen as a valid starting point for the following preliminary experimental assessment.

3.4 Experimental Verification

In this section, a preliminary experimental assessment of the electrostatic force between the finger and the plate is performed.

3.4.1 Experimental Setup

As introduced in the previous section, electrovibration modifies the lateral force felt by the finger in motion by a modulation of the normal force. The modulation is due to electrostatic force and appears between the finger and the polarized surface. The developed tribometer detailed in section 2.2.2.1 will be employed for this purpose.

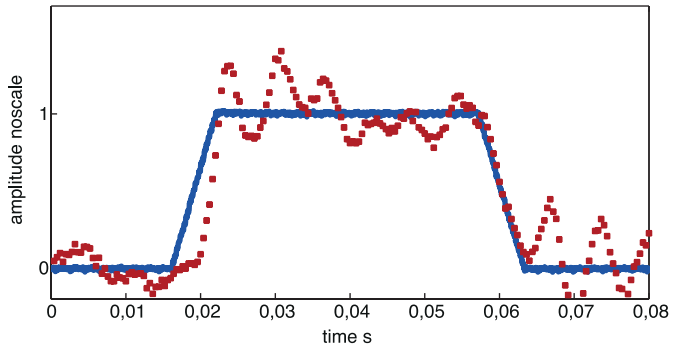

FIGURE 3.5: Normal force for the finger suspended near the polarized plate (red dots), and voltage applied (continuous line).

To provide electrostatic stimulation to the finger, an aluminum plate covered with a plastic insulator film has been used. The thickness of the plastic film was 90 µm and its dielectric relative permittivity was 3.3. A waveform generator (33120A, Agilent, USA) provides waveforms to a high voltage amplifier supplying the tactile plate. The data are acquired and elaborated in a post-process.

3.4.2 Results

Thanks to the experimental setup described in section 3.4.1, the force between a finger and the polarized plate has been measured, while there is no contact between the finger and the surface. In Fig. 3.5 is reported the normal force measured for a given voltage signal for a floating finger. It is possible to remark oscillations due to the difficulties to maintain the finger close to the plate without any contact, but the major behavior is in agreement with Eq. 3.13, that is roughly a constant force once the voltage applied is constant. Assuming that the force F_e is also given by the Eq. 3.12 once the finger touches the plate, an increase of F_e would lead to an increase of the lateral force, Eq. 3.13, creating a friction change feeling. Nevertheless, Giraud et al. [84] found an exponential reduction of the lateral force, Eq. 3.12, for an applied square voltage signal when the finger is sliding on the plate. This phenomenon is unexplained by this static model and it will be addressed in section 3.6. In the following section a more detailed modeling and refined measurements of the non contact case is reported.

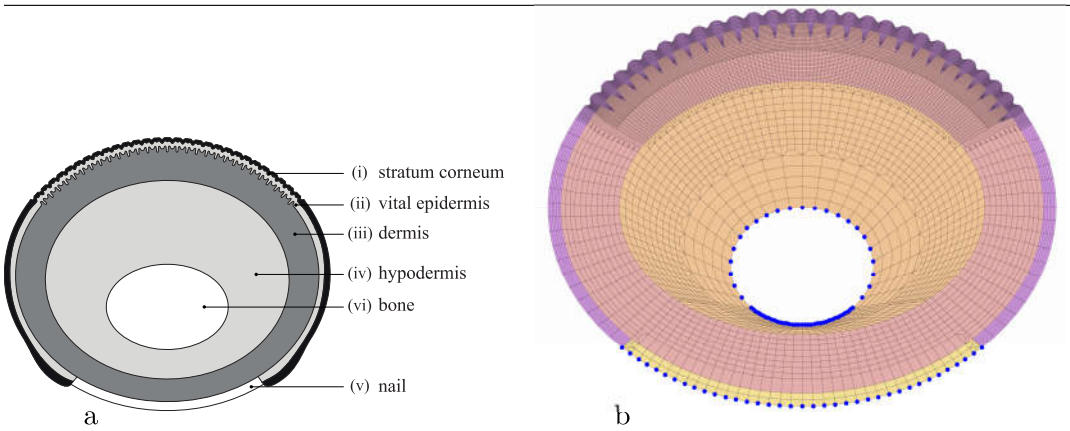

FIGURE 3.6: (a) Schematic representation of the finger pad cross-section; the model comprises six characteristic domains: (i) stratum corneum, (ii) vital epidermis, (iii) dermis, (iv) hypodermis, (v) nail and (vi) bone. (b) Representative mesh of a 2D finite element model of a fingerpad. Blue marks denote nodes with enforced boundary conditions, i.e. prevented displacements.

3.5 Air and Finger Mechanics Influence

In this section, the finite element framework developed in collaboration with the researchers of Swansea University is presented to take into account the presence of the air layer between the finger pad and the plate as well as the geometry and finger mechanics.

3.5.1 Mechanical domain

A 3D multi-scale multi-physics FE framework system for simulation of tactile scenarii has been developed in previous works in order to obtain spike time predictions of mechanoreceptors during finger pad exploration of different surfaces [92]. Current research employs a 2D version of the framework, as it has been shown in [93, 94] that 2D approach can describe the discussed problem with sufficient accuracy.

The FE model of the finger pad comprises most characteristic subdomains to assure sufficient anatomical accuracy (Fig. 3.6a). The subdomains are (i) cornified and (ii) vital layer of epidermis, i.e. *stratum corneum* and (vital) epidermis, respectively; (iii) dermis; (iv) hypodermis, i.e. the dermal white adipose tissue or subcutaneous tissue; (v) nail; and (vi) bone.

The material and geometrical properties obtained from literature [89, 94] are presented in Table 3.1 and 3.2.

	subdomain	Young's modulus [MPa]	Poisson's ratio
i	*stratum corneum*	1.000	0.30
ii	vital epidermis	0.136	0.30
iii	dermis	0.080	0.48
iv	hypodermis	0.034	0.48
v	nail	17.000	0.30

TABLE 3.1: Material parameters of fingerpad subdomains

	parameter	value	unit
a	finger width	16.68	mm
b	finger height	12.79	mm
R_{w}	fingerprint ridge width	0.50	mm
R_{h}	fingerprint ridge height	0.15	mm
d_{sc}	thickness of *stratum corneum*	0.200	mm
d_{ed}	thickness of epidermis	1.000	mm
d_{d}	thickness of dermis	2.000	mm
ϵ_0	vacuum permittivity	8.8542E-12	F/m
ϵ_{a}	relative permittivity of air	1.00	
ϵ_{i}	relative permittivity of insulator	3.35	
ϵ_{sc}	relative permittivity of *stratum corneum*	1650	
d_{i}	thickness of insulator	0.090	mm
v_{eff}	effective voltage	1414, 2000	V
μ	coefficient of friction	0.30	

TABLE 3.2: List of geometrical and electrical parameters and their values used in numerical simulations

The fingerpad can exhibit large elastic deformation, therefore the use of hyperelastic Neo-Hooke type strain energy potential constitutive law is usually employed [95, 96]. Built-in two dimensional quadrilateral plane strain F-bar finite elements [97] are utilised.

The framework is currently run on a desktop computer equipped with Intel® i7 Six Core Processor, 3.4 GHz, and 16 GB RAM, DDR3 2400 MHz. The mechanical model of a fingerpad used in this study is comprised of 23,139 nodes and 21,150 elements. *stratum corneum* consists of 2,240 nodes and 1,662 elements, epidermis of 10,998 nodes and 10,281 nodes, dermis of 8,208 nodes and 7,677 elements, hypodermis of 1,434 nodes and 1,314 elements, and nail consists of 259 nodes and 216 elements; bone is assumed to be rigid, therefore, only fixed boundary conditions are prescribed at its contour (Fig. 3.6b).

3.5.2 Electrical domain

Analytical studies of electrovibration [86, 87, 98, 99] presume that the problem can be treated as an infinite plate capacitor, as introduced in the section before, with parallel dielectrics Eq. 3.12. It is assumed that metallic plate and finger pad conductive tissue layers can be represented as conductive capacitor plates, while insulation layer placed over the metallic plate and the *stratum corneum* on fingerpad act as dielectrics, Fig. 3.1.

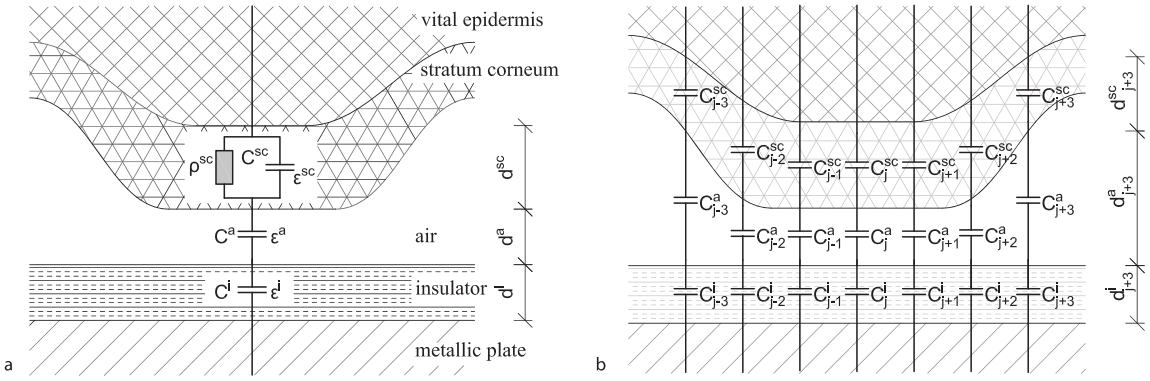

FIGURE 3.7: Graphical representation of a single fingerprint superimposed of the infinite parallel-plate capacitor model: conductive plates are formed of metallic plate and vital epidermis layers while stratum corneum, insulator and air layer behave as dielectrics.

Former studies have been persistently disregarding the insulative air layer, but since the electrostatic force between the finger pad and the tactile display can be measured even if not brought into contact, as shown in the previous section, the influence of the air layer was taken into consideration in numerical simulations. Thus, the same assumption was adopted in this section, with inclusion of possible air layer as dielectric between the finger pad and the tactile display (in the representation of a single fingerprint ridge Fig. 3.7a); Hence, the equation for electrostatic force becomes considering Eq. 3.6 becomes:

$$F_e = \frac{\epsilon_0 A v^2}{2\left(\frac{d_{\mathrm{sc}}}{\epsilon_{\mathrm{sc}}} + \frac{d_{\mathrm{a}}}{\epsilon_{\mathrm{a}}} + \frac{d_{\mathrm{i}}}{\epsilon_{\mathrm{i}}}\right)\left(d_{\mathrm{sc}} + d_{\mathrm{a}} + d_{\mathrm{i}}\right)}, \tag{3.17}$$

where $\{\epsilon_{\mathrm{a}}, d_{\mathrm{a}}\}$ denote relative permittivity and thickness of the air layer.

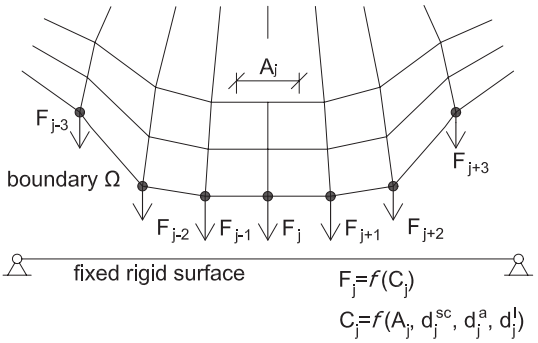

FIGURE 3.8: Schematic representation of implementation of electrostatic component within the finite contact element. For simplification purposes the electrostatic force is assumed to act only on the nodes forming the potential contact between the fingerpad and the surface.

Since the geometry of the finger pad-tactile display system varies along the dimension of a fingerprint, expression Eq. 3.17 cannot be directly used for the whole finger pad. The system has to be assumed to behave as a circuit composed of parallel-plate capacitors with varying thicknesses of dielectrics in series[1] (Fig. 3.7b). Thus, the total capacitance may be obtained by integrating the capacitances of all capacitors over the surface area A, taking into account finger pad deformations, changeability of d_{sc} and d_{a}, whereas thickness of the insulator d_{i} is presumed constant. Hence, the expression for total electrostatic force F_e, with an approximation in the discrete domain as, Fig. 3.8:

$$F_e = \sum_j F_{ej} = \sum_j \frac{\epsilon_0 v^2 A^j}{2\left(\frac{d^j_{\mathrm{sc}}}{\epsilon_{\mathrm{sc}}} + \frac{d^j_{\mathrm{a}}}{\epsilon_{\mathrm{a}}} + \frac{d_{\mathrm{i}}}{\epsilon_{\mathrm{i}}}\right)\left(d^j_{\mathrm{sc}} + d^j_{\mathrm{a}} + d_{\mathrm{i}}\right)}. \tag{3.18}$$

By this mean it is possible to take into account the finger surface geometry and structure, as well as the contribution of the air layer, in the theoretical calculation of the electrostatic force between the finger and the high voltage supplied plate. This modelling will be validated in the next section.

[1] Present study does not consider the possibility of fringing effect, which occurs when the capacitor dimensions are significantly smaller than the distance between plates although, as suggested in [100], an approximation may be implemented provided that sufficient experimental evidence is obtained. The equation for electrostatic force considers only components in vertical direction since it is assumed that horizontal components cancel out due to the vertical symmetry of the fingerprint ridges.

3.5.3 Experimental setup

The experimental setup is designed and built in order to measure the electrostatic attraction induced by a high-voltage supplied between a fingerpad and a plate. When the fingerpad and a polarising plate are in contact, it is hard to measure the electrostatic force directly since the electrostatic force is inner to the system, but its influence on the friction between the finger pad and the polarised plate can be observed. However, results can easily be inconclusive since the measurements exhibit a high level of noise; namely, the contribution of the electrostatic force to the general normal force that modulates the friction is, in principle, relatively small. Furthermore, there is also a topical question regarding tribological properties of the finger, such as moisture deposition, occlusion, stick slip, plasticisation and degradation of the skin, which should be taken into account [40, 71].

In order to avoid above-mentioned effects, a static approach was considered: the idea was to measure the electrostatic attraction between the finger and a polarized plate when they are both motionless and not in contact, i.e. when there is a thin layer of air in-between, hence confirming the role of air layer in contribution to the electrostatic force in light touch exploration.

Description The main components of the setup, as depicted in Fig. 3.9, comprise a chemical scale (BP410, Sartorius, Germany) acting as a force sensor, a tactile plate attached to the scale, a vertical bench placed over the scale and equipped with two micro-positioners (M-SDS40, Newport, USA), and a finger-holder. The tactile plate comprises a copper tape, 10×4 cm in size, which is glued to the scale and covered with a plastic insulator (0.090 mm thick, $\epsilon_{\mathrm{i}} = 3.35$ relative permittivity). The plate is connected to a high voltage amplifier (HVA2kV, Ultravolt, USA); see [84] for more details on safety issues. The finger-holder has the shape of a triangular prism, it is clamped to the horizontal bench with magnets, and positions the finger so that the angle between the longitudinal axis of the finger and the tactile plate is 30°.

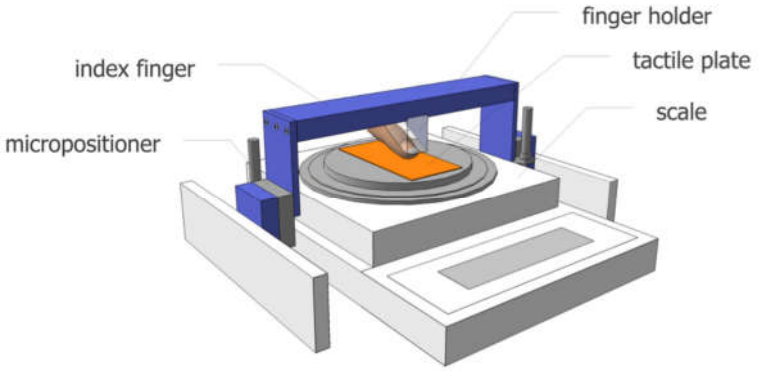

FIGURE 3.9: Experimental setup comprises a chemical scale acting as a force sensor and a bench placed over the scale. Finger-holder is attached to the bench with magnets. Vertical position of the finger is set by adjusting the micro-positioners installed on each side of the bench; tactile plate and the finger are not supposed to be in contact.

Participants Eleven volunteers were recruited for the study. They were eight males and three females and were aged 22–57 years with a median of 28 years. They all gave their informed consent and did not report any skin condition or tactile deficit.

Procedure The participants were placed in front of the setup, as illustrated in Fig. 3.9. Oral description of the setup and explanation of one's task was given to each of them. Firstly, the dimensions of each participant left index fingerpad were taken[2] (Table 3.3). The finger pad was then wiped with alcoholic solution before being attached to the finger-holder with a tape; to prevent any movements, the nail was fastened using double-sided adhesive tape. We let few minutes for the finger to adapt to the new conditions and the skin to regain its natural moisture. Participants were asked to position their left hand on a setup and to put their right hand on a metallic plate connected to the mass to close the circuit.

3.5.4 Results

3.5.4.1 Experimental verification of the numerical model

The experimental results were collected and analysed in real-time using Matlab Software [101]. Two different applied voltages and two different distances between the finger pad and the plate were considered (Table 3.4). Each recording lasted roughly 60 s. The

[2]Note: in Table 3.3 a and b denote diameter of the finger cross-section in lateral and vertical direction, respectively, and c denotes the length of the distal phalanx.

	gender	age	a [mm]	b [mm]	c [mm]	HDHV [mN]	LDHV [mN]	LDLV [mN]
i	m	33	19.18	13.09	26.19	2.50	1.55	4.00
ii	f	28	14.04	11.16	25.67	1.70	1.37	2.73
iii	m	26	17.65	12.41	24.25	1.98	1.67	3.41
iv	m	28	17.89	14.94	26.50	1.85	1.21	2.49
v	m	22	16.45	11.66	27.02	0.91	0.54	1.54
vi	f	23	16.25	11.40	25.26	1.47	0.75	2.02
vii	m	25	16.89	12.53	24.18	1.11	0.86	1.86
viii	m	32	16.78	13.20	28.52	2.57	1.45	3.92
ix	m	57	18.20	15.00	28.40	2.31	1.86	4.17
x	f	55	14.69	12.80	25.62	1.40	0.81	1.85
xi	m	26	15.46	12.49	24.99	2.06	2.42	4.42

TABLE 3.3: Experimental measurements. a, b and c are, respectively, the width, height and length of the finger pad.

	label	distance d_a [mm]	voltage U [V]
i	HDHV	0.50	2000
ii	LDHV	0.25	2000
iii	LDLV	0.25	1414

TABLE 3.4: Experimental test set

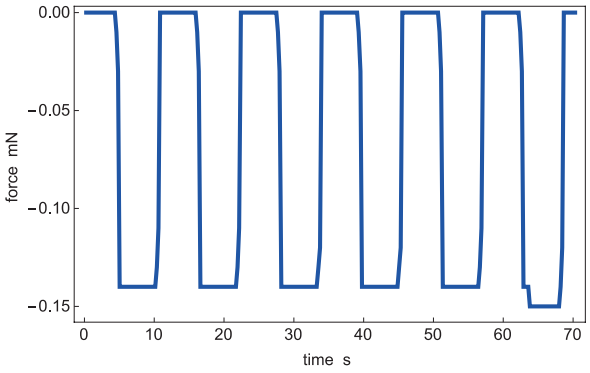

FIGURE 3.10: The graph plots time evolution of the recorded measurement of the electrostatic force for a square variation of applied voltage of 2000 V; the distance between the finger pad and the plate is set to 0.25 mm (LDHV).

voltage was applied in terms of step-function with on-and-off period of 5 s. Typical behaviour of the recorded force is depicted in Fig. 3.10. The measured forces in considered scenario are shown in Fig. 3.11 (vertical orange bar).

Similar scenarii were considered in numerical simulations using a *best estimate model*[3]: (i) the applied voltage was kept constant at 2000 V and the finger was moved from 1.00 mm towards the plate until the contact was detected; (ii) the fingerpad distance was kept constant at 0.25 mm and the applied voltage was varied from 0 to 2500 V (Fig.

[3]Mean values for the parameters used in best estimate model were obtained from experimental measurements and from the literature, see Table 3.1, 3.2, 3.3, 3.5.

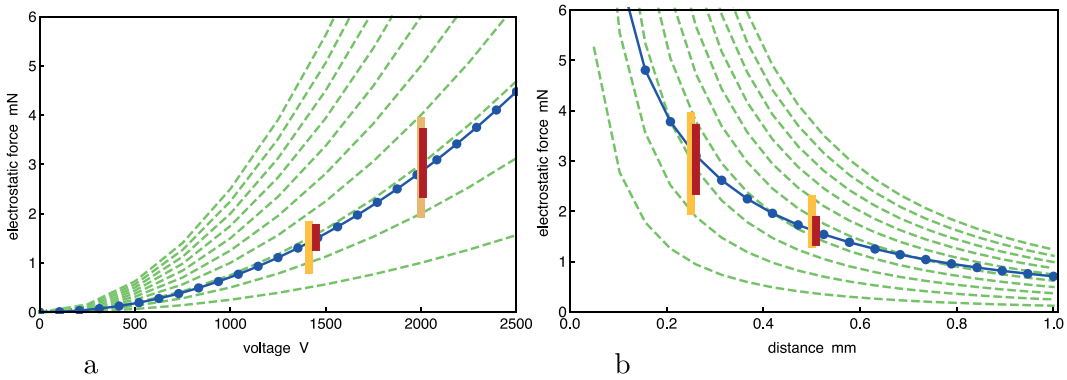

FIGURE 3.11: Comparison of experimental and numerical results for probabilistic model and analytical predictions: (a) scenario (ii): varying the applied voltage from 0 to 2000 V at constant distance of 0.25 mm. (b) scenario (i): varying the distance between fingerpad surface from 0.1 to 1.0 mm at constant applied voltage of 2000 V and Grey vertical stripes denote experimental results $\pm\sigma$, whereas dark stripes denote the results of a probabilistic model; dashed lines plot analytical solution for different contact areas, varying from 10 to 100 mm^2.

3.11 – blue solid line).

In order to quantify the dispersion of experimental results a *probabilistic model* of a fingerpad was developed employing the LHS method [102–105], where distance between fingerpad and the plate, *stratum corneum* thickness and fingerpad dimensions were selected as the most influential random variables. Variability of other parameters (material parameters, fingerprint dimensions, etc.) was neglected due to minimal influence on the results in the considered scenario of fingerpad hovering above the plate. Although great care was taken when micro-positioning the fingerpad, small errors were inevitable. By repeating the experiment three times for each participant, we were able to conclude that the fingerpad was held still at the current position, Fig. 3.9 and also to estimate the scale of error of setting the position. The applied voltage and the thickness of the insulator were controlled and therefore not recognised as a random variable in the simulations. The selected random variables with estimated mean values and unbiased coefficients of variations are presented in Table 3.5. It was assumed that there is no correlation between the distance–*stratum corneum* thickness and distance–fingerpad dimensions, whereas correlations between selected fingerpad dimensions were taken into account as observed from measurements. Since all the selected random variables take only positive real values, the log normal distribution was assumed for all of them except for fingerpad distance where extreme value distribution was employed. The selected distribution functions were confirmed by the Kolmogorov-Smirnov test. The results of

	parameter	mean value [mm]	coefficient of variation	distribution type
i	fingerpad distance	0.25 (0.50)	0.10	extreme value
ii	*stratum corneum* thickness	0.38 (M), 0.20 (F)	0.30	log normal
iii	fingerpad dimension A	16.70	0.08	log normal
iv	fingerpad dimension B	12.80	0.09	log normal
v	fingerpad dimension C	26.10	0.05	log normal

TABLE 3.5: List of random variables, their estimated mean values and biased coefficients of variations

a probabilistic model are shown in Fig. 3.11 (vertical blue bar).

The results of the analytical model of parallel plate capacitors with inclusion of air layer, Eq. 3.17, were also compared to experimental values. The contributing area A is hard to estimate a priori, therefore its value was varied from 10 to 100 mm^2 with steps of 10 mm^2, for the same scenarii as in the best estimate model (Fig. 3.11 – green dashed lines). The analytical approach shows good agreement with experiments and numerical results for varying voltage (Fig. 3.11a at $A = 30$ mm^2), which proves the parallel plate capacitor assumption ($F_e \sim V^2$), but fails to describe the change of the imposed electrostatic force with varying the plate distance (Fig. 3.11b).

3.5.5 Conclusion

The electrostatic force model was included into a 2D mechanical model of the finger and the predicted attractive forces compared with the performed experiment. The variability of the parameters influencing the electrostatic attraction were considered and the dispersion of the experimental result predicted for a finger floating over an polarised plate. Moreover, a better prediction of the experimental data of electrostatic attraction force was achieved by the consideration of the correct surface geometry of the finger pad.

In the next section, the case where the finger is in contact with the polarised plate will be considered.

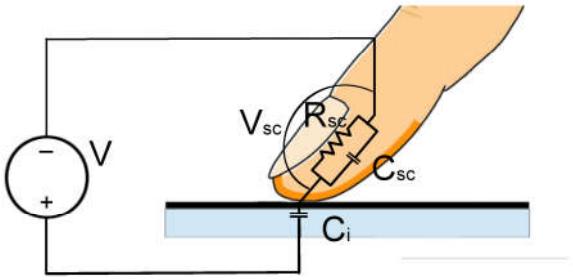

FIGURE 3.12: Electrical representation of the *stratum corneum*

3.6 Electrical Modeling Analysis

In this section, the implementation of a refined electrical modeling of the finger pad allows to explain the dynamic behavior of the electrostatic force during the contact phase between the finger and the plate.

3.6.1 Frequency Dependence of the Parameters

Each human tissue exhibits specific electrical characteristics; in this case, it is interesting to investigate the properties of the *stratum corneum* for its relevant role in the electrovibration force generation. The electrical properties of the *stratum corneum* were investigated by Yamamoto et al. [88]. In their work, the strong frequency dependence of the resistivity and permittivity is reported for this biological material due to its intrinsic structural characteristics.

In our modeling we are going to include the parametric dependences of the *stratum corneum* properties. For simplicity, the resistivity of deeper tissue is neglected for its low value, and the contribution of the air shown in the previous section is not considered. It is possible to model the interface of the finger and the insulator as shown in Fig. 3.12 with R_{sc} and C_{sc} the resistance and the capacitance of the stratum corneum, and C_i the capacitance of the insulator. From electrical circuit theory it comes:

$$v_{sc} = \frac{R_{sc}C_i s}{1 + R_{sc}(C_{sc} + C_i)s} = \frac{C_i}{C_{sc} + C_i}\frac{\tau_d s}{1 + \tau_d s} \tag{3.19}$$

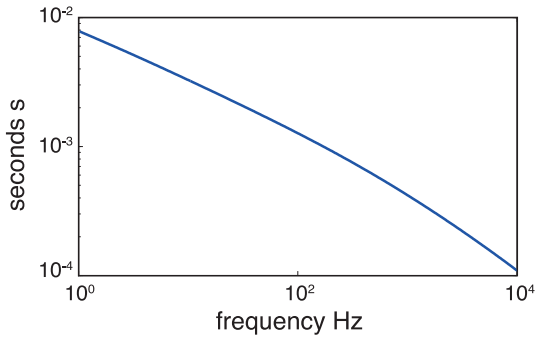

FIGURE 3.13: τ_d frequency dependence, $\tau_d = \epsilon_0 \epsilon_{sc} \rho_{sc}$

where $\tau_d = (C_i + C_{sc})R_{sc}$. For a given material, characterized by a thickness d, and a contacting area A:

$$R = \frac{\rho d}{A} \tag{3.20}$$

where ρ is the material resistivity. In the studied case, a plastic film has been used to insulate the finger from the electrode, leading to $C_i = 32pF$ where $\epsilon_i = 3.35$, $d_i = 90$ µm and the contact area between the finger and the plate is estimated as $A = 1cm^2$. For the stratum corneum, $C_{sc} = 6.9nF$ with $d_{sc} = 200$ µm [1] and $\epsilon_{sc} = 1560$ [88]. It is possible to assume $C_{sc} >> C_i$, which leads, to $\tau_d \sim C_{sc}R_{sc} = \epsilon_0 \epsilon_{sc} \rho_{sc}$. In Fig. 3.13, where the frequency dependence of the time constant τ_d is represented; Now let us consider the results from [88], where the parameters ϵ_{sc} and ρ_{sc} were measured in function of the applied voltage frequency. If we compute the time constant τ from these values, it gives the results represented in Fig. 3.13. It may be noticed that there is a strong frequency dependence of this time constant which substantially changes the behavior of Eq. 3.19 from a pure first order high pass filter.

3.6.2 Loss of Charge During Contact

In addition with the previous phenomenon of frequency dependence, it has to be considered the charge lost through the *stratum corneum* when the contact occurs. The lost charge is gathered on the surface of the insulator as free surface charge, for this reason it no longer participates to the generation of the force on the finger, and consequently, to the measured force. This happens because the charges on the surface of the insulator are no longer mechanically bounded to the finger and the insulator sustains the induced

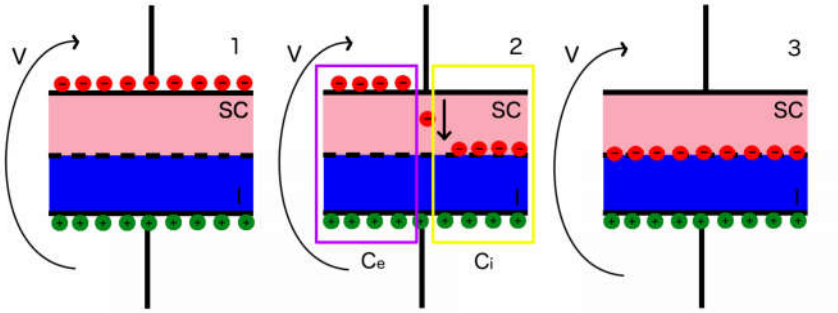

FIGURE 3.14: Charge configuration at the border of the *stratum corneum* (SC) and insulator (I). The conductive part of the system is represented like the electrode of a capacitor. 1) Initial configuration on the charge when the voltage v is applied. 2) Discharge through the *stratum corneum* with the two equivalent capacitors. 3) Final configuration of the charges after the transient.

electrostatic force. Fig. 3.14 illustrates three different moments of the discharge through the *stratum corneum*. The electrostatic force generated by v associated to the first configuration is described by Fig. 3.14 -1, but in the third configuration the electrostatic force between the finger and the polarized plate is 0 for the reason explained before. During the transient period represented by the second case, it is possible to imagine the applied voltage v, distributed across two different perfect capacitances. These capacitances are C_e formed by the case 1, where the charge is still on the finger, and C_i formed by the case 3, where the charge has migrated through the *stratum corneum*. It gives:

$$v = v_e + v_i = \frac{Q_{sc}}{C_e} + \frac{Q_i}{C_i} \tag{3.21}$$

where v_e and v_i are the voltages at the terminals of the capacitors C_e and C_i, and Q_{sc} and Q_i are respectively the charge on the *stratum corneum* and the insulator. The link between the two charges is determined by the rate at which the charge flows through the stratum corneum. The capacitor contributing to the electrostatic force between the finger and the insulator is C_e, because it is the only one that has a charge bounded to the finger. Then the effective part of the applied voltage contributing to the force is:

$$v_e(s) = Q_{sc}/C_e = \frac{C_{sc}v_{sc}}{C_e} = \frac{C_{sc}}{\frac{((C_iC_{sc}}{(C_i+C_{sc}))}} \frac{C_i}{C_i + C_{sc}} \frac{\tau_d s}{1 + \tau_d s} v = \frac{\tau_d s}{(1 + \tau_d s)} v \tag{3.22}$$

It is possible to recover the effective force acting on the finger by replacing v in Eq. 3.12 with v_e to take into account the effect described above:

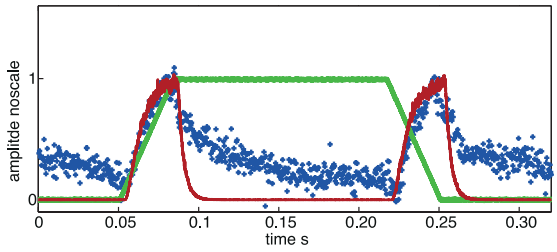

FIGURE 3.15: Lateral force measured for the finger sliding at constant speed on the polarized plane (continuous green line), in red - continuous line, it is reported the modeled electrostatic force acting between the *stratum corneum* and the insulator, and in blue dots the experimental results.

$$F_e = \frac{\epsilon_0 A v_e^2}{2\left(\frac{d_{\mathrm{sc}}}{\epsilon_{\mathrm{sc}}} + \frac{d_{\mathrm{i}}}{\epsilon_{\mathrm{i}}}\right)\left(d_{\mathrm{sc}} + d_{\mathrm{i}}\right)}. \tag{3.23}$$

It has to be noticed that ϵ_{sc}, as shown in the previous section, has a frequency dependence [88] taken into account in this modeling.

3.6.3 Simulated and Experimental Results

From Eq. 3.23, it is possible to predict the time evolution of the lateral force F_t for a given applied voltage signal thanks to Eq. 3.13. The evolution of the measured lateral force compared to the predicted one is proposed in Fig. 3.15. The plate is polarized with a trapezium signal from 0 to $1000V$ to investigate both the transient and the steady states. The signal is provided by an amplifier (HVA2kV, Ultravolt, USA) with a safety system to avoid any electrical shock and to limit the current to $I_s = 250\mu A$ as detailed in [84]. The mechanics of the finger and the measurement system have not been considered in this modeling.

The reported behavior has been observed on 8 different subjects, both male and female, aged from 22 to 29. Three of them were students and the other five were from the laboratory staff, all of them gave their informed consent to perform the experiment. It is possible to remark a close behavior between the proposed modeling and the experimental results on the rising steps, however on the discharging parts, there is a difference between the modeled and the measured signal. One assumption to explain this phenomenon could be the measurement system that can show relaxation behavior, or that the increased interface force generates a local plasticization of the superficial tissues that results in a increased contacting area, leading to a greater friction in the following time. Nevertheless

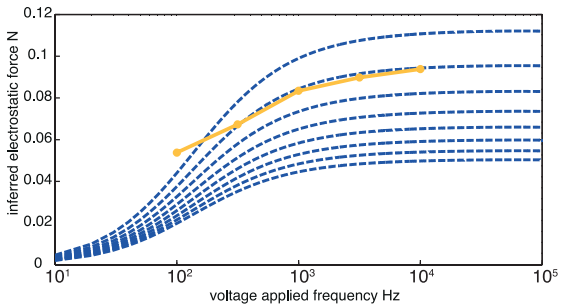

FIGURE 3.16: Comparison of the model with experimental data taken from [86]. The different lines corresponds to different thickness of the stratum corneum.

the modeling is able to take into account the discharge phenomenon of the finger. The absolute value of the measured force varies from 2 to 5 mN whereas the model, for a thickness of the *stratum corneum* about 0.2 mm, predicts 2.5 mN, in accordance with the bibliography comparison reported in the previous section. The variability of the force can be explained by the variability of the finger properties as explained in the previous section. It may be noticed that Giraud et al. [84] found a value of the decay of the lateral force, considering the mechanics of the measurements system, of $\tau_d = 6$ ms for a square signal applied. The calculated value of τ_d with our modeling, considering the same experimental situation reported in [84], is 7.7 ms.

Another way to assess the relevance of this modeling is to compare with the experimental results from Meyer et al. [86], Fig. 3.16. In their paper, the authors investigated the frequency dependence of the electrostatic force from 100 to 10000 Hz. The inferred measured force had a noticeable dispersion between different subjects, but generally exhibited an increasing and a successive saturation for all the measure detailed in their article. The dispersion of the force is well explained by Eq. 3.23, considering the variability of the thickness of the *stratum corneum* in human fingers reported in [1], and as explained in the previous section. The model we propose is compared with one result from [86], it is reported in Fig. 3.16. According to the different experimental situations described in [86], the approximation of $\tau_d = C_{sc}R_{sc}$ is not valid anymore for the comparable value of C_i and C_{sc} therefore, in the shown simulation, it has been considered $\tau_d = (C_i + C_{sc})R_{sc}$.

3.6.4 Conclusion

In this section, the influence of varying electrical properties of the skin and a more refined electrical model of the system allowed to explain and predict the absence of the electrostatic force for a DC voltage applied. It is also shown that the frequency dependence of the electrostatic force is explained by the frequency behavior of its electrical properties.

3.7 Influence of air layer during finger sliding

In this section, the influence of the trapped air layer between the fingerprint ridges on the induced modulation of the friction during sliding will be presented.

In order to estimate the influence of the air layer on the imposed electrostatic force during sliding of a finger pad on a tactile display, a series of simulations with the FE model previously developed was performed. The finger pad model was pressed against the screen until desired normal force (0.1 to 1 N by a step of 0.1 N) was achieved, then the effective voltage $v_e = 1000$ V was applied. Based on the deformed shape, the imposed electrostatic force was determined for four cases: finger pad with and without fingerprints and with and without the air layer (Fig. 3.17). Results are also compared with an analytical result obtained using Eq. 3.23, i.e. similar to the values obtained for a finger pad without fingerprints and without the air layer. The study shows that the air layer plays a major role in case of light touch, since it provides main contribution to the electrostatic force (Fig. 3.17, blue lines, left ordinate). The increase in the friction, at vertical force levels typically used for touchscreen exploration (∼0.5 N, i.e. 0.05 N/mm), is in order of 10–20 % (Fig. 3.17, blue lines, left ordinate).

3.8 Material Dependence

3.8.1 Influence of the Insulator Thickness on the Electrostatic Force

The thickness of the insulator play an important role into the determination of the electrostatic force induced by the device. The choice of the insulator between the tactile

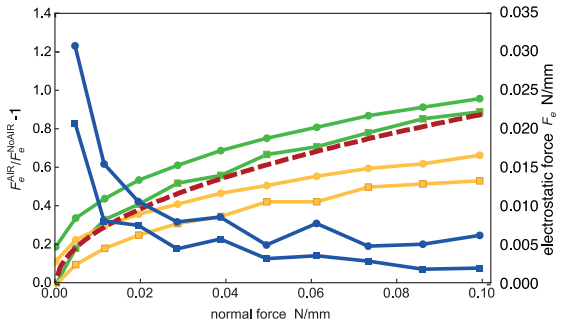

FIGURE 3.17: The figure depicts relative contribution of air layer to the electrostatic force in relation to normal force (blue lines, left ordinate) and electrostatic force in relation to normal force (right ordinate). In case of relative contribution versus normal force, solid blue line with circle disk plot marks denotes the situation with fingerprints and solid blue line with square plot marks denotes situation without fingerprints. In case of electrostatic versus normal force, green lines depict the numerical results obtained without modelling fingerprints while orange lines orange lines depict the simulations with fingerprints. In both cases, disk plot marks denote case with inclusion of the air layer and square plot marks simulations where air layer is neglected. Solid purple line plots analytical predictions according to Eq. 3.23.

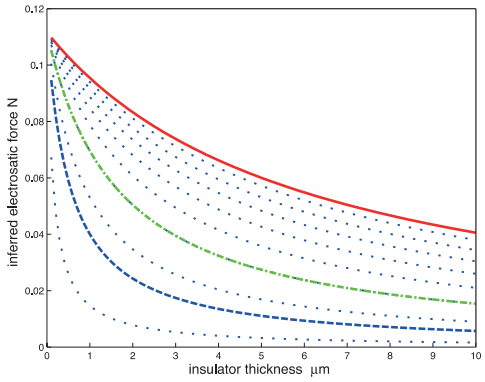

FIGURE 3.18: dependence of the induced electrostatic force as a function of the insulator thickness. Each line corresponds to a given materials characterized by its dielectric constant, from 1 (bottom line) to 36 (upper line). In red the predicted results for zirconium dioxide, in green for the zirconium oxide and blue for the glass.

plate and the finger needs also to commit requirements of wear resistance and in the case of application to tactile screens, to be transparent. The dependence of the electrostatic force as a function of the insulator thickness for a sinusoidal voltage at 10kHz, 140 V P-P, which corresponds to a $v_e \sim 140$ V, is computed from the reported relation Eq. 3.23. The result is reported in Fig. 3.18.

3.8.2 Influence of the Insulator Permittivity on the Electrostatic Force

A parameter influencing the generation of the electrostatic attraction in the finger is the permittivity of the insulator. The dependence of the electrostatic force as a function of the insulator electrical properties is reported in Fig. 3.18. In the picture, three reference materials are reported: silicium dioxide (glass), zirconium oxide and zirconium dioxide (zircona in crystalline form). Best performances can arise just with the substitution of the insulator with a more adapted one.

3.9 Conclusion

Electrostatic attraction is the second main technique available to modify the finger friction while sliding on an active surface. In this chapter, both literature models explaining the features of the electrostatic forces between the finger and a high voltage supplied plate were tested. Through a phenomenological and theoretical analysis, it was concluded that just one of the two models was suitable to be considered for a refined analysis.

A finite element model of the finger pad was developed including the expression of the electrostatic attraction between the finger and the plate. Through a discretization of the infinite parallel plane assumption, supported by the axial symmetry of the system, it was possible to propose a coupled electro-mechanical model of the finger pad interacting with a high voltage supplied plate. The predictions of the model were compared with experimental data gathered without contact between the finger and the plate to avoid artifacts deriving from the tribology measurements. The range of variability of the experimental data were predicted with the consideration of the variance of the physical values influencing the generation of the electrostatic force, assessing in this way part of the great range of perception of the electrovibration stimulus among different users.

A refined electrical modeling of the plate-finger contact was proposed with the consideration of the variable electrical properties of the *stratum corneum* in function of the frequency of the applied voltage. By these means, the dynamic of the charge at the interface between the finger and the tactile plate was exemplified, and just the contribution of the bounded charge to the finger was considered in the prediction of the

electrostatic force. The model prediction was validated with performed measurements and comparison with literature data.

Moreover, the influence of the bounded air layer beneath the fingerprint and the plate on the total electrostatic attraction was predicted, and it can account of the 10-20 % of the total attraction while the finger is interacting with the tactile device.

In the end, a discussion about the insulator properties was outlined to enhance the performance of the electrostatic based tactile devices.

In the next chapter, both electrostatic and ultrasonic friction modulation techniques will be coupled in a single device, and the physical and perceptual independence of both techniques will be proven.

Related pubblicatons to this chapter are:

- E. Vezzoli, M. Amberg, F. Giraud and B. Lemaire-Semail, Electrovibration Modelling Analysis, Haptics: Neuroscience, Devices, Modeling, and Applications, EuroHaptics 2014, pp 369-376.
- T. Vodlak, Z. Vidrih, E. Vezzoli, B. Lemaire-Semail, and D. Peric, Multi-physics modelling and experimental assessment of electrostatic force for electrovibration based haptic displays, submitted to Biotribology
- Z. Vidrih and E. Vezzoli, Electrovibration Signals Design: A simulative approach. Haptics: Perception, Devices, Control, and Applications, EuroHaptics 2016, pp 304-313,

Chapter 4

Coupling Electrovibration and Ultrasonic Vibrations for Friction Modulation

4.1 Introduction

In the previous chapters, two different techniques available to modify the users' perception of the surface were analyzed, having an opposite effect on the perceived friction: ultrasonic vibrations reduce the friction between the finger and the plate, whereas electrostatic attraction increases it. The range of sensation provided by the two friction modulation techniques can be enlarged due to their opposite influence on the perceived friction allowing a better rendering dynamic of the simulated texture. The aim of this study is to show that the two principles can be added independently in the static, dynamic and perceptual points of view. This work has been performed in collaboration avec Wael Ben-Messaoud, PhD student in L2EP.

The earliest attempt to couple ultrasonic vibrations and electrovibration was performed by Giraud et al. [84], confirming the technical possibility to use them together. In this chapter, the development of the device able to combine both techniques will be depicted, and the independence of the two friction modulation techniques will be shown in the static regime; then an analysis of their dynamic behavior will be performed. In the

end, a psychophysical experiment showing the independence of the two effects from the perceptual point of view will be presented.

4.2 Haptic Stimulators

In this section, the two different tactile stimulators developed for these experiments will be presented. A standalone stimulator will be employed for the static measure and psychophysical evaluation, because it performs simultaneously the two effects; whereas a fast response stimulator will be employed in the dynamic behavior study.

4.2.1 Standalone Stimulators

The haptic stimulator used for the static and the psychophysical experience is based on a modified USB-standalone version of the STIMTAC [56]. The tactile plate in aluminum used in this experiment has a resonant frequency of 38220 Hz at ambient temperature. In this modified version, the stimulator has the inverter electrically insulated from the vibrating plate. In this way, it was feasible to introduce an amplifier to apply a high voltage to the tactile plate inducing the electrovibration effect. The utilized amplifier (UVA2kV, Ultravolt, USA) coupled with a signal generator provides a programmable voltage modulated at 440 Hz. To perform the static measure, in order to monitor the forces and the friction coefficient, a 6 axis force sensor (nano 43, ATI, USA) was used to ensure a resolution of 7.8 mN with a sampling period of 400 µs. To measure the vibration amplitude, an interferometer vibrometer was focused on the plate. To perform static measure, the tactile plate has been unmounted from the tactile stimulator and placed on the force sensor, Fig. 4.1. At last, data are acquired with an oscilloscope (3014B, Tektronik, USA) then post-processed through Matlab.

4.2.2 Fast Response Stimulator

The previous stimulator was designed to couple the two strategies in steady state, for this reason the ultrasonic plate have not been optimized on a dynamic point of view, resulting in a reduced bandwidth. To perform the dynamic behavior measurement, a specific, tactile stimulator was designed, ensuring a fast mechanical time response of

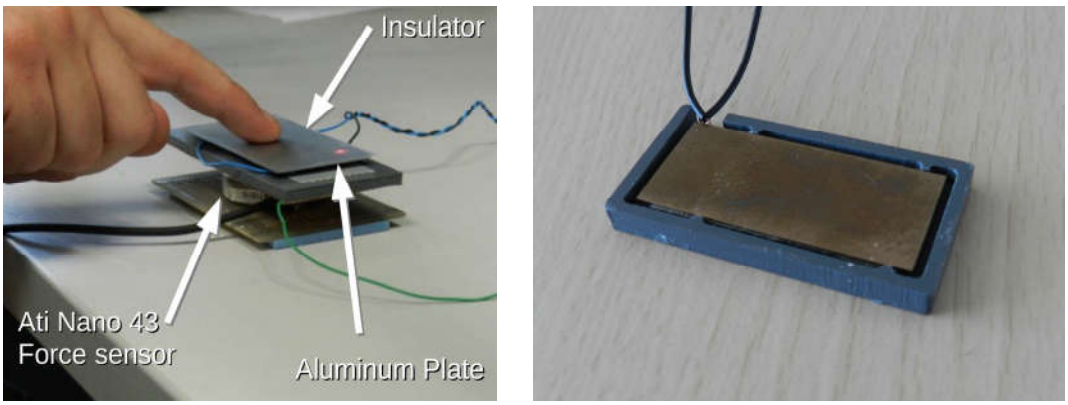

a b

FIGURE 4.1: (a) static measurement system. The red spot on the plate is the focus of the laser of the vibrometer. (b) picture of the fast response stimulator.

the vibrating plate. It is needed to monitor the vibration amplitude of the plate itself because it is the effective parameter responsible for the generation of friction reduction as shown in chapter 2. This plate has been equipped with five piezoelectric ceramics, four of them are used as actuators and one of them is used as a sensor. To calibrate the relationship between the signal provided by the ceramics and the effective vibration of the plate, a laser vibrometer has been used (OVF-5000, Polytech, Germany). To guarantee consistency with the previous setup, the wavelength of the vibration mode and the plastic film used to insulate for electrovibration are identical in both cases, Fig. 4.1b. It may be noted that this plate was not designed to stimulate the finger with the two different technologies simultaneously.

4.3 Physical Coupling

4.3.1 Static Independence

In this section, it will be demonstrated that there is no influence between the two tactile stimulation techniques while coupled. Electrovibration and ultrasonic vibrations act in opposition: electrovibration increases the normal force between the pulp of the finger and the plate whereas in the ultrasonic devices a reduction of the friction is experienced. In particular, it is possible to express the lateral force, F_t, felt by the finger in an hybrid

stimulator as:

$$F_t = \mu(w)(F_n + F_e), \tag{4.1}$$

where the friction is assumed Coulombic. To propose this formula, it is assumed that there is no mutual influence between the friction modulation induced by electrovibration and ultrasonic vibrations as shown in the following sections. This assumption is also motivated by the finding depicted in chapter 2 that the friction modulation induced by the ultrasonic vibrations is independent of the normal load applied, thus it should not be influenced by the increased normal load induced by the electrostatic attraction.

The friction force and the normal force of a finger sliding on a tactile stimulator were recorded while the effects have been coupled with different phases. Five participants gave their informed consent to perform the experiment, which was carried out in free exploration by the users. The data were recorded after a period of training to assume the normal force constant as well as the speed. Before the experience, the subject was asked to wash his hands and completely dry them with talcum powder, and 10 minutes waited to let the skin equilibrate. To avoid the deposition of moisture on the plate, the exploration was allowed just 30 seconds before having a pause of 30 seconds to let the finger dry.

The value of the normal force applied by the user on the stimulator was provided by the oscilloscope, allowing a visual feedback. The experiment was performed with 3 different phases between the two effects (0, 90 and 180 degrees) to study different possible interactions between the two principles, Fig. 4.2. Before the starting of the experiment, the two effects have been singularly tuned to induce a similar tangential force modulation $\pm\Delta F_t$ on the finger performing the experiment. Fig. 4.2a represents the case where the electrovibration effect and the ultrasonic vibrations are applied in phase. For a constant normal force applied by the finger while sliding, it has been recorded a constant lateral friction force. On a different phase (90 degrees) between the two friction modulation techniques, a stair modulation appears on the measured lateral force, Fig. 4.2b.

From all the performed measurements of one participant (about 50 tries), the friction coefficient μ has been computed for each considered case: electrovibration applied $\mu(EV, 0)$, ultrasonic vibration applied $\mu(0, UV)$, no friction modulation $\mu(0, 0)$ and both effects applied $\mu(EV, UV)$. The average on the performed measurements on one participant is

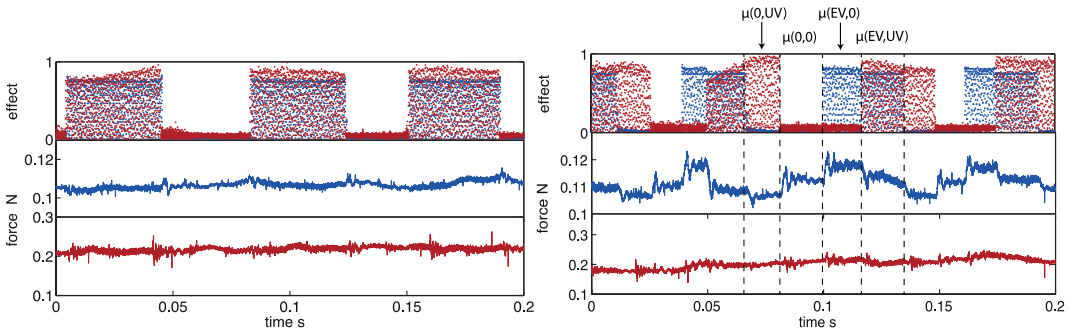

FIGURE 4.2: Measure of coupling of electrovibration and ultrasonic vibrations in phase (a), and in quadrature (b). In the first graph is reported the presence of the effect, electrovibration (blue) and ultrasonic vibrations (red). In the second graph is reported the recorded lateral force. In the third graph is reported the measured normal force.

TABLE 4.1: Phase and Opposition Ratios

participant	1	2	3	4	5
phase ratio	-0.9%	-1.2%	0.8 %	1.1 %	0.4 %
opposition ratio	16%	3.9%	9.2 %	14.4 %	7.3 %

reported in Fig. 4.3. The phase opposition ratios are defined (see table 4.1) to characterize the difference between friction coefficients obtained respectively when the two effects are in phase and in opposition for each of the five participants. The phase ratio is equal to $1 - \mu(EV, UV)/\mu(0, 0)$, where UV is ultrasonic vibrations and EV electrovibration, and the opposition ratio is equal to $1 - \mu(EV, 0)/\mu(0, UV)$

These measurements substantially confirm that the two techniques are fully mixable and that there is no mutual influence between the two in the static regime on the tribological point of view: indeed, as the opposite effects were initially tuned to achieve respectively $+\Delta F_t$ and $-\Delta F_t$, Fig 4.3 shows that, qualitatively, the resulting effect after coupling, tends towards zero when in phase, and towards $2\Delta F_t$ when in opposite. This is also assessed in Table 4.1 by the low value of the phase ratio. Moreover, it is possible to find a level of the two effects to fully compensate each other and the resulting induced modulation of the lateral force.

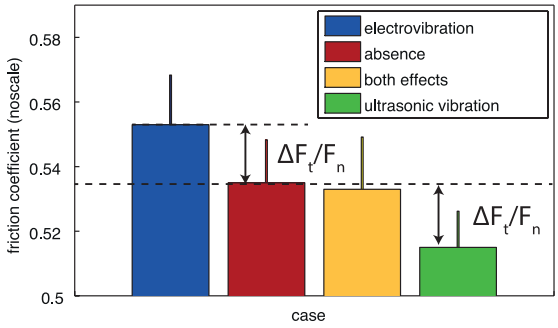

FIGURE 4.3: Calculated μ for the different modulations in the considered cases. When the effects are regulated to induce the same friction modulation, their coupling results in a compensation of the induced friction modulation

4.3.2 Dynamic Behavior

In this section, the possibility to couple the two effects also on a dynamic point of view will be discussed. For this experiment, the fast response stimulator presented in section 4.2.2 was used. To compare the two effects, their rise time has been measured. This one is defined by the delay measured between the 10% and the 90% of the equilibrium value of the tangential force measure, after the application of the excitation. To perform this experiment, the tribometer detailed in chapter 2 was used due the large bandwidth (1 kHz). A similar experience was performed by Meyer et al. [86]; they measured the response of the tangential force to a reference step either due to ultrasonic vibrations or electrovibration, for different finger speeds. In the cited work, the rise time was measured between the control signal (the voltage supplied) of the device and the measured lateral force, which implies the inclusion of the mechanical response of the plate, as well as the dynamic of the amplifier in the measurements. In our case, we are interested into the dynamic of the physical effect, for this reason, to perform this measure, it was necessary to record the parameter generating tactile stimulation: the vibration amplitude for the ultrasonic devices and the voltage applied for the electrovibration. Moreover a unique surface to exploit both experiments is required to compare the two effects. For a similar plate design than the one used in [86], it was found a mechanical time response of the plate vibration mode of about 15 ms. This could be the cause of this discrepancy between the two stimulation principles. For this reason, the fast response stimulator described before has been used to conduct these experiments. This plate has a measured mechanical time response around 1.5 ms. In Fig. 4.4 the measurements recorded on the same subject of the aforementioned analysis are presented. Each line represents the

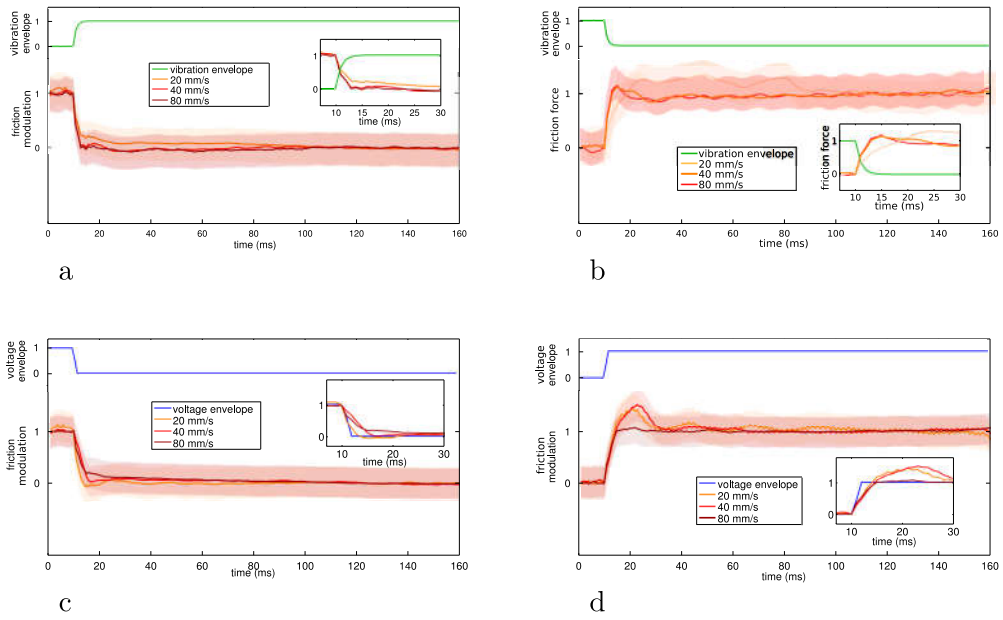

FIGURE 4.4: Friction modulation for different finger speeds related to the measured plate vibration or voltage envelope reported in the figure. The shadowed area represents the measure standard deviation. (a), descending friction ultrasonic devices, (b) increasing friction ultrasonic devices, (c) decreasing friction electrovibration and (d) increasing friction electrovibration.

average of about 50 measurements.

The tangential force response of both effects was analyzed for an increase and decrease of friction modulation. The green line represents the vibration envelope of the plate. The plate vibration was set at 2 µm peak to peak with the presence of the finger. To ensure a uniform mechanical behavior of the finger, the normal forces for the reported measurements are equal to 0.3 ± 0.05 N. At this point, it was possible to proceed with the identification of the model to link the parameter generating the friction force modulation. To do so, the MATLAB toolbox for Black-Box modeling has been utilized considering a second order model. The input parameter has been the vibration amplitude envelope for the ultrasonic device and the applied voltage envelope for electrovibration. For each situation, the calculated model has been evaluated with a step function to investigate the actual behavior of the effect itself. In accordance with the approach reported in [86], the parameter evaluated to compare the effect has been the rise time of the response of the identified model to the step. The results are reported in Fig. 4.5, and analyzed in the discussion section.

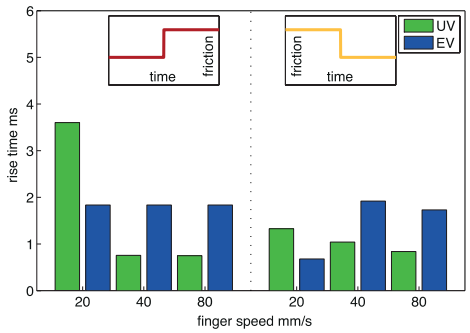

FIGURE 4.5: Rise time of the step response for the identified models based on the previous measures for the two different friction cases considered: mounting friction (left) and descending friction (right).

4.4 Perceptual Independence

In the previous section, it is shown that it is possible to compensate the effect of both technologies on the lateral force, however, it is not clear if physical principle itself can be perceived by the user. So, in this section, a psychophysical experiment will be presented, showing the possibility to find a level of compensation between the two effects, at which the user cannot distinguish between a surface with compensated friction modulation, and a surface without any friction modulation. To perform so, the standalone stimulator was programmed to induce a friction reduction on the plate following a sinusoidal profile, with a spatial wavelength of 1 cm. Then, it has been implemented the same spatial profile with the electrovibration. It was possible to adjust the electrovibration maximal voltage applied to the plate on eight different levels, from 0 to 2000 V. The levels were equally spaced with a singular amplitude level of 287 V. The aim of the experiment is to know if for all the users, it was possible to find a level of electrovibration where the friction modulation induced by the ultrasonic vibration was totally compensated and the plate surface was perceived as uniform. It was asked to ten subjects to freely explore the tactile plate while maintaining the normal force applied around 0.4 N. It was necessary to introduce this limitation to ensure that the vibration damping of the plate induced by the presence of the finger was stable. To avoid any noticeable difference into the dynamic of the two effects and the time response of the system that could induce distortion into the perception of the surface, it was asked to the participants to maintain a constant exploration speed (smaller than 40 mm/s). All the participants gave their informed consent for the execution of the experiment. It was asked to the subjects to wear an anti-noise headset. The value of the normal force was provided

via a graphical interface to the subjects. Before each experiment, the tactile plate was cleaned and the participants were invited to wash their hands and dry them with talcum. Before starting the experiment, the participants had the time to get used to the friction modulation induced by the ultrasonic vibration with the compensation effect induced by electrovibration set to 0 (no effect of increased normal force). When the participant communicated that he was ready and exhibited a stable normal force while exploring the plate, the experiment started. The level of electrovibration was increased by one step and the subject was asked how the surface was and how it was in comparison with the set-up situation. The participant could describe the surface as non uniform or uniform, then the level of electrovibration compensation was increased by another step. To avoid moisture deposition, the exploration of the plate was allowed for 20 seconds with 20 seconds of pause to let the finger dry. After each participant, the tactile plate was cleaned to remove any remaining deposit. The starting level of compensation was always available to the users to compare the friction modulation. Every participant could find a level of electrovibration which fully compensates the friction modulation induced by the ultrasonic vibration. After finding the level where the modulation was not perceived anymore, the procedure has been repeated from a random compensation level. All the participants indicated the same level as before as the one exhibiting the uniform surface (see Fig. 4.6). The compensation level necessary to cancel the influence on the lateral force induced by the ultrasonic vibration exhibits a huge variability between the subjects. The variability of the compensation force can be explained by the variability of the thickness of the *stratum corneum* on the human fingertip [1] or its water content, which strongly influences the induced electrostatic force on the finger [106], as well as the variability of the friction modulation induced by ultrasonic vibration as exemplified in chapter 2.

4.5 Discussion

The static dependence measure confirmed that it is possible to constructively couple the two effects to enhance the range of lateral force modulation experienced by the finger. Moreover, it has been demonstrated that if the influence on the lateral force by the two effects is set as similar, it is possible to obtain a friction modulation equal to zero while coupling them in phase. These measurements confirm the physical independence of the

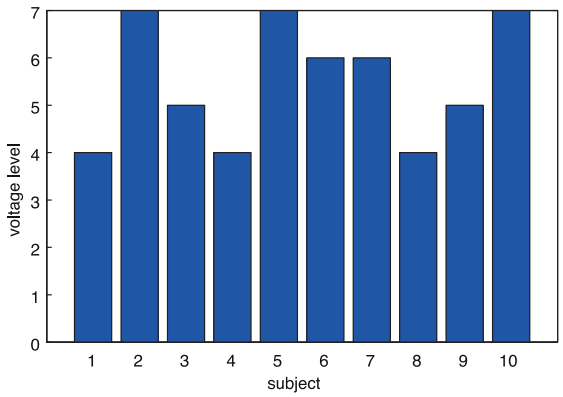

FIGURE 4.6: Compensation level of electrovibration necessary to cancel the friction modulation induced by the ultrasonic devices and have a uniform perception of the surface. Each voltage unit corresponds to 287 V.

two effects and confirm the validity of the Eq. 4.1. In this range of induced modulation, it is possible to conclude that the two effects are purely additive, and that there is no mutual influence. The measured dynamic of the two effects is an indicator of their behavior in the varying regime considering a real finger. The experiment substantially confirms that in most of the cases considered, the rising times of the two effects are comparable. Thus, they can be successfully coupled additively also in dynamic. This conclusion can be understood by considering the physical modelling introduced in Chapter 2 and 3. An exception is the case of rising friction for ultrasonic vibrations with low exploration speed (20 mm/s), this is probably due to some stick-slip effect that happened after the increasing of the friction. This phenomenon can be seen in Fig. 4.4b for the lower speed of exploration. For this reason, the rise time is higher than in the other measured cases.

To obtain a linear coupled tactile stimulator, it is necessary to design the mechanical plate and choose the amplifier for the electrovibration to match the dynamic of the two effects: the mechanical rise time of the plate for ultrasonic vibrations and the rise time of the amplifier for electrovibration have to be considered. The former is dependent on the Q factor of the plate and can be reduced to 1-2 ms, where the latter is just dependent on the amplifier and, with the right amplifier choice, can be neglected. These results are obtained considering all the device parameters which affect the stimulation principle itself and are consistent between the two different techniques. As suggested by [86], fingertip mechanical behavior plays an important role in the determination of these forces, and the analysis of these rise times is consistent with the analysis proposed by Wiertlewski et al. [107] for the mechanical response of the fingertip. Their analysis

predicts a fingertip response in the order of milliseconds, which is in good agreement for all the considered friction modulation changes.

The psychophysical experiment on the two coupled effects confirms that it is always possible to find a level where the two effects fully compensate each other. By implementing a spatial modulation of the effects (sinusoidal waveform), the compensation level reported in Fig. 4.6 shows that there is no difference, from the point of view of the user perception, between a surface with no effect, and a surface where the friction modulation is compensated. This does mean that the users cannot perceive the presence of the effects on the surface, but perceive just the impact of those effects on the lateral force.

Another important point suggested by this study is that the psychophysical results found valid for one technique may be assumed valid for the other.

4.6 Conclusion

This chapter analyzed the possibility to successfully couple two friction modulation techniques, electrovibration and ultrasonic vibrations, to expand the range of sensation provided to the users. A coupled stimulator was proposed merging both stimuli on the same surface, and the static independence of the stimuli was proven with tribology measurement. An analysis of the rise time of these two effects while sliding on a surface was proposed to analyze the possibility to couple them also in the dynamic domain. The psychophysical evaluation confirms that the effects are fully mixable and the user cannot distinguish the presence of the two compensated effects on the surface to the non-modulated one because he/she perceives this surface as uniform. The reported results suggest that the psychophysical conclusion previously found valid for one technique, may be assumed valid for the other, and that these effects just modify the user perception of the friction of the material, without modifying any other perceptual parameter.

In the next chapter, a novel tactile stimulator called E-ViTa will be developed based on the concept depicted in chapter 2. Moreover an efficient texture rendering algorithm will be proposed taking advantages of the characteristics of the human tactile perception introduced in chapter 1.

Related pubblicatons to this chapter are:

- E. Vezzoli, W. Ben Messaoud, M. Amberg, B. Lemaire-Semail, F. Giraud and M.A. Bueno, Physical and perceptual independence of ultrasonic vibration and electrovibration for friction modulation, IEEE - Transaction on Haptics, Volume: 8, Issue: 2, pp. 235-239, 2015
- E. Vezzoli, W. Ben Messaoud, C. Nadal, F. Giraud, M. Amberg, B. Lemaire-Semail, and M.A. Bueno, Coupling of ultrasonic vibration and electrovibration for tactile stimulation, European Journal of Electrical Engineering, Vol 17, Issue 5-6, pp. 377-395, 2014.

Chapter 5

Texture Rendering

In the previous chapters, an improved modelling of the ultrasonic vibration friction reduction and electrovibration has been proposed. Later on, the perceptual equivalence of the two techniques has been proven trough a device able to produce both stimuli. The main focus of this chapter is on texture rendering with friction modulation technique, and, in particular, the development of efficient algorithms to reproduce dense tactile signals with commercial hardware is proposed.

To approach the design of the stimuli, two important features of tactile recognition should be recalled: in [6], it was shown that the direction of the applied force on the fingertip is more important than the actual geometry of the object for shape recognition, whereas in [108] it was suggested that the spatial spectrum of the skin displacement can encode tactual texture. A stimulus design aiming to mimic the tactile information given by everyday object can take advantages of the two suggested approaches to provide a more natural interaction with surface haptic devices.

An important work on the rendering of spatialized texture with friction modulation device was performed by Biet et al. [57]. In this paper, the modulation of the friction based on a squared modulation of the vibration amplitude in function of the position of the finger was compared with real squared gratings.

Kim et al. [109] have observed, that despite the great user interaction opportunities haptic displays can provide, there has been little work done on designing and evaluating algorithms for generating high fidelity tactile sensations on such devices. Therefore

they have proposed an algorithm for rendering 3D bumps based on the gradient of the simulated surfaces and a friction model based on psychophysical experiments.

Another option for texture rendering consists of record – and – re-play technique [110], in which a recorded values of quantities (forces, displacements, accelerations, etc.) while exploring a real surface, are re-played when exploring a virtual surface. A publicly available database of haptic texture models, for use by the research community, is the Haptic Texture Toolkit (HaTT), which can be downloaded from the Penn University web page. HaTT includes 100 haptic texture and friction models, the recorded data from which the models were made, images of the textures, and the code and methods necessary to render the textures using an impedance-type haptic interface such as a SensAble Phantom Omni [111, 112].

Another static method may be used, it is based on gray-scale levels of the displayed image: the applied voltage/ultrasonic vibrations, modifying the friction at a location on a screen, is proportional to the gray-scale value of pixels, as it is intuitive, and relatively easy to implement, similarly as what we did in the previous chapter for the electrovibration signal in the psychophysical experiment.

A similar approach is used in [113], where friction models are recorded using the finite element modelling of tactile scenarii. An extensive database of friction profiles for simple reference standards (bump, edge, and sinusoidal surface) has been established and implemented in an artificial probabilistic neural network in an online tool "HapTex" [114]. Moreover, in the developed tool, tribological measures of different surfaces are also utilised for realistic haptic signal rendering.

While generating realistic signals is a fundamental topic, few interest was spent into the developing of efficient algorithms taking advantages of the perceptual characteristics of the tactile surface, and of the commercial interfaces available on the market. To hope to integrate these technologies into commercial smartphones or tablet, it is necessary to consider their hardware limitations.

In this chapter, the developing of the E-ViTa (Enhanced Visual-Tactile) device is described. E-ViTa is based on low-price, off the shelves components, to mimic some of the hardware constraints present into tablets and smartphones. With this device, the importance of the reproduction bandwidth is shown with a psychophysical experiment.

Following, the analysis of the classic strategy for tactile signal reproduction, here named "Position control", is compared with an original technique called "Texture control" developed following the perceptual characteristics of the finger. In the end, a broad user study on the two techniques allows to define a merged representation strategy.

5.1 E-ViTa Device

5.1.1 Structure

The device is built around the "Banana Pi" (Shenzhen LeMaker Technology Co. Ltd, China) single board computer featuring a 1 GHz ARM Cortex-A7 dual-core CPU with 1 GB of ram working in parallel with a microcontroller (stm32f4, STMicroelectronics, France). The single board computer is connected to a 5 inches flat capacitive touch screen (Banana-LCD-5"-TS, Marel, China) providing the finger position input and display output, where the sampling frequency of the finger position is 50 Hz. The communication between the microcontroller and the single board pc is provided by a SPI bus working at 10 kframes/second. This bound rate was chosen for signal reconstruction reason: to be able to reproduce a 500 Hz sinusoid with at least 20 points per period in order to reduce the distortion of the signal for linear interpolation. 4 flat resistive force sensors (CP 150, IEE, Luxemburg) are placed under the corners of the display and provide the normal force value to the microcontroller. The microcontroller synthesizes a PWM signal to pilot a voltage inverter to actuate piezoceramics. In Fig. 5.1, the structure of the device is represented, and in Fig. 5.2, is reported a picture of the device and the equivalent electrical scheme.

5.1.2 Ultrasonic Plate

The ultrasonic vibrating plate implemented in the device is a glass plate 54x81x1.6 mm^3 resonating at 60 750 Hz, where the half wavelength of the vibration mode is 8 mm. 22 piezoceramics, 14 mm × 6 mm × 0.5 mm, are mounted on the sides of the plate, each one glued along a full wavelength; 20 of which are used as motors and 2 as vibration sensors. Their unglued electrode was split along the nodal line and both halves connected to 2 complementary outputs of the voltage inverter. This setup avoids the need of electrical

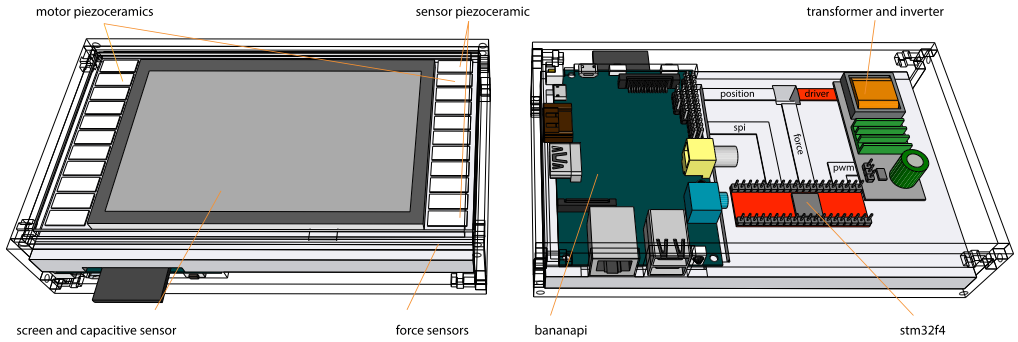

FIGURE 5.1: E-ViTa Device Structure

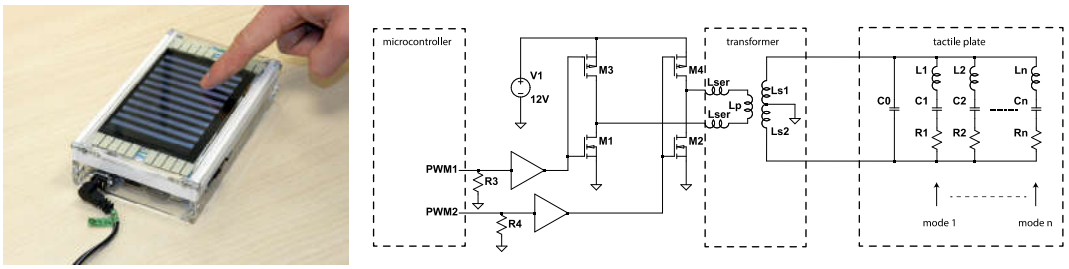

a b

FIGURE 5.2: (a) Picture of the E-ViTa device. (b) equivalent electrical scheme of the device, the PWM signal drives the inverter which supplies the transformer powering the vibrating plate. For each resonant mode m of vibration there is a series of RLC represented on the right part of the scheme.

access to the glued electrode, while maintaining it at ground voltage in order to reduce perturbations to the capacitive sensor. The cartography of the vibration amplitude of the plate is reported in Fig. 5.3a. A closed loop control on the vibration amplitude, running at 60 kHz, is implemented on the microcontroller acquiring the value of the vibration from the two piezoceramics used as sensors. The controller is a PI and its parameters were tuned with the Ziegler-Nichols method. In Fig. 5.3b, the bode diagram of the controlled system is reported. The system exhibits a bandwidth of 400 Hz at 2 µm. The closed loop control allows the stability of the vibration amplitude within a tolerance of 50 nm for a normal force applied by the fingertip lower than 3 N.

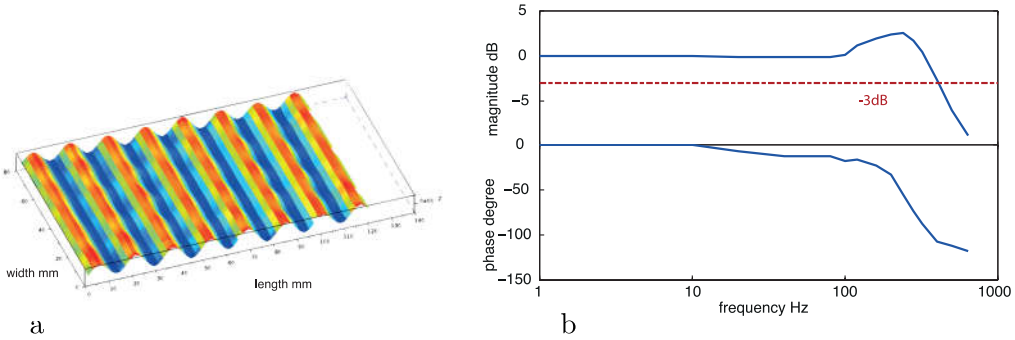

FIGURE 5.3: a, cartography of the ultrasonic vibrating plate. b, Bode diagram of the vibration response of the plate. The dashed line at -3dB indicates the bandwidth of the plate up to 400 Hz.

5.2 Friction Time Response Perception

5.2.1 Experimental Protocol

This section presents the psychophysical protocols used in the following experiment. The experiment was conducted to determine the capacity of participants to distinguish differences in the rise time of a single tactile stimulation to determine the bandwidth of perception of friction signals.

In all experiments, the participants were interacting with the tactile device described in the previous section. Ten subjects, aged between 25 and 40, participated to this study (8m. and 2f.). The ultrasonic vibrating interface sometimes makes a slight noise when alternating active and passive states. Therefore, to prevent any influence of this noise on the participant perception, the subjects had to wear noise reduction headphones and a white noise was also diffused in the room during the experiments. For each trial, the participants had to move their finger from left to right on the screen, which generates a stimulation, but they were free to choose the force and the speed of exploration. The participants had to lift their finger from the plate after each sliding.

5.2.1.1 Minimum rise time Discrimination

The minimal rise time (defined in the previous chapter, as the time necessary to increase the signal between the 10 % and the 90 %) discrimination experiment aim is to determine the capacity to perceive differences in the rise time of the friction reduction. From this

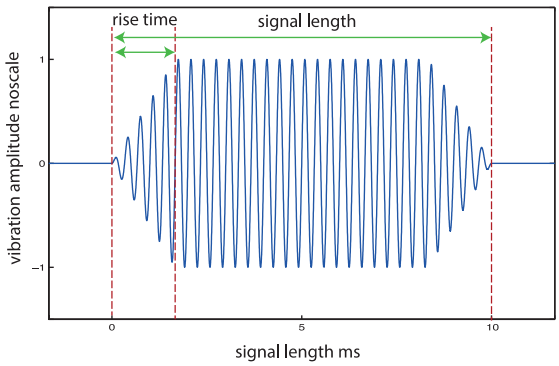

FIGURE 5.4: Voltage amplitude of the signal from the sensor ceramics. The signal is defined by the signal length and the imposed rise time of the vibration amplitude.

psychometric function, it is then possible to extract the just noticeable difference (JND) of the rise time duration for humans interacting with the ultrasonic vibrating tactile device. The experiment is based on a forced choice task with a constant pool of stimuli (constant stimuli method). The participants have to compare the sharpness of two stimuli, displayed in sequential order. A reference value of signal duration is always randomly set as one of the two stimuli presented in the discrimination task. The other stimulus is a test value to compare against the baseline. The participants explored the two stimuli up to 3 times and was then asked to report which stimulus offered the "sharpest" stimulation. They had to choose one of the signals even if not sure of the answer.

Test signals were presented in a pseudorandom order where one of the signals was always the baseline and the other selected from a list of five signal rise times calibrated in advance. The signal was always 10 ms long and the possible rise times were 0.8, 1.2, 1.8, 2.6 and 4.4 ms to be compared with a baseline of 0.4 ms, Fig. 5.4. The experiment was stopped after a signal of each length has been presented 10 times against the reference. Each of the five subjects was thus presented to a total of 50 signal comparisons. Beside, to reach these rise times, the E-ViTa device was driven in open loop with specific voltage profiles to induce the desired stimulation.

5.2.1.2 Psychophysical Analysis

In each task, the psychophysical threshold is evaluated by fitting a logistic psychometric function based on the method of maximum likelihood to the psychophysical performance

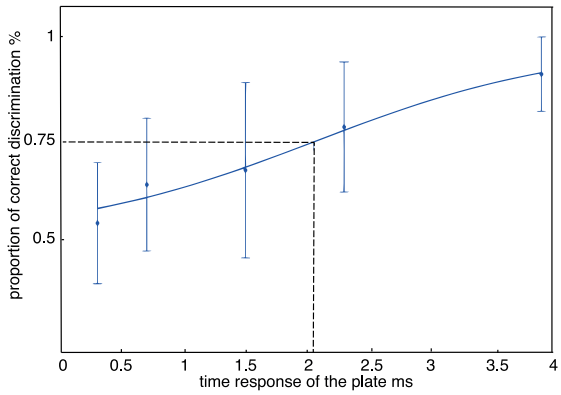

FIGURE 5.5: Just noticeable difference of signal rise time. Error bars represent the standard deviation and the line is a fit of a logistic psychometric function to the results.

of the participants. The fitting is implemented by using the version 1.81 of the Palamedes toolbox (Kingdom & Prins).

5.2.2 Results

Results from the ten subjects are presented. All the answers from the ten participants were averaged together and the standard deviation calculated. The data obtained during the trial are shown in Fig. 5.5.

To compute the just noticeable difference (JND), which represents the minimum rise time difference that can be reliably discriminated, the percent of correct answers as a function of the difference in the rise time was calculated. A logistic psychometric function bounded between 0.5 and 1 was fitted to the resulting plot. A value of 0.5 on the Y axis represents a situation where the participant performs at chance level. On the contrary, a value of 1 represents a 100 % correct discrimination from the participant. For a forced choice task with two alternatives, the JND is typically set as 75 % of correct answers. It was computed by interception of the psychometric function at Y=0.75: the overall JND for the five participants was therefore estimated at 2 ms.

5.2.3 Discussion

The JND of the rise time is around 2 ms, thus, users are able to distinguish between two frictional signals, one with a bandwidth of 175 Hz, the bandwidth associated to a step with a rise time of 2.4 ms, and the other with 850 Hz,the bandwidth associated to a step

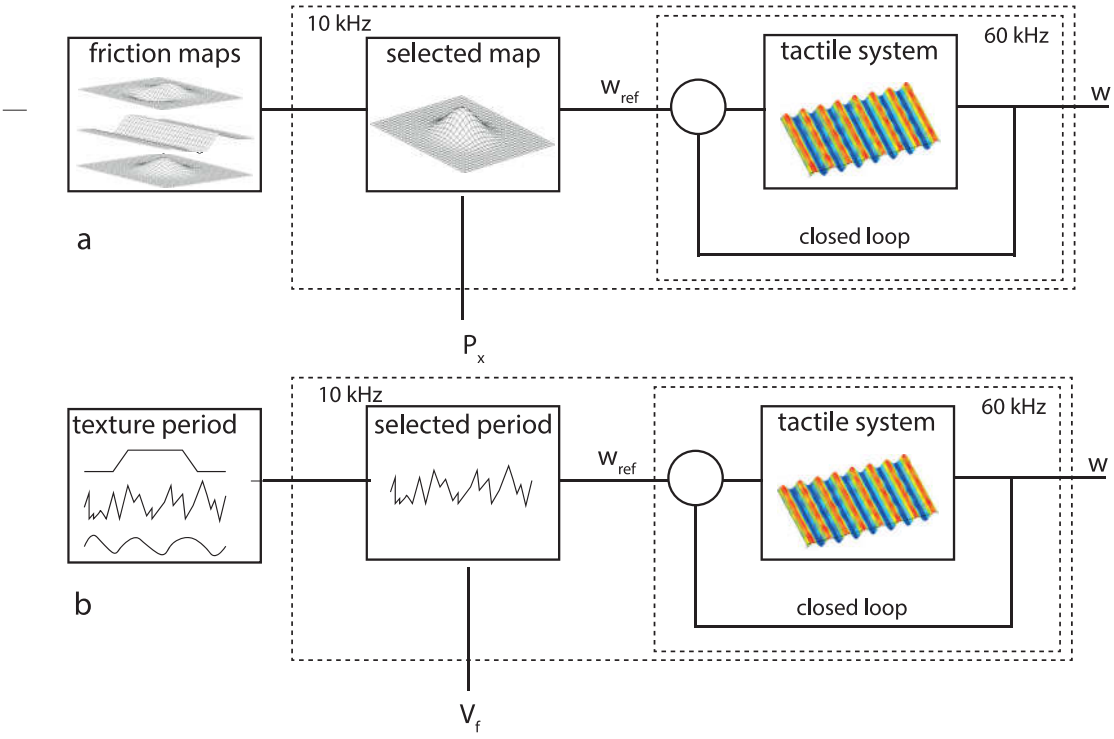

FIGURE 5.6: a, structure of the control chain for friction coefficient modulation through map representation (Position control). b, structure of the control chain for friction coefficient modulation through period synthesis (Texture control). The rate of reproduction of the selected period is dependent on the speed of exploration of the finger

with a rise time of the baseline of 0.4 ms. This experience confirms that the perception of a friction modulation signal is comparable with the perception of a vibrational signal typically around 800 Hz [115].

5.3 Texture Rendering Strategies

In this section, two different strategies for texture reproduction are introduced.

5.3.1 Position Control - Map Representation

The classical strategy to reproduce textures and objects on a flat surface through friction modulation relies on the comparison of the detected position with a map previously selected, Fig. 5.6a. It is possible to introduce a concept of "Position control" to describe this control strategy, which determines the amplitude reference value of the plate vibrations as a function of the finger position, for a given map. The Position control relies on

the accuracy and on the bandwidth of the position acquisition system to reproduce textures. This led to the implementation of different solutions to maximize the bandwidth of the position acquisition with an optical [116] or a force based [56] position detection solutions, effective, but hardly implementable on mass produced devices.

On the other hand, a noisy or low bandwidth system cannot reproduce accurately the desired signal; e.g. a 50 Hz capacitive touch screen is only able to reproduce a grating up to 25 Hz. This value corresponds in the spatial domain to a grating of 1 mm period for a finger velocity of 2 mm/s. For texture with a lower spatial period, these performances are not accurate enough.

5.3.2 Texture control

To cope with the problem described in the previous section, in this subsection, the definition of the Texture control is introduced.

A different approach for the texture reproduction is implemented through a synthesis of the haptic signal based on a single period. It has been shown that the interaction of the fingertip with a spatially periodical texture leads to a periodical spatial pattern of the lateral force [108]. Through a synthesis based on the periodic force signal it is possible to avoid the limitations imposed by a low bandwidth position sensor, Fig. 5.6. As Texture control, it is defined a spatial frequency haptic pattern independent on the finger position. The reproduction rate of the identified friction period is determined by the velocity of the finger, which is updated to the new value at each cycle of acquisition (50 Hz).

By implementing this approach, it is possible to reproduce the full bandwidth of a periodical tactile signal with a capacitive touch sensor, due to the continuity of the velocity function for a sampled position. The drawback of this approach is the error in the spatial phase of the signal, and the difference between the measured and real velocity of the finger. This is not problematic for an opaque tactile stimulator, where there is no visual clue given by a screen. However, for a transparent stimulator coupled with a screen, the errors introduced for a low spatial frequency may be easily perceivable

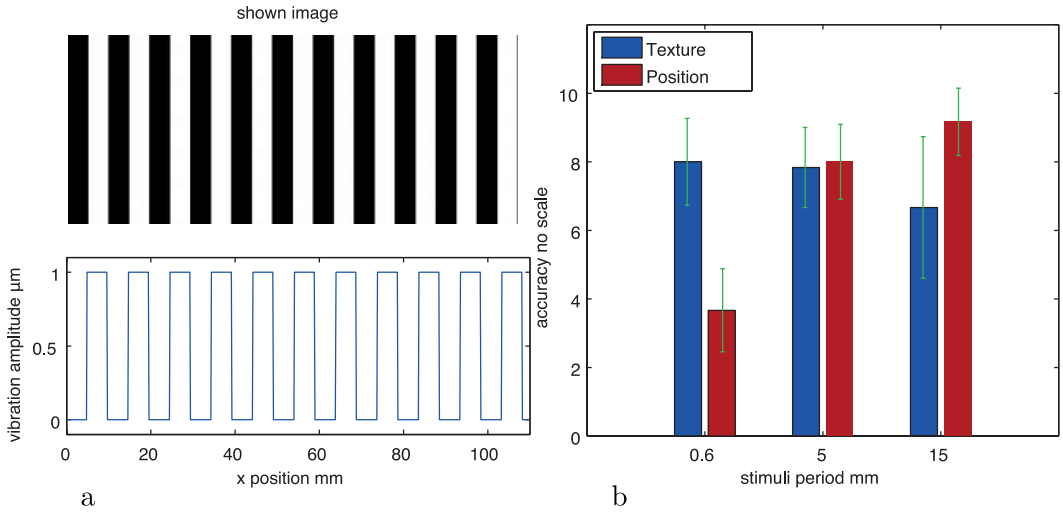

FIGURE 5.7: a, image shown on the screen and associated envelope of the vibration amplitude in function of the x position of the finger. b, given rate of reproduction accuracy for Position control and Texture control

5.3.3 Psychophysical Validation

A psychophysical experiment has been developed to validate the advantages and drawbacks of both the rendering strategies, Position control and Texture control. It was asked to 6 participants, which gave their informed consent, to freely evaluate, with a number from one to ten, the accuracy of reproduction of three different spatialized tactile signals. During the exploration, a visual grating was shown on the screen of the device with the same spatial frequency as the tactile grating, Fig. 5.7. The tactile signals were programmed to provide a friction step change at the interface between black and white line, Fig. 5.7. The participants were free to accustom themselves with the sensation provided by the device with a simple visual and tactile signal in the middle of the screen before the beginning of the experiment. The three analyzed cases were, respectively, composed by a spatial grating of 15, 5 and 0.6 mm, all of them reproduced with both strategies. The signals for each period were presented randomly to the users which were allowed to explore them freely. At the end of each exploration, it was asked to the users to rate, with the number from one to ten, the accuracy of reproduction of the signals. The results are reported in Fig. 5.7. The difference between the control strategies was tested with an unpaired t-test. For the lowest spacing, the Texture control performs significantly better than Position control ($p = 0.0001$). Whereas for the higher spacing Position control performs better than Texture control ($p=0.0232$). No significant difference between the two strategies was found for the intermediate case ($p=0.8$).

5.3.4 Discussion

The approach to the texture simulation on friction control devices is usually based on the comparison of the finger position with a precompiled map of friction. This approach is effective, but the bandwidth of the position sensor determines the maximum reproduction bandwidth of the device. In the case of capacitive touchscreen, this value is in the order of 50 Hz, largely insufficient to reproduce real textures. By defining two different control strategies, the Position control, spatially located, and the Texture control, spatially periodically distributed, it is possible to overcome the limitation of the slow position acquisition. The Texture control approach performs significantly better than the Position control for a large spatial frequency (17 stimuli/cm) resolving the undersampling problem of the finger position. The Position control approach is better than the Texture control for a spatial frequency around 0.7 stimuli/cm where the phase error accumulated by the Texture control becomes noticeable trough visual comparison. No statistical difference was found for the intermediate case. This allows us to propose a spatial frequency boundary between Position control and Texture control, located around 2 stimuli/cm in agreement with the perception separation described in [117].

These results here shown present a fundamental difference to a related experience introduced by Meyer et al. [118]. In the cited work, the interest of the authors was on the identification of the smallest spatial gap impossible to identify by the user as different from the provided noise. The aim of their experience was to highlight the passage from a spatial encoded regime, to a fully vibrational regime.

The present experiment is totally focused on the spatial texture perception provided by periodic signals. In this experiment, the participants were not able to perceive the difference between a spatial signal where the tactile stimulation was provided on the white/black interface or consistently in another spatial phase of the period, postulated that the density of the tactile signal is greater then the finger pad contact area, accordingly with the hypothesis at the basis of the Texture control definition.

The boundary between Position and Texture control placed around a spatial density of 5 mm is understandable by considering that the friction modulation device does not provide a locatable stimulus under the finger pad, but provides a change of the frictional boundary condition of the whole area in contact. The inability to place the stimulus in a determined area of the finger induces the inability to distinguish the spatial phase

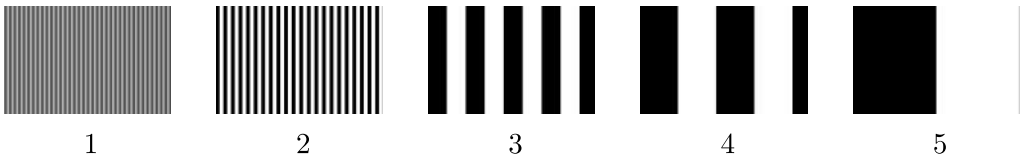

FIGURE 5.8: The 5 visual textures of the 5 tactile feedback numbered from left to right (1-5)

error of the Position control signal when at least two expected stimuli are present under the fingerpad area.

The results confirm that a high bandwidth position recording is not necessary to provide dense spatial stimuli information, assuming that the reproduced spatial signal can be described as a periodic signal. This result is consistent with the work from [117] and does provide a direct experimental proof of the introduced concept.

Speculatively, this result might be interpreted with the duplex theory of texture perception recalled in chapter 1, stating that the coarse textures are encoded by slowly adapting mechanorecepetors, whereas fine tactile sensations are mostly driven by skin vibrations, called vibrotaction, encoded by the rapidly adapting ones. These sensations are not localized, but the interaction with a fine texture produces a determined spatial pattern on the skin, similarly to the Texture control.

In the next section, a broader user study comparing Position control and Texture control will be described to precisely identify the boundary between the two approaches and its dependence on the velocity of exploration of the finger.

5.4 User Study

In this Section a broader user study validating the difference between the two control techniques and exploring the influence of the exploration velocity and the user preference is presented. This work was carried on in collaboration with Yosra Rekik, post-doc researcher from INRIA LNE.

The idea is that the better the quality of the tactile feedback, the more the user is able to match the perceived feedback with a specific texture image. Moreover, it is expected

that the quality of the tactile feedback can be highly related to finger velocity, as well as to the density level of the texture to simulate. More specifically, with respect to the two considered techniques (Position, and Texture), the following hypothesis are introduced:

H1. Faster finger movements cause a decrease in tactile feedback quality.

H2. Texture control provides better (resp. worse) tactile feedback quality than Position control for relatively fast (resp. slow) finger movements.

H3. Denser textures cause a decrease in tactile feedback quality.

H4. Texture control provides better (resp. worse) tactile feedback quality than Position control for relatively dense (resp. sparse) textures.

An experiment is designed to evaluate the proposed hypotheses.

5.4.1 Participants

Ten participants (2 females and 8 males) volunteered to take part into our experiment, their age was between 21 and 31 years (mean=26.33, s.d=3.35).

5.4.2 Method and Apparatus

The E-ViTa device introduced in the previous section is employed for the development of this experiment.

In this study, 5 different periodic tactile signals were either simulated with Texture or Position control. All of them were composed of periodic patterns: extra fine (XF), fine (F), medium (M), large (L) and extra large (XL) periodic patterns, as shown in Fig. 5.8. High friction was associated to black color and low friction was associated to white color. The spatial periodicity of the 5 textures are as follow: 1.2 mm for XF, 5.1 mm for F, 25.5 mm for M, 51 mm for L and 110 mm for XL.

5.4.3 Procedure and Task

The experiment was composed by a training session followed by the data acquisition session. Five visual textures were presented to the participant using paper sheets. Each

visual texture was given a number between 1 and 5. These texture were simulated on E-ViTa and no visual feedback was shown on the tactile surface, and only tactile feedback was provided to the participant. In this manner, it was explored the ability of the participant to recognize a tactile pattern and associate it to an extern visual one.

In the training phase, participants were instructed to move one finger on the interface to feel the tactile feedback. Then, participants were asked to guess which was the visual texture reported on the paper sheet corresponding to the perceived tactile feedback. In this step, participants were instructed to use their preferred finger and to move it at the preferred speed. Overall, each participant completed 10 training trials: five completed with one control technique (eg position) with a randomized order of exposure, then five trials with the other control technique (eg Texture).

In the experiment phase, three factors were covered: the control technique, the finger movement velocity and the tactile feedback signal. The control technique has two controlled levels: Position and Texture. For each control condition, three levels of finger movement velocity were evaluated: slow, moderate and fast. To control the finger movement velocity, its value was shown in real time to the user, and he/she was asked to respect the following boundaries: for the slow condition, participants were instructed to move their finger with a velocity lower than 30 mm/s; for the moderate condition, participants had to proceed faster than 30 mm/s and lower than 180 mm/s; and, for fast condition, participants were instructed to move their finger fastest than 180 mm/s. For the three velocity conditions, participants were instructed to perform as much as possible within the previously mentioned bounds. No time limit was given for the performing of the task. As it will be commented later in the chapter, participants had no trouble fulfilling this requirement. For each velocity condition, and for each of the 5 aforementioned textures, participants were asked to sense the tactile feedback and to guess the corresponding visual texture among those provided in the paper sheets.

Participants' trials were administered as 6 (randomized) blocks of 25 trials each as follows. Under each velocity condition (fast, moderate, slow), the two control technique conditions (Position, Texture) were experimented consecutively, in a random order. For each control technique condition, each tactile feedback texture was experimented five times (25 trials in total). The order of these trials was randomized. Overall, there is a

total of 3 velocity conditions × 2 control conditions × 5 Textures × 5 repetitions = 150 trials for each participant. The average duration of the experiment was 30 minutes.

After each of the 6 experimented blocks (velocity × control), participants were asked to answer the following 5-point Likert-scale questions with possible responses from strongly disagree (1) to strongly agree (5):

- I performed/guessed well
- I needed to concentrate to guess well
- I felt frustrated
- I felt confident in my ability to guess the visual texture
- I enjoyed interacting with the touchscreen

After terminating the trials for each velocity condition, participants were asked to rank the two experimented conditions according to their preferences.

5.4.4 Experimental Analysis

Two dependent variables are investigated, namely, *error rate* and *guess time*. The error rate is defined as the proportion of incorrect answers with respect to a given texture experiment. The guess time is defined as the time that a user takes from starting a trial until entering his response. The error rate provides a sound measure of the quality of the tactile feedback and can be straightforwardly used to inform about the accuracy of the control technique. The guess time is more subjective and can only provide an estimation of how difficult might be the guess for participants.

Dependent variables are analyzed using $2 \times 3 \times 5$ repeated measures within subjects analysis of variance for the factors control {Position and Texture}, velocity {slow, moderate, and fast} and textures {XF, F, M, L, and XL}.

5.4.5 Results

Before starting the analysis of the collected data, it is first checked how well participants performed with respect to the bounds instructed for the finger velocity conditions. All

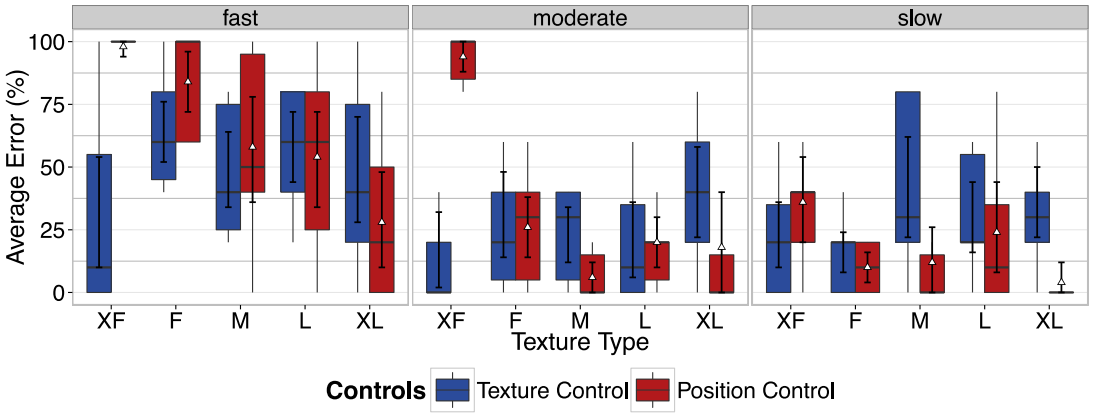

FIGURE 5.9: Distribution of error rate of textures (x-axis). Results are grouped by velocity, (see facet top labels) and by control technique (see legend). Box-plots give median and inter-quantile range.

participants' trials satisfied the required velocity bounds. It was found that in the fast condition, participants moved their finger faster when using Texture control than when using Position control. Wilcoxon Signed-rank test confirmed that this difference was significant ($z = 2.58$, $p < .01$, $r = .25$). This observation suggests that participants were more careful when experimenting Position control using fast finger movements.

In the following, our main findings with respect to the previously described dependent variables are discussed.

5.4.5.1 Error rate

In Fig. 5.9, the different error rates obtained with the two considered control techniques grouped by velocity and as a function of texture type are summarized . To finely analyze our data, a statistical analysis based on repeated-measures ANOVA followed by a post-hoc analysis was conducted. Due to the different interactions revealed by the statistical analysis and the number of factors involved in the experiment. The detailed analysis of the experiment is reported in appendix C.

To summarize the results, the main conclusions of the pre-test are confirmed. Position technique works better for coarse texture, when the stimulus localization is important, and Texture control works better for fine texture. The exploration velocity plays a role for the undersamplig problem, and, as expected, the Texture control works better for fast exploration speed. These results support **H2** and **H4**, and place the boundary

between Position and Texture control between the textures F (5 mm period) and M (25 mm period).

5.4.5.2 Guess time

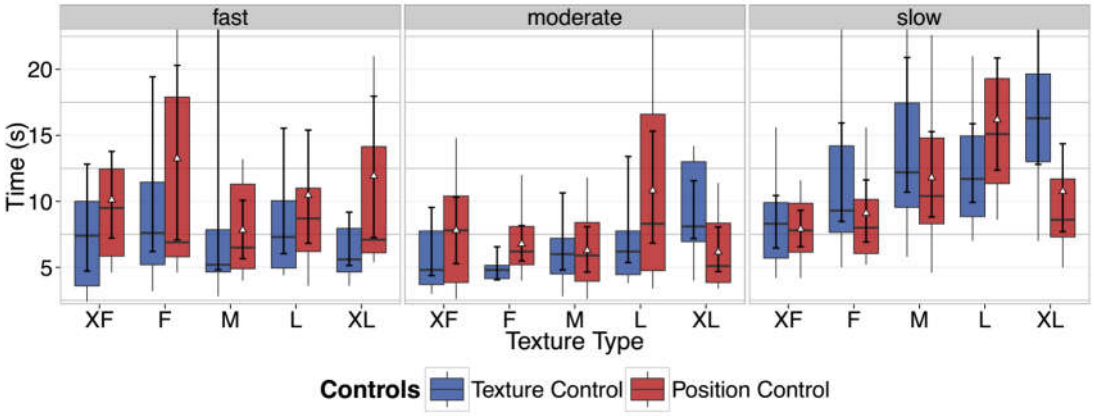

FIGURE 5.10: Distribution of guess time of textures, (x-axis). Results are grouped by velocity, (see facet top labels) and by control technique (see legend).. Box plots give median and inter-quantile range.

In Fig. 5.10, the guess time performance obtained with the two considered control techniques grouped by velocity and as a function of texture type is summarized . Repeated-measures ANOVA revealed a significant main effect of velocity ($F_{2,18} = 9.06$, $p < .001$) on guess time. It may be noted that using moderate velocity induced smaller guess time (mean = 7.48s, s.d = .93s), than fast velocity (mean = 10.31s, s.d. = 1.93s) and slow velocity (mean = 12.22s, s.d = |1.35s). Post-hoc comparisons showed significant differences between moderate velocity and both fast and slow velocities ($p < .05$), but not between fast and slow, thus mitigating **H1**. Importantly, it was found no significant effect of the reproduced signal on guess time suggesting that the time needed to identify a texture is independent from the texture density (mean = 10, s.d = 1.18s), hence mitigating **H3** as well. This is in agreement with a recent study on the kinematic of real texture exploration [28].

5.4.5.3 Subjective results

After each trial of the experiment, participants were asked to rank the control conditions after completing the trial blocks corresponding to each finger movement velocity.

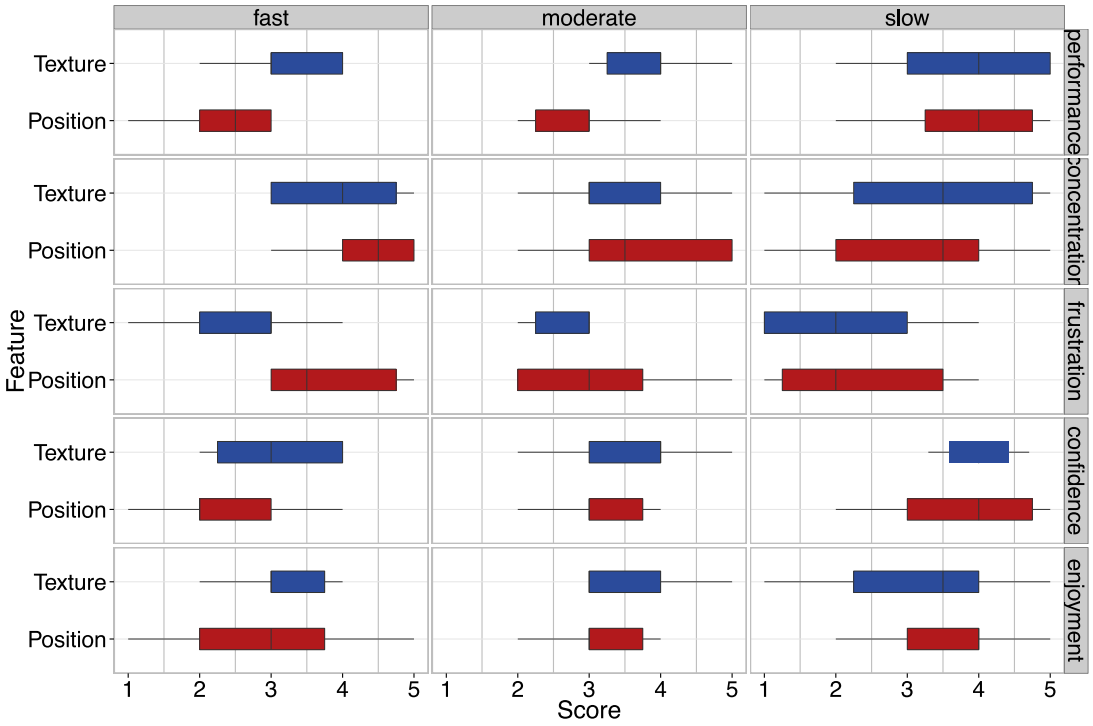

FIGURE 5.11: Distribution of rating scores (x-axis) for subjective questions (see facets right labels). Results are grouped by velocity, (see facets top labels) and by control technique (see legend). Box plots give median and inter-quantile range.

Overall, Texture control was ranked first 100% of the time for fast velocity, 70% of the time for moderate velocity and 40% of the time for slow velocity.

Participants were also asked to rate each control condition. This is summarized in Fig. 5.11. In average, considering all finger velocities, participants found that Texture control was better performing, demands less concentration, implies less frustration, while being more confident and more enjoyable than Position control. However, Wilcoxon Signed-rank tests showed that there were significant differences between the two control conditions only for performance ($z = 2.86$, $p < .01$, $r = .63$) and confidence ($z = 2.44$, $p < .01$, $r = .54$) in fast velocity condition, and for frustration ($z = -2.6$, $p < .01$, $r = .58$) in the moderate velocity condition.

These findings are supported by the participants' comments, some quotes are: "the association of the tactile feedback to its visual representation is easy as the perceived feedback is clearly perceived", "this technique is more faithful to the visual representation", and "I like this technique, the friction is cleanly felt". In contrast, participants felt that Position control reproduced the tactile feedback in a fuzzy way. Some of them

added that they felt that the tactile feedback was not periodically perceived; in particular, for faster finger movements. For instance, for fast velocity some quotes are: “I am unable to differentiate between the textures”, “There are no difference between all the trials”, “There is a mismatch between the visual textures I see and tactile feedback that I perceive”, “I feel confused because for me there is no difference between all the trials... All perceived signal are texture number 5!” and “I feel the same sensations for all the trials, is it normal?”.

It may be noted that Friedman tests revealed that there is no significant effect of finger velocity on each rating score for Texture control. However, for Position control, Friedman tests revealed a significant effect of finger movement velocity on performance rating ($\chi^2(2) = 7.03$, $p < .05$), concentration rating ($\chi^2(2) = 6.93$, $p < .05$) and enjoyment rating ($\chi^2(2) = 7.52$, $p < .05$), with faster velocity inducing a decrease in performance and enjoyment, and an increase in concentration.

5.4.5.4 Conclusion

Given the previous analysis and observations, our key finding is that Position control leads to the lowest level of accuracy for dense Signals. In contrast, Texture control resolved this problem and improved tactile feedback perception significantly for denser tactile feedback textures. On the other hand, Position control is still more accurate for sparser tactile feedback textures where the phase of the tactile signal is associated with the graphical location of the boundaries between different stimuli. In addition, our findings indicate that Texture control improves the tactile feedback quality for high finger movement velocity. In substance, the more refined user study confirmed the results of the pre-experiment, where the boundary between the two control strategy are between the F and M texture.

5.5 Taxtel and Hybrid Control

In order to overcome the limitations of Position and Texture control techniques, a merged control unifying the advantages of both techniques is introduced.

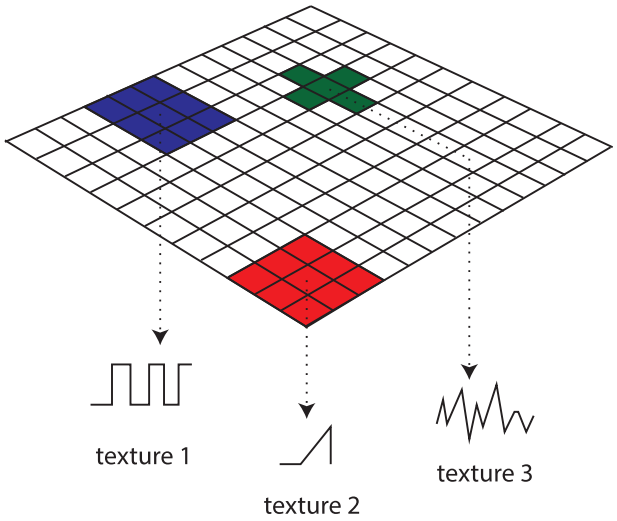

FIGURE 5.12: Representation of Hybrid Reproduction Strategy. Each square on the grid represents one Taxtel with the assigned texture.

5.5.1 Definition

Before introducing the hybrid technique, the smallest period for which the user can perceive the difference between two signals with same spatial period, but different spatial phase, allows us to define the Taxtel, the area unit where the spatial phase of the reproduced signal does not matter.

By separating the tactile rendering in two different processes, one acquiring the finger position and comparing it with a grid of Taxtel (Position control), and the second executing the spatial frictional pattern assigned to this Taxtel (Texture control), Fig. 5.12, it is possible to merge the advantages of both techniques. This division is similar to the one used for the monitors where there is a grid of pixels (Taxtels), the smallest single unit emitting light (Haptic Signals), which is singularly programmed to reproduce a color (texture). As for pixel, the Taxtel is not the smallest dimension where we can detect/perceive a texture (the pixel is not the smallest dimension where we can distinguish a color). However, a set of Taxtels (a set of pixels) can encode a distinguishable texture (color). The assigned texture can be variable or continuous, allowing the implementation of all the gratings previously developed.

Practically, the software handling the tactile reproduction is divided in two separated running processes on the Banana Pi ©, the low level code runs in background and handles the acquisition of the finger position, and the reproduction of the selected texture

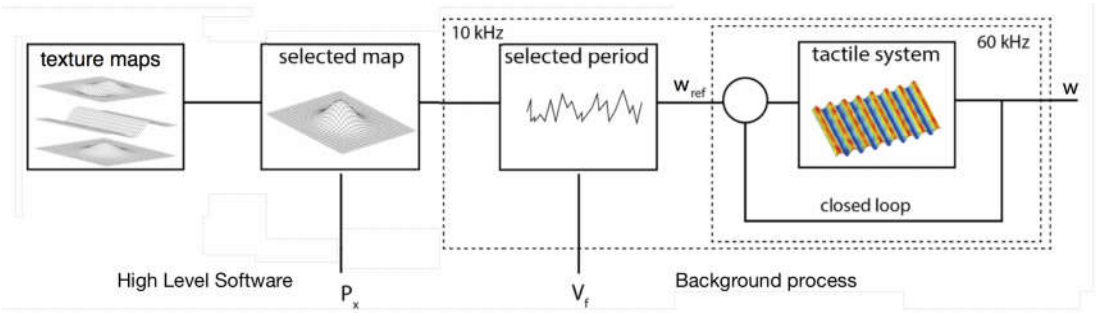

FIGURE 5.13: Representation of Hybrid Reproduction control scheme. The two software separation layer are visible, the high level software handling the interaction with the user, and the background process performing the tactile rendering.

in parallel with the microcontroller in Texture control mode. The high level code communicates with the background process through software communication receiving the finger position and sending the code of the tactile texture to reproduce, in Position control mode. The schema of the control can be seen in Fig. 5.13.

The dimension of the Taxtel defines the resolution of the friction map that has to be encoded. By the pre-experiment, Fig. 5.7, the similar rating of the Position and Texture control given for a spatial grating with 1 cm periodicity sets the bottom boundary of the dimension of the Taxtel as 5 mm, because in one spatial period the tactile stimuli is delivered two times, on the rising and falling of the vibration amplitude. A greater value will be tested in the next experiment to validate this hypothesis.

This makes it possible to keep the accuracy of the spatial division for sparse areas as accurate as the Position control and to leverage the extended range of sensation for greater spatial density signals of the Texture control.

5.5.2 User Study

The Hybrid control technique defined in the previous section is hereby tested. Our goal is to provide users with the extended range of sensation enabled by the Texture control technique while leveraging the spatial accuracy of the Position control technique.

Our first experiment was restricted to simple regular uni-pattern textures. In the second experiment, the effect of two different patterns is investigated. It was chosen to keep the experiment limited to bi-patterns to test the reproduction principle, and to be sure to obtain an accurate information on the Taxtel dimension. Besides, in order to be able to

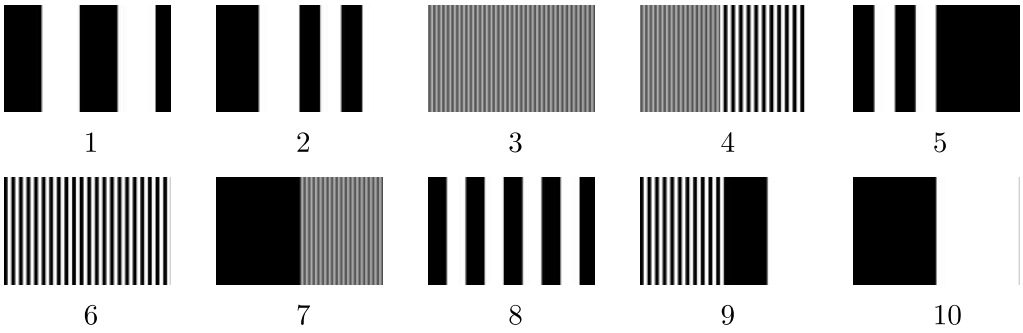

FIGURE 5.14: The set of 10 textures numbered from left to right (1-10) as presented to the participants. Bi-pattern textures representations (2; 4; 5; 7; 9) are the tested textures while uni-pattern textures representations (1; 3; 6; 8; 10) present the distractors.

assess the accuracy of participants' guesses with respect to the perceived feedback, and to remove any noise or randomness in their responses, fake textures were introduced, playing the role of distractors; they were also proposed as possible responses among the provided paper-sheets. 5 textures were haptically represented and 10 textures were shown to the users. All of the distractors were uni-pattern textures, and all of the haptically rendered textures were bi-patterns, Fig. 5.14. The additional 5 distractor textures were all of uni-pattern types, namely, textures number 1, 3, 6, 8, and 10 in Fig. 5.14. This experimental setting is more advanced and allows to remove any noise when evaluating the accuracy of the tactile feedback as perceived by the users. The same experimental procedure as the one depicted in the previous section was used.

Given the output of our first experiment on the relative accuracy of the Texture and Position control techniques, these hypothesis are stated for the Hybrid control technique:

H5. Hybrid control will outperform Position control in error rate for textures mixing at least one dense pattern.

H6. Hybrid control will outperform Position control in error rate for high finger movement velocity.

H7. Textures of dense bi-pattern types (XF-F), will be confused with dense uni-pattern types for Position control.

H8. There will be no significant differences between Hybrid and Position control in guess time.

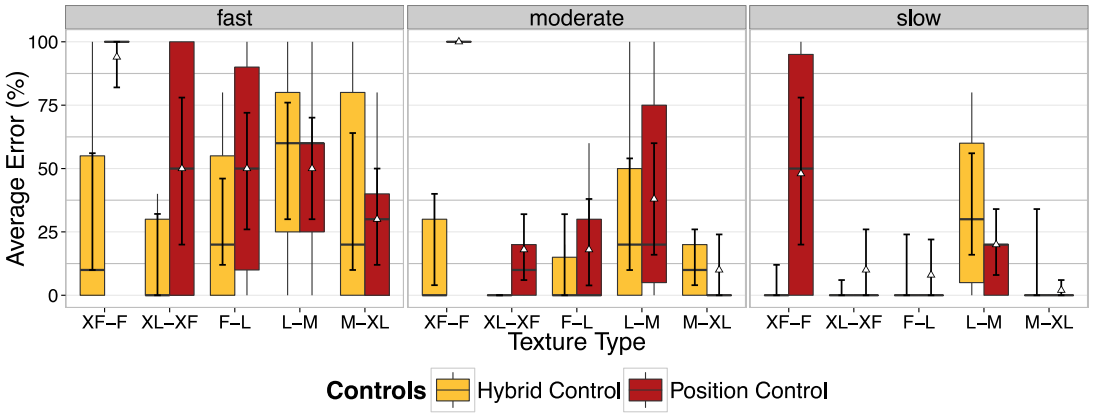

FIGURE 5.15: Distribution of error rate of textures, (x-axis). Results are grouped by velocity, (see facet top labels) and by control technique (see legend). Box plots give median and inter-quantile range.

For this experiment on the Hybrid control, we associated Texture control to XF, F and M textures, while Position control was associated to L and XL textures. With this choice, the dimension of a Taxtel reproduced by the M texture is 12.5 mm, half of the M period.

Ten (10) new participants (two females) volunteered to take part in our experiment. Participants' ages varied between 21 and 32 years (mean age=27, s.d=3.01 years). The dependent measures are the same than for our first experiment, i.e., error rate and guess time. Dependent measures are analyzed using 2 x 3 x 5 repeated measures within-subjects analysis of variance for the factors: control (Position and Hybrid), velocity (slow,moderate, and Fast) and Texture (XL-XF, F-L, L-M, XF-F and M-XL). In the following, the results are presented.

5.5.3 Error rate

Fig. 5.15 shows the distribution of error rate for the two control techniques grouped by velocity, and texture. Repeated-measures ANOVA revealed significant main effects of control ($F_{1,9} = 8.57$, $p < .01$), velocity ($F_{2,18} = 12.54$, $p < .0001$), textures ($F_{4,36} = 14.19$, $p < .0001$) on error rate. Post-hoc tests revealed that Hybrid control improved significantly ($p < .0001$) the accuracy rate by 44% compared to Position control. In addition, it was found that there was a significant control $\times$ textures ($F_{4,36} = 28.18$, $p < .0001$) interaction. Post-hoc tests revealed that error rate was significantly lower for Hybrid control than for Position control ($p < .00001$) for texture types XF-F and

Perceived Texture

Actual Texture	XF-F	XL-XF	F-L	L-M	M-XL	XF	F	M	L	XL
XF-F	82.0	0.0	0.7	0.0	0.0	12.0	4.7	0.7	0.0	0.0
XL-XF	2.0	94.0	0.7	0.0	0.0	2.0	1.3	0.0	0.0	0.0
F-L	4.7	0.7	83.3	4.0	0.7	0.7	2.0	3.3	0.7	0.0
L-M	0.0	0.7	2.7	60.0	2.7	0.7	2.7	13.3	17.3	0.0
M-XL	0.0	1.3	4.7	3.3	78.7	0.0	0.0	0.7	2.0	9.3

Perceived Texture

Actual Texture	XF-F	XL-XF	F-L	L-M	M-XL	XF	F	M	L	XL
XF-F	19.3	0.0	6.0	3.3	1.3	10.7	36.7	21.3	0.7	0.7
XL-XF	0.7	74.0	0.7	13.3	0.7	0.0	0.0	0.7	2.7	7.3
F-L	1.3	0.0	74.7	4.0	1.3	0.0	4.0	8.7	5.3	0.7
L-M	0.0	7.3	2.7	64.0	1.3	0.0	1.3	10.7	11.3	1.3
M-XL	0.7	0.7	5.3	1.3	86.0	0.0	0.0	1.3	2.0	2.7

TABLE 5.1: Confusion matrices for Hybrid (top) and Position (bottom) controls for the textures condition. Cell values show percentages of associations between actual and perceived textures.

XL-XF ($p < .05$). These results support **H5**. Moreover, we found that there was no significant control × velocity interaction (p=.07), suggesting that the benefits of Hybrid control are consistent across the different velocities, and hence, supporting partially **H6**.

A confusion matrix is an useful tool to resume the performances of the two techniques, in Table 5.1. Each cell of the table corresponds to the average of times a participant's response with respect to the pattern depicted in the row was equal to the pattern depicted in the column over all velocity conditions.

The analysis of confusion matrices shows that dense bi-patterns texture (XF-F) was often confused in the case of Position control with a uni-pattern texture, namely in 68.7% in average over all guesses (36.7% with F, 21.3% with M and 10.7% with XF). In contrast, it was confused in only 12% of the time with XF in the case Hybrid control. These results support **H7**. It was also found that the XL-XF texture is 13.3% of the time confused with L-M when using Position control, while it is seemingly not confused when using Hybrid control. Finally, it was found that the L-M texture was confused with the M texture and the L texture, 10.7% and 11.3% of the time respectively when

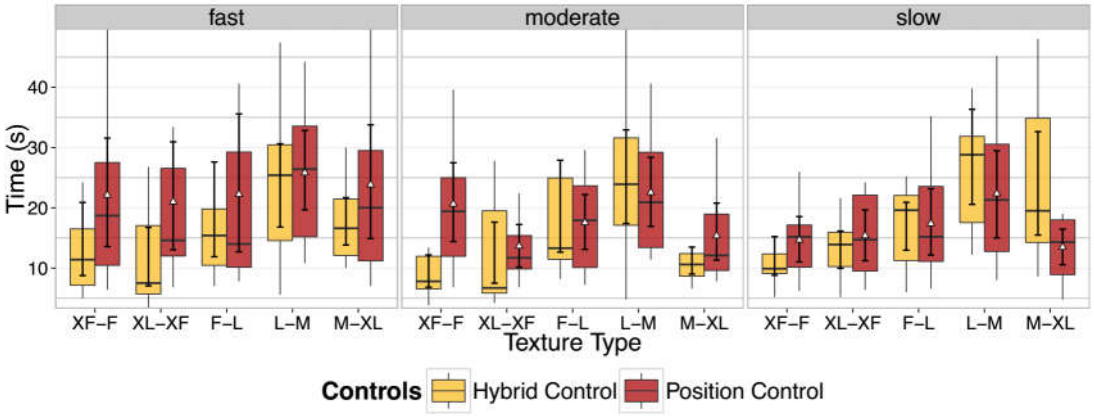

FIGURE 5.16: Distribution of guess time of textures, (x-axis). Results are grouped by velocity, (see facet top labels) and by control technique (see legend). Box plots give median and inter-quantile range.

using Position control, while it was confused by 13.3% and 17.3% of the time respectively when using Hybrid Control.

This does confirm that the dimension of the Taxtel, and following, the boundary between Position and Hybrid control is in between the 12.5 mm distance of the stimuli found in this experiment and the 5 mm distance obtained in the pre-experiment.

5.5.4 Guess time

Repeated-measures ANOVA revealed a significant main effect of textures ($F_{4,36} = 15.11$, $p < .0001$) on guess time, with significant control × velocity ($F_{2,18} = 5.77$, $p < .01$) and control × textures ($F_{4,36} = 3.863$, $p < .01$) interaction. It was found that XL-XF texture took the lowest time to be recognized (mean = 14.47, s.d = 2.40s), followed by XF-F (mean = 15.42, s.d = 2.64s), then M-XL (mean = 17.58, s.d = 2.78s), then F-L (mean = 18.65, s.d = 3.05s), and finally L-M (mean = 24.56, s.d = 2.98s). Post-hoc tests revealed that there were significant differences between L-M and the four other textures (*i.e.*, XF-F or XL-XF or F-L or M-XL). Importantly, it was not found a significant main effect of control on guess time, supporting **H8**.

5.5.5 Subjective results

Hybrid control was ranked first 100% of the time for both fast and moderate velocities, and first 80% of the time for slow velocity.

As for rating, for all finger velocities, participants found that Hybrid control is more accurate, demands less concentration, implies less frustration, while being more confident and more enjoyable than Position control. Wilcoxon Signed-rank tests show that there is a significant difference between the two control conditions for performance ($z = 2.92$, $p < .01$, $r = .65$), frustration ($z = -2.40$, $p < .05$, $r = .53$), and confidence ($z = 2.60$, $p < .05$, $r = .58$) for fast velocity, and for concentration ($z = 1.41$, $p < .05$, $r = .31$) and enjoyment ($z = -1.41$, $p < .05$, $r = .31$) for slow velocity.

Friedman tests revealed that no significant effect of finger movement velocity on each rating score for Hybrid control can be reported. However, for Position control, Friedman tests revealed a significant effect of finger movement velocity on performance rating ($\chi^2(2) = 8.85$, $p < .01$), frustration rating ($\chi^2(2) = 8.58$, $p < .01$) and confidence rating ($\chi^2(2) = 8.66$, $p < .01$), with faster velocity inducing a decrease in performance and confidence and an increase in frustration.

Finally, participants also found that Hybrid control provided them with a clear tactile feedback faithful to the visual texture representation, while Position control is described as less faithful to the visual representation.

5.5.6 Methodology for identifying the textures

To better understand how participants were performing, the different strategies elaborated by participants in order to associate the tactile feedback with a given texture are reported here-after ; it is possible to state the following:

- **Determining the number of pattern types in the texture.** Most of the participants first try to figure out how many pattern types they are able to perceive. For this purpose, three main strategies are used: (1) Most participants move their finger in one direction, e.g. west-east, and then the opposite direction, e.g. east-west, in order to determine if they "feel the same sensation or not", (2) some participants move their finger many times in the middle of the screen trying to "detect a change in the pattern type", and (3) some participants explored many times the right half of the texture then the left half (or inversely) to determine whether it "holds the same pattern type" or not. If the texture is judged as

containing two pattern types, then participants divide the surface in two subspaces and explored each one separately using the next strategies.

- **Counting the number of all tactile feedbacks.** Most of the participants count the number of all tactile feedbacks, and then try to match the tactile feedback distance with the visual texture represented on the paper.
- **Searching the larger and thinner texture patterns.** While most participants use a counting methodology to correctly identify a texture, some notice that, in addition, "sparser and denser pattern types are helpful to classify the texture" by eliminating the textures that do not correspond those patterns.
- **Making small finger movements.** One participant explored the tactile surface by making small finger movements in both directions arguing that this "enables to identify more quickly the actual texture".

5.5.7 Conclusion

The performed user study confirmed that a merged control strategy can obtain the same performances of the Position control for sparse textures, and the Texture control for dense textures. It was possible to obtain this result with the introduction of the taxtel concept and the separation of the rendering software layers.

5.6 Conclusion

In this chapter, the development of the E-ViTa device is described and the techniques to efficiently render dense tactile signals are introduced. The device is based on off-the-shelves low-cost components equipped with custom firmware on the microcontroller. It was designed to synthesize a vibration amplitude signal of 500 Hz with at least 20 points for period, ensuring a low distortion of the control signal of the vibration amplitude. A reproduction bandwidth of 400 Hz was obtained thanks to a closed loop control of the vibration amplitude of the device, and the importance of a broad band of reproduction was proven thanks to a psychophysical experiment. It was shown that the user is able to perceive the difference between a step with a maximal harmonic content of 175 Hz and a signal with an harmonic content of 800 Hz.

In the following, two different haptic signal strategies are formalized: Position and Texture control. The former, is the classic approach for haptic signal rendering based on the comparison of the finger position with a precompiled map of friction. The latter relies on the assumption that the interaction with texture generates a periodical stimulation. By posing this hypothesis, it was possible to define a single period of the stimulation and reproducing it in function of the finger velocity, to generate a spatial integration of the signal. The difference between the two approaches has to be searched in the spatial phase of the tactile signal, which is constant for the Texture control and dependent on the first contact position for the Position control. A preliminary experiment validating the ability of the user to match a visually represented texture with the reproduced signal for both of the techniques suggested that the spatial phase of the signal is not a useful information when the density of stimulation is greater than the fingerpad contact area for surface haptic devices. A broader user study analyzing the user preferences and performance in a similar task was developed for 5 textures. The results are aligned with the pre-experiment, confirming the better accuracy of the Texture control when fine patterns are represented, especially for great finger velocity, and the superiority of Position control when the objects are sparse.

Finally, the concept of the Taxtel, the largest area where the spatial phase of the signal does not matter, and a Hybrid control technique are proposed and tested with a similar experiment certifying the merging of the advantages of the both techniques in a unique general reproduction strategy.

Related pubblicatons to this chapter are:

- E.Vezzoli, T. Sednaoui, M. Amberg, F. Giraud and B. Lemaire-Semail. Control Strategies for Texture Rendering with a Capacitive Based Visual-Haptic High Fidelity Friction Control Device, Eurohaptics 2016.
- T. Sednaoui, E. Vezzoli, D. Gueorguiev, C. Chappaz and B. Lemaire-Semail, Psychophysical Power Optimization of Friction Modulation Tactile Interfaces, Eurohaptics 2016.

Chapter 6

Conclusion and Prospectives

6.1 Conclusion

This work aimed to propose a refined modeling for both surface haptic techniques, ultrasonic vibrations and electrovibration, to develop a novel tactile device taking advantage of the perceptual properties of the tactile sense, and to propose control strategies for texture rendering.

Initially, the characteristics of the human sensing were outlined with a focus on the mechanisms behind the tactile encoding. The state of the art of the knowledge of texture perception is described with the introduction of the *duplex theory of tactile sensing*, dividing the perception of fine signals induced by skin vibrations, and coarse signals induced by skin indentation. The anatomical and mechanical characteristics of the finger pad and the skin were introduced, as well as the influence of these characteristics on the interaction with objects. The finger pad friction was analyzed thanks to of the summary of the latest works for its relevant role on the surface haptic techniques involving the modification of the sliding friction. This introduction posed the theoretical basis for the understanding of the tactile sensing in humans, and allowed the development of the hypothesis and strategies outlined in the contribution chapters of the thesis.

The classical explanation of the friction reduction in ultrasonic device, namely the *squeeze film* effect, was tested with different experimental setups. It was concluded that its participation to the reduction of friction in ultrasonic device is, at least, partial. A mechanical exploration of the contact dynamics between the finger and the ultrasonic

vibrating plate showed that the intermittent contact is the dominant mechanism for the friction modulation associated with ultrasonic displays. It appears when the vibrational amplitude is greater than the corresponding unloading displacement of the fingerprint ridges. It occurs because the viscoelastic retardation time of the finger pad is much longer than the timescale of ultrasonic vibrations, and thus it is reasonable to assume that deformation is limited to the more elastic fingerprint ridges. The mechanism is relatively complex and does not involve only a reduction in the total contact time since it has been shown that a normal force balance is maintained under high frequency vibration. At one vibration period timescale, the phenomenon happens because the periodic contact of the vibrating plate occurs at maximum acceleration so that the resulting instantaneous maximum reaction force is greater than that of the applied normal force. When such a contact is formed, the fingerprint ridges deform laterally due to the exploration of the fingertip, which causes a gradual increase in the perceived frictional force until inducing slip, which corresponds to the Coulomb's law, that is the product of the coefficient of friction without vibration and the instantaneous normal reaction force. Thus, the integral mean frictional force will be less than that which would be perceived if there was no loss in contact. The friction modulation of ultrasonic displays may be ascribed to a ratchet mechanism since the lateral displacement of a finger pad involves recurrent engagement and subsequent escape from the display. This mechanism predicts multiples dependencies of the reduced friction with finger material parameters, applied force, vibrational frequency, exploratory velocity, and coefficient of friction. A first order data superposition was proposed by the developing of a dimensionless group able to summarize the contribution of each parameter. An experimental validation of the developed model was performed through a tribology assessment with a custom developed probe, and a finger pad, confirming the validity of the developed approach. Moreover, the modelling suggests that a greater friction modulation effect, and a greater sensation stability across users, would be achieved by increasing the vibrational frequency of the ultrasonic device.

Electrovibration technique is the second available technique to modify the user perception of a surface, it increases the friction between the finger and the plate covered by an insulator with the application of a high voltage. Both of the static electrical models of the phenomenon proposed in bibliography were evaluated with the comparison of the predicted values of normal force increase with literature data; one of which was

discarded for the inability to predict experimental data, and theoretical imprecision. The chosen model was implemented in an anatomically inspired finite element model of the finger with infinite capacitors assumption due to the symmetry of the geometry. An experimental assessment with a direct measurement of the attraction force without contact was used to validate the developed model. The influence of the air film and the finger geometry were certified: they account for the 20 % of the attraction force during light touch exploration. The the study continued with the contact condition analysis. Previously performed tribological assessment showed a decreasing of the lateral friction force following the application of a step function of voltage, which is not predicted by the literature model, for this reason, an analysis of the charge dynamics between the finger and the plate was performed. It was possible to predict the dynamic of the charges and the frequency behavior of the induced friction modulation by including the non-linear electrical properties of the *stratum corneum* in function of the frequency in the developed model. This more reliable electrical modeling of the electrostatic phenomenon can help for the design of more efficient electrostatic devices.

Both of the presented techniques were proven independent in the physical and the perceptual domains by the development of a coupled device able to reduce the friction with the ultrasonic vibrations and increase the friction by the application of a voltage. The static compensation of the friction signals as well as the similar dynamics were proven by tribological assessment. A psychophysical experiment certifying that the human perception of the techniques is similar suggests that all the perception results found valid for one technique may be assumed valid for the other.

Finally, a novel ultrasonic device, called E-ViTa, was developed taking into consideration the design rules suggested by the modeling of the interaction between the finger and the plate, as well as the perception characteristics of the human tactile sense. It features a commercially available screen coupled with a capacitive position sensor. A new algorithm for the reproduction of spatially periodical signal was developed accounting to the *duplex theory of tactile sensing*. It is shown that the absence of localized stimuli under the fingertip leads to the illusion to touch localized periodical pattern even for a non-localized periodic haptic signal. This is proven when the density of the stimuli is comparable with the human fingertip contact area, which is probably due to the encoding of coarse surface haptic texture as vibrotaction stimulation. The developed concept allowed the relaxation of the necessary bandwidth of the finger detection sensor to reproduce fine textures. A

broad user study comparing the performances of the new algorithm with the classic one is performed, certifying its superior ability to reproduce dense textures. Following, an hybrid technique joining the advantages of both introduced control schemes is developed with the concept of Taxtel, defined as the largest area where the user can not distinguish a spatially phase locked signal from a random one.

In summary, this work provides a deeper understanding of the surface haptic techniques and may help for the design of future devices and tactile signal.

6.2 Prospectives

Vibration Pattern Rendering Till present, the approach to render real texture on a haptic surface was based on the reproduction of the friction profile. However, due to its mechanical properties, the finger tends to filter the relation between the fine surface geometry and the measured friction force. To overcome this problematic, it would be better to implement a control scheme of the system tuning the induced vibration pattern on the skin of the finger. By this mean, it might be possible to reconstruct the vibrotaction spectrum of the tactile signal, achieving a greater rendering accuracy.

Optimized Coupled Device The development of more precise physical models of both surface haptic techniques, and the experimental proof of their independence, may allow to develop an optimized coupled device exploiting the predicted optimization of the performances. In particular the material properties of the insulator should be better designed. Moreover, to obtain a linear stimulation along all the rendering capabilities of the device, the dynamic of both effects needs to be matched, otherwise the user may easily perceive the mismatch between the rendering bandwidth of both techniques, as shown in chapter 5.

Tactile Information In the last chapter, the ability of the user to match the visual representation of a texture with its tactile rendering may allow to implement a transition between a simple stimulation performed by tactile device, to a not boolean information delivery. Till now, haptic signal in surface haptic devices were employed to enrich the

user experience, but the possibility to deliver a piece of information, instead of just a stimulation, may open new cases of application.

In order to obtain this transition, a precise categorization of the number of distinguishable textures that the surface haptic device can reproduce is necessary. This experience may identify the number of bit of information that the haptic interface can deliver, allowing the implementation of user cases exploiting this advantage.

Texture Representation Standard and Haptic Card A possible theoretical proposition of a parametric standard to encode tactile signals is here reported.

By defining the Hybrid control, it was possible to merge the advantages of the positional accuracy of represented localized objects and the high spatial density pattern information of dense surfaces. The definition of a periodic spatial pattern associated to dense tactile signals may allow to introduce a more efficient representation of the signals.

The perception of the vision and auditory sense is provided by the division of the perceived signal in a given number of channels that are singularly encoded, i.e. cone cells in vision are responsible of the light perception in the eyes are divided in three big families responsible for the detection of the blue, green and red color. These perceptual characteristics are responsible for the use of the three colored light emitters in each pixel of our computer, smarthphone or tablet monitor. It is also at the basis of the well know RGB standard for pixel color encoding.

As described in the introduction, the encoding of the tactile signal is slightly different, due to the different families of information that it encodes: spatial, geometrical and temporal, which complicates the texture encoding task. While these characteristics are generally true, the results shown in the last chapter may allow to implement an encoding standard valid for surface haptic signals. By proving that the spatial pattern of the haptic signal matters for the texture encoding when the object density is greater than the contact area of the fingerpad, the necessity of an accurate spatial definition may be relaxed.

From functional analysis, each continuous signal may be represented as a superimposition of orthogonal functions with a determined amplitude coefficient and a phase. For

periodic signals, it is possible to implement an efficient representation based on a sinusoidal superimposition of functions. The Texture control is based on a single spatial period that is reproduced, it is then possible to implement the encoding of the spatial period, not as a precompiled table of values, but as a set frequency, amplitude, and phase parameters describing its evolution. An algorithm performing the reconstruction of the signal based on a single sinusoid period is sufficient to reconstruct the information.

The identification of the number of channels necessary to encode without perceivable loss between the continuous signal and the reproduced one is necessary to identify bandwidth separation between the modes. The structure of the E-ViTa device is ready to implement the experiment and prove the concept, which will be performed in the near future.

The plausible outcome of the standard may be N triplets of parameters (frequency, amplitude, relative phase) defining the texture for a determined Taxtel.

By implementing this procedure in an extern piece of hardware, a first generic tactile card handling all the process of tactile reproduction for surface haptic device may be implemented. It would handle both spatial and temporal signals with the high spatial accuracy of the Texture control, and the only pieces of information required by the card would be the velocity of the finger and the spatial or temporal parameters of the signal to reproduce.

Appendix A

Mechanoreceptors Friction Encoding

In this appendix, the description of the study currently performed at Goteborg University in Sweden with one ultrasonic device produced in the lab is outlined.

The specific role of friction has not been considerably explored in human neurophysiology compared to textures or vibration. A series of studies addressed the issues of detection of the slip of an object gripped by the fingers [119, 120], or shearing of the finger tips in different directions caused by a load with high friction [121]. One problem is that differences in friction between natural surfaces normally also implies variations in texture. Hence, it has been impossible or very difficult to study the specific role of friction in mechanoreceptor coding the properties of dynamic tactile stimuli, such as when the finger tips are sliding over a surface. In the present study, our aim is to determine how a pure modulation of friction is coded by the four classes of tactile mechanoreceptors. This can be achieved by an ultrasonic device, since the controlled ultrasonic vibrations of that device cause a change in friction while the texture of the surface remains constant. The ultrasonic vibrations themselves cannot be detected by low-threshold mechanoreceptors. Hence, the role of friction for mechanoreceptor coding of tactile events can be studied in isolation in a way that has not been possible before. The coding of the changes in friction caused by the ultrasonic device is also important from the point of view of benchmarking new Tactile Display technology, where the end goal is to mimic natural tactile sensations during exploration of a flat surface. Here, we

report the successful adaptation and integration of an ultrasonic device to the conditions of microneurography in human volunteer participants, and the results from the first experiments.

Methods Participants and Units. Four human volunteers took part in the study from which we recorded the nerve activity of 2 single unit afferents (1 SA1, 1 FA2). They were recruited at the campus of the University of Gothenburg and were paid for their participation. The microneurography and the stimulation were conducted in their left arm and hand respectively on the left median nerve. All participants received an information letter, and provided written informed consent according to the declaration of Helsinki.

Material Within the PROTOTOUCH project, the ultrasonic device was designed in order to adapt to the constraints of the microneurography procedure, figure A.1. It features a closed loop control system of the vibration amplitude up to 1.2 µm with a bandwith up to 250 Hz. As such, the device was placed on a custom-built robot platform, which provides the means to passively stimulate the participant's finger. Normal and tangential forces were measured with a 6-axis load cell (ATI Industrial Automation, Apex,. NC, USA). The robot slides the ultrasonic device surface over the finger with a constant speed of 20 mm/s, while applying a normal force of 0.4 N. The robot was also oriented in order to match the receptive field of the unit tested. A tri-axial accelerometer was placed on the participant's finger in order to measure high-frequency vibrations, and to control for the presence of mechanical resonance during the stimulation. All data were sampled at 16000 Hz using Spike2 software (Cambridge Electronic Design, Ltd., Cambridge UK).

Protocols Four independent protocols were designed to investigate how the single unit afferents respond to friction and friction modulation. In the first protocol (P1), there was a step change in friction, from the base friction caused by the surface of the device when it was inactive (ultrasonic vibration amplitude equal to zero), to another friction value. Three distinct amplitudes of vibration were tested (200, 750 and 1200 nm). In P2, the friction was modulated by an alternating fast increase/decrease in vibrational amplitude in order to simulate stimulation by natural, grating-like, textures.

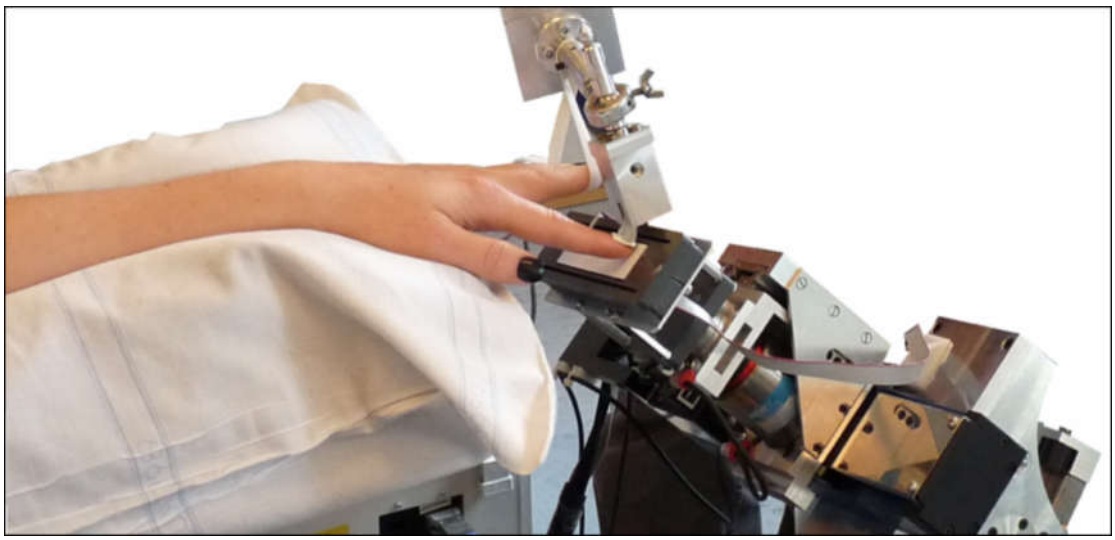

FIGURE A.1: An adapted ultrasonic device mounted on the tactile robot platform. The figure also shows the finger holder attached to the nail of the index finger. The tip of the finger is brought in contact with the ultrasonic device by the robot

Five simulated gratings were used, with spatial periods of 1600, 800, 400, 200 and 100 µm. (This corresponds to tactile fundamental frequencies of 12.5, 25, 50, 100, and 200 Hz, since the ultrasonic device was sliding at 20 mm/s.) In P3, we manipulated the rise time, which is the time taken by the device to reach a given amplitude. This manipulation affects the sensation of sharpness associated with a change in friction. In P4, we manipulated the mean level of friction of the device, which was maintained constant. Three levels were tested: 200, 750 and 1200 nm. The four protocols used are illustrated schematically in figure A.2. Before starting the microneurography procedure testing, a familiarisation trial was provided with the four stimulation protocols being executed on the index finger of the participant. The protocols were displayed according to a priority order, with P1 being displayed first, followed by P2, etc. This procedure was used to optimise the data collection; with more protocols being tested the longer the duration of the recording. For each protocol, the stimulations were completely randomised, delivered in two directions (ulnar or radial), and repeated six times.

Preliminary Results Illustrative results from two single unit afferents are illustrated in figure A.3. For these units, only P1 was tested. The results obtained for an FA2 (Pacinian Corpuscle) type unit are presented on the left panel. The results from an SA1 type unit are presented in the right panel. These results illustrate that following an increase in vibration amplitude (top panels), there is a reduction in friction, here

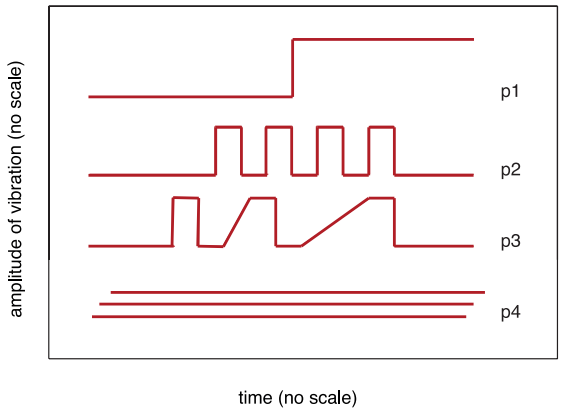

FIGURE A.2: Schematic illustration of the four experimental protocols: P1, step change in friction; P2, simulated grating; P3, change in the rise time of the friction change; P4 constant friction at three different levels. See text for details.

measured as a change in the lateral force (since the normal force is constant; see the middle panels). The bottom panels show the raw nerve recordings. Figure 2 shows that the FA2 responds transiently at the step change in friction, here with a single nerve discharge near 0.6 s (bottom left panel). The FA2 unit also responds transiently when the load is applied at the start of the trial, and when it is removed at the end, reflecting the fast adaptation and high dynamic sensitivity of this type of mechanoreceptor. The SA1 shows a sustained response during the full sliding phase, which reflects the slow adaptation of the unit, and the coding of the applied forces. However, there is a reduction in the overall firing rate after the reduction in friction to the right, tentatively indicating that this SA1 unit encodes normal as well as the tangential force. Hence, there appears to be a role also for SA1 units in the encoding of friction, and coding of simulated "edges" by the ultrasonic device.

Conclusion The data presented in this report serves to illustrate the successful application and use of the ultrasonic device during actual microneurographic recording of the activity of single, identified mechanoreceptors in human participants. Data collection is ongoing, but already the preliminary data show that pure changes in friction, without concomitant change in the texture or other properties of the surface touching the skin, can elicit mechanoreceptor responses that appear to mimic those caused by a naturally occurring tactile event. This includes FA receptor detection of an edge, and SA coding of the magnitude and direction of tangential as well as normal forces.

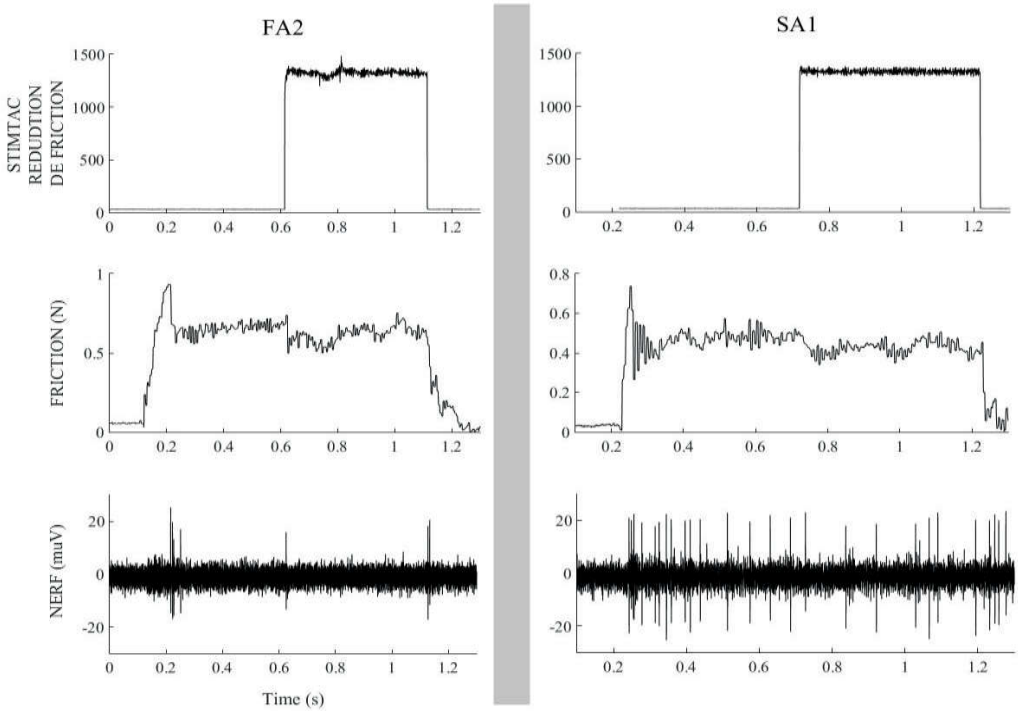

FIGURE A.3: Illustration of the results obtained

Appendix B

Limits of Friction Perception and Encoding of Active and Passive Touch

In this appendix, a brief description of the two experiment conducted with the ultrasonic device provided to the neuroscience departement of the Universite Catholique de Louvain is reported.

B.1 Frictional Perception Limits

Materials A specific tactile stimulator controlled in amplitude has been designed to provide an extremely low friction-time response and a 250 Hz reproduction bandwidth, to cover the perceptual range of the human finger. The compact stimulator has been designed to be mounted on the robot for tactile studies. Moreover, the implementation of a slave mode via BNC connection, and the communication of the measured vibrational amplitude via a BNC connector have been performed, to provide an easily control method for the device, figure B.1.

Protocol The friction perception experiment aim was to determine the capacity to perceive differences in of the amount of friction reduction. From this psychometric function it was then possible to extract the just noticeable difference (JND) of signal duration

for humans interacting with the ultrasonic vibrating tactile device. The experiment was based on a forced choice task with a constant pool of stimuli (constant stimuli method). The participants had to compare the length of two stimuli, displayed in sequential order. A reference value of the null signal was always randomly set as one of the two stimuli presented in the discrimination task. The other stimulus was a test value to compare against the baseline. Three different surfaces were evaluated to test the influence of hydrophobic/hydrophilic material properties on the reduction of friction. 11 participants were tested with the current protocol.

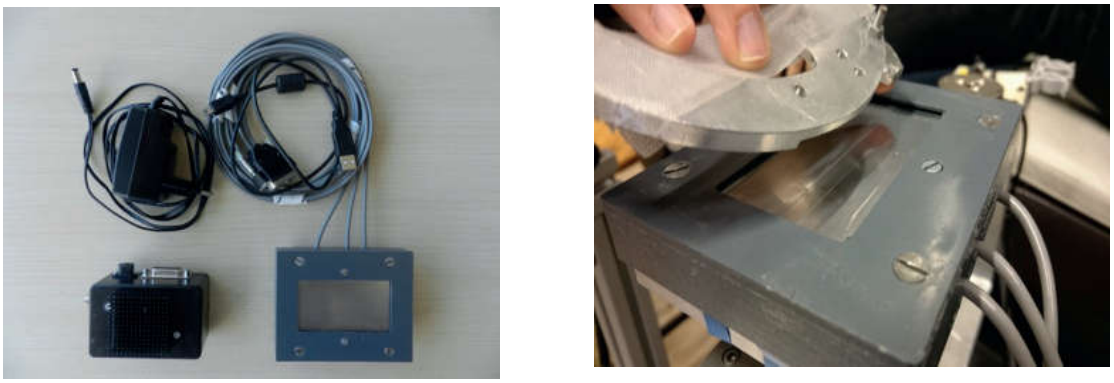

a b

FIGURE B.1: a, provided ultrasonic device, and b the device mounted on the evaluation robot

Results It was found that the absolute reduction of the tangential force depended on the natural friction coefficient of the material. However, the relative reduction of the tangential force was similar for the three tested screens, which were made from different materials. Thus, it seems that the screen material does not influence the perception of the modulation of friction and the quality of haptic feedback. This is in accord with the modeling presented in chapter 2. A psychphysical evaluation of the threshold of perception of the relative friction changing is stable between the different material, and it assumes the value of 8 %, suggesting that humans are sensible to the relative friction change, figure B.2.

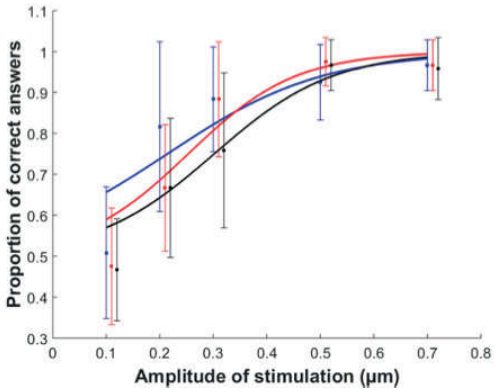

FIGURE B.2: Psychometric curves and corresponding error bars for screen surfaces made of aluminium (blue), polypropylene (red) and polyurethane (black) fitted to the proportion of correct answers for each of the tested amplitudes of ultrasonic vibration. The error bars are slightly shifted for better visibility.

B.2 Neurofisionlogy of Active and Passive Touch

This part in the project aims to study the neurophysiological mechanisms underlying the sense of touch, regarding the central nervous system. More precisely, the project is focused on exploring actively and passively textured surfaces using electroencephalography (EEG) and more specifically a novel approach based on the recording of Steady-State Evoked potentials (SS-EPs) in order to study non-invasively touch perception in humans. To date, experiments have been conducted to obtain an insight into the way people perceive periodic textures (i.e. gratings) in passive touch in order to study in depth the perception of textures. The results indicate that humans perceive differently textures depending on their spatial characteristics. Characterizing the cortical activity of textures can be challenging, so, in order to address this difficulty, the approach that has been used thus far is presenting the stimuli in passive touch in order to have better control of the experimental parameters. The purpose of the first testing of the device was to explore whether it is possible find in the EEG signal the brain responses related to the exploration of the tactile device.

Material The same ultrasonic device presented in the previous section was employed for this study.

Methods To perform the experiment it was used the Steady-State Evoked potentials (SS-EPs) approach. SS-EPs are elicited by the periodic modulation of a stimulus feature,

identified in the frequency domain as peaks appearing at the frequency of the repeated stimulus. The vibrational amplitude was modulated at a frequency of 11 Hz with a square wave modulation to elicit both low frequency and harmonics stimulation. The tactile device evaluation consisted of two parts. Initially, participants were recruited to explore the device by scanning their index fingertip across the plate in active touch and then comparing their performance in passive touch. To reproduce the same force applied and movement pattern, the position of the finger and the its force applied were recorded during the active touch phase and reproduced with the robot in the passive touch experiment. The reproducibility of the active touch exploratory condition was in this way achieved [122].

Results Frequency analysis showed that the chosen evaluation method was suitable. Indeed, we observed that consistent brain responses were elicited when participants explored the display. This result also supports the choice of SS-EPs as a valid method in response to sensory stimulation. The results highlight that the sensation provided by the tested ultrasonic device was constant in both conditions (active and passive touch) and, importantly, the participants' attention did not depend on the exploration method (active or passive). A particularly interesting results is the different response of the SS-EPs for the 22 Hz stimulation. By referring of Appendix A, it is straightforward to understand that the fast adapting mechanoreceptors encode the change in friction, which, for a squared wave modulation happens 2 times for period. Speculatively it is possible to suggest a similar encoding of the 11 Hz modulation, mostly performed by SAs, whereas, the study shows a different behavior for high frequency encoding of the FAs in the active and passive touch.

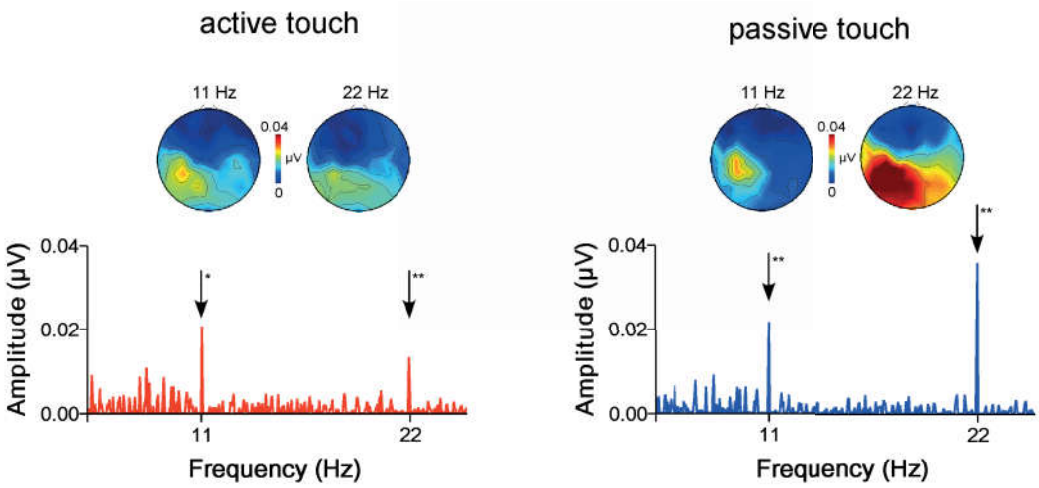

FIGURE B.3: EEG frequency spectrum during active and passive exploration of the right index finger tip across the ultrasonic device with localized tactile feedback under identical conditions. x-axis: frequency (Hz), y-axis: average noise-subtracted amplitude (μV) of the EEG signals recorded from left parietal electrodes. A robust response can be observed at the frequency of stimulation (i.e. 11 Hz) for both conditions, and the different response for the first harmonic stimulation is well visible. The scalp topography shows the topographical distribution of the signal at the expected frequency.

Appendix C

Analysis of Texture vs Position Control Study

A significant main effect is found for the velocity ($F_{2,18} = 44.92$, $p < .001$) on error rate with slow velocity being more accurate (mean = 25, s.d. = 5.05%), then moderate velocity (mean = 29.4, s.d. = 6.38%) and fast velocity (mean = 57, s.d. = 6.71%). Post-hoc comparison confirmed significant differences between fast velocity and both moderate and slow velocities ($p < .0001$), but not between moderate and slow velocity which supports the previously stated **H1** hypothesis. However, this is to be mitigated when considering a specific texture type and/or a specific control technique as will be commented later-on. This result can be explained by the frequency compression of the signal followed by a greater exploration velocity, which leads to smaller temporal bandwidth of the signal.

Repeated-measures ANOVA revealed a significant control × velocity interaction ($F_{2,18} = 9.05$, $p < .001$) on error rate with Texture control being more accurate than Position control for fast velocity (mean = 49.6, s.d = 8.47% for Texture *vs.* mean = 64.4, s.d = 10.1% for Position) and for moderate velocity (mean = 26, s.d = 7.45% for Texture *vs.* mean = 32.8, s.d = 10.37% for Position); while Position control was more accurate for slow velocity (mean = 28.8, s.d = 7.09% for Texture *vs.* mean = 17.2, s.d = 6.9% for Position). Post-hoc tests confirmed that error rate was significantly lower for Texture control than for Position control with fast finger movement velocity ($p < .05$). However,

the differences between Texture and Position control for the slow velocity as well as for the moderate velocity, were not significant. These results partially support **H2**.

Repeated-measures ANOVA also revealed a significant main effect of Textures ($F_{4,36}$ = 4.01, p < .01) on error rate with XL more accurate (mean = 28.66%, s.d. = 7.98%), then M (mean = 31.66, s.d. = 7.92%) followed by L (mean = 34.33, s.d. = 7.57% then F (mean = 38.33, s.d. = 8.5% and XF (mean = 49.33, s.d. = 10.47%). Post-hoc comparisons confirmed a significant difference between the following paires: M and XF, L and XF and XL, XF (p < .01). These results support **H3**.

Besides, it was found a significant control x Textures interaction ($F_{4,36}$ = 23.55, p < .001) on error rate. Post-hoc tests revealed that error rate was significantly lower (70%) for Texture control than for Position for XF, while it was significantly lower (60%) for Position control than for Texture control with XL (p < .001). These results support partially **H4**. In this respect, it was also found a significant velocity × Texture ($F_{8,72}$ = 4.14, p < .001) and control × velocity × Texture interaction ($F_{8,72}$ = 2.28, p < .05) on error rate. Post-hoc comparisons revealed that for fast velocity, Texture control was significantly more accurate than Position control for XF and F textures (p < .01), while Position control was significantly more accurate for XL texture (p < .01). Again, Texture control was significantly more accurate than Position control for XF texture in moderate velocity (p < .01) while Position control was significantly more accurate for M and XL for both moderate and slow velocities (p < .01).

Bibliography

[1] H. Fruhstorfer, U. Abel, C. D. Garthe, and A. Knüttel. Thickness of the stratum corneum of the volar fingertips. *Clinical Anatomy (New York, N.Y.)*, 13(6):429–433, 2000. ISSN 0897-3806. doi: 10.1002/1098-2353(2000)13:6<429::AID-CA6>3.0.CO;2-5.

[2] Julien van Kuilenburg, Marc A. Masen, and Emile van der Heide. Contact modelling of human skin: What value to use for the modulus of elasticity? *Proceedings of the Institution of Mechanical Engineers, Part J: Journal of Engineering Tribology*, 227(4):349–361, April 2013. ISSN 1350-6501, 2041-305X. doi: 10.1177/1350650112463307. URL http://pij.sagepub.com/content/227/4/349.

[3] Teja Vodlak, Zlatko Vidrih, Dusan Fetih, Djordje Peric, and Tomaz Rodic. Development of a finite element model of a finger pad for biomechanics of human tactile sensations. Milano, Italy, 2015. IEEE EMBC. accepted as a technical paper.

[4] 2016. URL http://www.merriam-webster.com.

[5] 2011. URL http://plato.stanford.edu/entries/life/.

[6] Gabriel Robles-De-La-Torre and Vincent Hayward. Force can overcome object geometry in the perception of shape through active touch. *Nature*, 412(6845):445–448, July 2001. ISSN 0028-0836. doi: 10.1038/35086588. URL http://www.nature.com/nature/journal/v412/n6845/abs/412445a0.html.

[7] M. Hollins and S.R. Risner. Evidence for the duplex theory of tactile texture perceptio. *Perception and Psychophysics*, 62(4):695–705, 2000.

[8] Lederman-SJ. Jones, LA. *Human hand function.* Oxford University Press, Inc., 2006.

[9] A. Bicchi, E. P. Scilingo, and D. De Rossi. Haptic discrimination of softness in teleoperation: the role of the contact area spread rate. *IEEE Transactions on Robotics and Automation*, 16(5):496–504, October 2000. ISSN 1042-296X. doi: 10.1109/70.880800.

[10] George A. Gescheider, Stanley J. Bolanowski, Jennifer V. Pope, and Ronald T. Verrillo. A four-channel analysis of the tactile sensitivity of the fingertip: frequency selectivity, spatial summation, and temporal summation. *Somatosensory & Motor Research*, 19(2):114–124, 2002. ISSN 0899-0220. doi: 10.1080/08990220220131505.

[11] V. Hayward. Introduction to haptics. Course notes, UPMC - Paris, 2013.

[12] J. A. McGrath and J. Uitto. Anatomy and Organization of Human Skin. In *Rook's Textbook of Dermatology*, pages 1–53. Wiley-Blackwell, 2010. ISBN 978-1-4443-1763-3. URL http://onlinelibrary.wiley.com/doi/10.1002/9781444317633.ch3/summary.

[13] Ravinder S. Dahiya and Monica Gori. Probing with and into fingerprints. *Journal of Neurophysiology*, 104(1):1–3, July 2010. ISSN 1522-1598. doi: 10.1152/jn.01007.2009.

[14] J. Wessberg. Introduction to microneurography. Course notes, University of Gotheborg, 2013.

[15] Teja Vodlak, Zlatko Vidrih, Primoz Pirih, Presern Skorjanc, Ales, and Tomaz Rodic. Functional microanatomical model of meissner corpuscle from finite element model to mechano-transduction. *Haptics: Neuroscience, Devices, Modeling, and Applications*, 2014.

[16] R. S. Johansson, U. Landstro¨m, and R. Lundstro¨m. Responses of mechanoreceptive afferent units in the glabrous skin of the human hand to sinusoidal skin displacements. *Brain Research*, 244(1):17–25, July 1982. ISSN 0006-8993. doi: 10.1016/0006-8993(82)90899-X. URL http://www.sciencedirect.com/science/article/pii/000689938290899X.

[17] R.S. Johansson and A.B. Vallbo. Tactile sensory coding in the glabrous skin of the human hand. *Trends in Neuroscience*, 6(1):27–32, 1983.

[18] K.O. Johnson and S.S. Hsiao. Neural mechanisms of tactual form and texture perception. *Annual Review of Neuroscience*, 15:227–250, 1992.

[19] K.O. Johnson. The roles and functions of cutaneous mechanoreceptors. *Current Opinion in Neurobiology*, 11(4):455–461, 2001.

[20] A. J. Brisben, S. S. Hsiao, and K. O. Johnson. Detection of vibration transmitted through an object grasped in the hand. *Journal of Neurophysiology*, 81(4):1548–1558, April 1999. ISSN 0022-3077.

[21] George A. Gescheider. *Psychophysics: The Fundamentals*. Psychology Press, 3 edition edition, June 2013.

[22] Alison I. Weber, Hannes P. Saal, Justin D. Lieber, Ju-Wen Cheng, Louise R. Manfredi, John F. Dammann, and Sliman J. Bensmaia. Spatial and temporal codes mediate the tactile perception of natural textures. *Proceedings of the National Academy of Sciences of the United States of America*, 110(42):17107–17112, October 2013. ISSN 0027-8424. doi: 10.1073/pnas.1305509110. URL http://www.ncbi.nlm.nih.gov/pmc/articles/PMC3800989/.

[23] Lisa Skedung, Martin Arvidsson, Jun Young Chung, Christopher M. Stafford, Birgitta Berglund, and Mark W. Rutland. Feeling Small: Exploring the Tactile Perception Limits. *Scientific Reports*, 3, September 2013. ISSN 2045-2322. doi: 10.1038/srep02617. URL http://www.nature.com/articles/srep02617.

[24] Mark Hollins, Sliman Bensmaïa, Kristie Karlof, and Forrest Young. Individual differences in perceptual space for tactile textures: Evidence from multidimensional scaling. *Perception & Psychophysics*, 62(8):1534–1544, December 2000. ISSN 0031-5117, 1532-5962. doi: 10.3758/BF03212154. URL http://link.springer.com/article/10.3758/BF03212154.

[25] Sliman J. BensmaIa and Mark Hollins. The vibrations of texture. *Somatosensory & Motor Research*, 20(1):33–43, 2003. ISSN 0899-0220. doi: 10.1080/0899022031000083825.

[26] Susan J. Lederman. Tactual roughness perception: Spatial and temporal determinants. *Canadian Journal of Psychology/Revue canadienne de psychologie*, 37(4):498–511, 1983. ISSN 0008-4255(Print). doi: 10.1037/h0080750.

[27] null Meftah el M, L. Belingard, and C. E. Chapman. Relative effects of the spatial and temporal characteristics of scanned surfaces on human perception of tactile roughness using passive touch. *Experimental Brain Research*, 132(3):351–361, June 2000. ISSN 0014-4819.

[28] Thierri Callier, Hannes P. Saal, Elizabeth C. Davis-Berg, and Sliman J. Bensmaia. Kinematics of unconstrained tactile texture exploration. *Journal of Neurophysiology*, 113(7):3013–3020, April 2015. ISSN 1522-1598. doi: 10.1152/jn.00703.2014.

[29] M. Wiertlewski, C. Hudin, and V. Hayward. On the 1/f noise and non-integer harmonic decay of the interaction of a finger sliding on flat and sinusoidal surfaces. In *2011 IEEE World Haptics Conference (WHC)*, pages 25–30, June 2011. doi: 10.1109/WHC.2011.5945456.

[30] Michael Wiertlewski, J. Lozada, and V. Hayward. The spatial spectrum of tangential skin displacement can encode tactual texture. *Robotics, IEEE Transactions on*, 27(3):461–472, 2011. ISSN 1552-3098. doi: 10.1109/TRO.2011.2132830.

[31] Lester E. Krueger. David Katz's Der Aufbau der Tastwelt (The world of touch): A synopsis. *Perception & Psychophysics*, 7(6):337–341, November 1970. ISSN 0031-5117, 1532-5962. doi: 10.3758/BF03208659. URL http://link.springer.com/article/10.3758/BF03208659.

[32] Louise R. Manfredi, Hannes P. Saal, Kyler J. Brown, Mark C. Zielinski, John F. Dammann, Vicky S. Polashock, and Sliman J. Bensmaia. Natural scenes in tactile texture. *Journal of Neurophysiology*, 111(9):1792–1802, May 2014. ISSN 0022-3077, 1522-1598. doi: 10.1152/jn.00680.2013. URL http://jn.physiology.org/content/111/9/1792.

[33] Xavier Libouton, Olivier Barbier, Leon Plaghki, and Jean-Louis Thonnard. Tactile roughness discrimination threshold is unrelated to tactile spatial acuity. *Behavioural Brain Research*, 208(2):473–478, April 2010. ISSN 1872-7549. doi: 10.1016/j.bbr.2009.12.017.

[34] Benoit Delhaye, Vincent Hayward, Philippe Lefèvre, and Jean-Louis Thonnard. Texture-induced vibrations in the forearm during tactile exploration. *Frontiers in Behavioral Neuroscience*, 6:37, 2012. ISSN 1662-5153. doi: 10.3389/fnbeh.2012.00037.

[35] Elaine R. Serina, C. D. Mote Jr., and David Rempel. Force response of the fingertip pulp to repeated compression—Effects of loading rate, loading angle and anthropometry. *Journal of Biomechanics*, 30(10):1035–1040, October 1997. ISSN 0021-9290. doi: 10.1016/S0021-9290(97)00065-1. URL http://www.sciencedirect.com/science/article/pii/S0021929097000651.

[36] E. R. Serina, E. Mockensturm, C. D. Mote, and D. Rempel. A structural model of the forced compression of the fingertip pulp. *Journal of Biomechanics*, 31(7): 639–646, July 1998. ISSN 0021-9290.

[37] Todd C. Pataky, Mark L. Latash, and Vladimir M. Zatsiorsky. Viscoelastic response of the finger pad to incremental tangential displacements. *Journal of Biomechanics*, 38(7):1441–1449, July 2005. ISSN 0021-9290. doi: 10.1016/j.jbiomech.2004.07.004.

[38] Qi Wang and Vincent Hayward. In vivo biomechanics of the fingerpad skin under local tangential traction. *Journal of Biomechanics*, 40(4):851–860, 2007. ISSN 0021-9290. doi: 10.1016/j.jbiomech.2006.03.004.

[39] Peter H. Warman and A. Roland Ennos. Fingerprints are unlikely to increase the friction of primate fingerpads. *The Journal of Experimental Biology*, 212(Pt 13): 2016–2022, July 2009. ISSN 0022-0949. doi: 10.1242/jeb.028977.

[40] Michael J. Adams, Simon A. Johnson, Philippe Lefèvre, Vincent Lévesque, Vincent Hayward, Thibaut André, and Jean-Louis Thonnard. Finger pad friction and its role in grip and touch. *Journal of The Royal Society Interface*, 10(80), 2012. ISSN 1742-5689. doi: 10.1098/rsif.2012.0467.

[41] Tabor D. Bowden, F.P. *Friction and lubrication of solids*. Oxford University Press, 1954.

[42] B. J. Briscoe and D. Tabor. Shear Properties of Thin Polymeric Films. *The Journal of Adhesion*, 9(2):145–155, January 1978. ISSN 0021-8464. doi: 10.1080/00218467808075110. URL http://dx.doi.org/10.1080/00218467808075110.

[43] J. A. Greenwood and J. H. Tripp. The Elastic Contact of Rough Spheres. *Journal of Applied Mechanics*, 34(1):153–159, March 1967. ISSN 0021-8936. doi: 10.1115/1.3607616. URL http://dx.doi.org/10.1115/1.3607616.

[44] Thibaut André, Philippe Lefèvre, and Jean-Louis Thonnard. A continuous measure of fingertip friction during precision grip. *Journal of Neuroscience Methods*, 179(2):224–229, May 2009. ISSN 1872-678X. doi: 10.1016/j.jneumeth.2009.01.031.

[45] M. J. Adams, R. McKeown, and A. Whall. A micromechanical model for the confined uni-axial compression of an assembly of elastically deforming spherical particles. *Journal of Physics D: Applied Physics*, 30(5):912, 1997. ISSN 0022-3727. doi: 10.1088/0022-3727/30/5/025. URL http://stacks.iop.org/0022-3727/30/i=5/a=025.

[46] A. M. Smith and S. H. Scott. Subjective scaling of smooth surface friction. *Journal of Neurophysiology*, 75(5):1957–1962, May 1996. ISSN 0022-3077.

[47] T. André, P. Lefèvre, and J.-L. Thonnard. Fingertip moisture is optimally modulated during object manipulation. *Journal of Neurophysiology*, 103(1):402–408, January 2010. ISSN 1522-1598. doi: 10.1152/jn.00901.2009.

[48] Subrahmanyam M. Pasumarty, Simon A. Johnson, Simon A. Watson, and Michael J. Adams. Friction of the Human Finger Pad: Influence of Moisture, Occlusion and Velocity. *Tribology Letters*, 44(2):117–137, August 2011. ISSN 1023-8883, 1573-2711. doi: 10.1007/s11249-011-9828-0. URL http://link.springer.com/article/10.1007/s11249-011-9828-0.

[49] M. J. Adams, B. J. Briscoe, and S. A. Johnson. Friction and lubrication of human skin. *Tribology Letters*, 26(3):239–253, March 2007. ISSN 1023-8883, 1573-2711. doi: 10.1007/s11249-007-9206-0. URL http://link.springer.com/article/10.1007/s11249-007-9206-0.

[50] S. A. Johnson, D. M. Gorman, M. J. Adams, and B. J. Briscoe. The friction and lubrication of human stratum corneum. In M. Godet and G. Dalmaz C. M. Taylor D. Dowson, T. H. C. Childs, editor, *Tribology Series*, volume 25 of *Thin Films in TribologyProceedings of the 19th Leeds-Lyon Symposium on Tribology held at the Institute of Tribology, University of Leeds*, pages 663–672. Elsevier, 1993. URL http://www.sciencedirect.com/science/article/pii/S016789220870419X.

[51] A. Schallamach. A theory of dynamic rubber friction. *Wear*, 6(5):375–382, September 1963. ISSN 0043-1648. doi: 10.1016/0043-1648(63)90206-0. URL http://www.sciencedirect.com/science/article/pii/0043164863902060.

[52] T. Watanabe and S. Fukui. A method for controlling tactile sensation of surface roughness using ultrasonic vibration. In *, 1995 IEEE International Conference on Robotics and Automation, 1995. Proceedings*, volume 1, pages 1134–1139 vol.1, May 1995. doi: 10.1109/ROBOT.1995.525433.

[53] Mélisande Biet, Frédéric Giraud, and Betty Lemaire-Semail. Squeeze film effect for the design of an ultrasonic tactile plate. *IEEE Transactions on Ultrasonics, Ferroelectrics and Frequency Control*, 54(12):2678–2688, 2007. doi: 10.1109/TUFFC.2007.596.

[54] Christophe Winter. *Friction Feedback Actuators Using Squeeze Film Effect*. PhD thesis, Ecole Polytechnique Federale de Lausanne, 2014.

[55] L. Winfield, J. Glassmire, J.E. Colgate, and M. Peshkin. T-pad: Tactile pattern display through variable friction reduction. In *EuroHaptics Conference, 2007 and Symposium on Haptic Interfaces for Virtual Environment and Teleoperator Systems. World Haptics 2007. Second Joint*, pages 421–426, 2007. doi: 10.1109/WHC.2007.105.

[56] Michel Amberg, Frédéric Giraud, Betty Semail, Paolo Olivo, Géry Casiez, and Nicolas Roussel. STIMTAC: A Tactile Input Device with Programmable Friction. In *Proceedings of the 24th Annual ACM Symposium Adjunct on User Interface Software and Technology*, UIST '11 Adjunct, pages 7–8, New York, NY, USA, 2011. ACM. ISBN 978-1-4503-1014-7. doi: 10.1145/2046396.2046401. URL http://doi.acm.org/10.1145/2046396.2046401.

[57] M. Biet, G. Casiez, F. Giraud, and B. Lemaire-Semail. Discrimination of Virtual Square Gratings by Dynamic Touch on Friction Based Tactile Displays. In *symposium on Haptic interfaces for virtual environment and teleoperator systems, 2008. haptics 2008*, pages 41–48, March 2008. doi: 10.1109/HAPTICS.2008.4479912.

[58] F. Casset, JS. Danel, P. Renaux, C. Chappaz, F. Bernard, T. Sednaoui, S. Basrour, B. Desloges, and S. Fanget. 4-inch transparent plates based on thin-film aln actuators for haptic applications. *Mechatronics*, pages –, 2016. ISSN 0957-4158. doi: http://dx.doi.org/10.1016/j.mechatronics.2016.05.014. URL http://www.sciencedirect.com/science/article/pii/S0957415816300538.

[59] R. Gassert, R. Moser, E. Burdet, and H. Bleuler. Mri/fmri-compatible robotic system with force feedback for interaction with human motion. *IEEE/ASME Transactions on Mechatronics*, 11(2):216–224, April 2006. ISSN 1083-4435. doi: 10.1109/TMECH.2006.871897.

[60] M. Biet, F. Giraud, and B. Lemaire-Semail. Squeeze film effect for the design of an ultrasonic tactile plate. *IEEE Transactions on Ultrasonics, Ferroelectrics, and Frequency Control*, 54(12):2678–2688, December 2007. ISSN 0885-3010. doi: 10.1109/TUFFC.2007.596.

[61] W. Ben Messaoud, M. Amberg, B. Lemaire-Semail, F. Giraud, and M. A. Bueno. High fidelity closed loop controlled friction in SMARTTAC tactile stimulator. In *2015 17th European Conference on Power Electronics and Applications (EPE'15 ECCE-Europe)*, pages 1–9, September 2015. doi: 10.1109/EPE.2015.7309191.

[62] Wael Ben Messaoud, Betty Lemaire-Semail, Marie-Ange Bueno, Michel Amberg, and Frédéric Giraud. Closed-Loop Control for Squeeze Film Effect in Tactile Stimulator. *ACTUATOR 2014*.

[63] Rebecca Fenton Friesen, Michael Wiertlewski, Michael A. Peshkin, and J. Edward Colgate. Bioinspired artificial fingertips that exhibit friction reduction when subjected to transverse ultrasonic vibrations. *IEEE - World Haptics Conference 2015*, .

[64] Xiaowei Dai, J.E. Colgate, and M.A. Peshkin. LateralPaD: A surface-haptic device that produces lateral forces on a bare finger. In *2012 IEEE Haptics Symposium (HAPTICS)*, pages 7–14, March 2012. doi: 10.1109/HAPTIC.2012.6183753.

[65] G. Imokawa, S. Akasaki, Y. Minematsu, and M. Kawai. Importance of intercellular lipids in water-retention properties of the stratum corneum: induction and recovery study of surfactant dry skin. *Archives of Dermatological Research*, 281 (1):45–51, February 1989. ISSN 0340-3696, 1432-069X. doi: 10.1007/BF00424272. URL http://link.springer.com/article/10.1007/BF00424272.

[66] Genji Imokawa and Michihiro Hattori. A Possible Function of Structural Lipids in the Water-Holding Properties of the Stratum Corneum. *Journal of Investigative Dermatology*, 84(4):282–284, April 1985. ISSN 0022-202X. doi: 10.

1111/1523-1747.ep12265365. URL http://www.nature.com/jid/journal/v84/n4/abs/5614640a.html.

[67] Thomas Sednaoui, Eric Vezzoli, Brygida Maria Dzidek, Betty Lemaire-Semail, Cedric Chiappaz, and Michael Adams. Experimental evaluation of friction reduction in ultrasonic devices. In *World Haptics Conference (WHC)*, 2015.

[68] Ted Belytschko, Jame Shau-Jen Ong, Wing Kam Liu, and James M. Kennedy. Hourglass control in linear and nonlinear problems. *Computer Methods in Applied Mechanics and Engineering*, 43(3):251–276, May 1984. ISSN 0045-7825. doi: 10.1016/0045-7825(84)90067-7. URL http://www.sciencedirect.com/science/article/pii/0045782584900677.

[69] Peter Wriggers. *Computational Contact Mechanics*. Springer Berlin Heidelberg, Berlin, Heidelberg, 2006. ISBN 978-3-540-32608-3 978-3-540-32609-0. URL http://link.springer.com/10.1007/978-3-540-32609-0.

[70] K. L. Johnson and Kenneth Langstreth Johnson. *Contact Mechanics*. Cambridge University Press, August 1987. ISBN 978-0-521-34796-9.

[71] Brygida Maria Dzidek, Michael Adams, Zhibing Zhang, Simon Johnson, Séréna Bochereau, and Vincent Hayward. Role of occlusion in non-coulombic slip of the finger pad. In Malika Auvray and Christian Duriez, editors, *Haptics: Neuroscience, Devices, Modeling, and Applications*, volume 8618 of *Lecture Notes in Computer Science*, pages 109–116. Springer Berlin Heidelberg, 2014. ISBN 978-3-662-44192-3. doi: 10.1007/978-3-662-44193-0_15.

[72] Daniel R. Einstein, Alan D. Freed, Nielen Stander, Bahar Fata, and Ivan Vesely. Inverse Parameter Fitting of Biological Tissues: A Response Surface Approach. *Annals of Biomedical Engineering*, 33(12):1819–1830, December 2005. ISSN 0090-6964, 1573-9686. doi: 10.1007/s10439-005-8338-3. URL http://link.springer.com/article/10.1007/s10439-005-8338-3.

[73] Fulin Lei and A. Z. Szeri. Inverse analysis of constitutive models: Biological soft tissues. *Journal of Biomechanics*, 40(4):936–940, 2007. ISSN 0021-9290. doi: 10.1016/j.jbiomech.2006.03.014. URL http://www.sciencedirect.com/science/article/pii/S0021929006001059.

[74] Albert Tarantola. *Inverse Problem Theory and Methods for Model Parameter Estimation*. SIAM, 2005. ISBN 978-0-89871-792-1.

[75] Rebecca Fenton Friesen, Michael Wiertlewski, and J. Edward Colgate. The Role of Damping in Ultrasonic Friction Reduction. *IEEE - Haptic Simposium 2016*, .

[76] Michael Wiertlewski and Vincent Hayward. Mechanical behavior of the fingertip in the range of frequencies and displacements relevant to touch. *Journal of Biomechanics*, 45(11):1869–1874, 2012. ISSN 0021-9290. doi: http://dx.doi.org/10.1016/j.jbiomech.2012.05.045.

[77] Eric Vezzoli, Brygida Maria Dzidek, Thomas Sednaoui, Frédéric Giraud, Michael Adams, and Betty Lemaire-Semail. Role of Fingerprint Mechanics and non-Coulombic Friction in Ultrasonic Devices. *WHC 2015*.

[78] Brygida Maria Dzidek, Michael Adams, Zhibing Zhang, Simon Johnson, Séréna Bochereau, and Vincent Hayward. Role of Occlusion in Non-Coulombic Slip of the Finger Pad. In Malika Auvray and Christian Duriez, editors, *Haptics: Neuroscience, Devices, Modeling, and Applications*, Lecture Notes in Computer Science, pages 109–116. Springer Berlin Heidelberg, January 2014. ISBN 978-3-662-44192-3, 978-3-662-44193-0. URL http://link.springer.com/chapter/10.1007/978-3-662-44193-0_15.

[79] Zhihong Huang, Margaret Lucas, and Michael J. Adams. Influence of ultrasonics on upsetting of a model paste. *Ultrasonics*, 40(1-8):43–48, May 2002. ISSN 0041624X. doi: 10.1016/S0041-624X(02)00245-7. URL http://linkinghub.elsevier.com/retrieve/pii/S0041624X02002457.

[80] Y. M. Huang, Y. S. Wu, and J. Y. Huang. The influence of ultrasonic vibration-assisted micro-deep drawing process. *The International Journal of Advanced Manufacturing Technology*, 71(5-8):1455–1461, January 2014. ISSN 0268-3768, 1433-3015. doi: 10.1007/s00170-013-5553-1. URL http://link.springer.com/article/10.1007/s00170-013-5553-1.

[81] Edward Mallinckrodt, A. L, and William Sleator Jr. Perception by the skin of electrically induced vibrations. *Science*, 118:277–278, 1953. ISSN 0036-8075(Print). doi: 10.1126/science.118.3062.277.

[82] K.A. Kaczmarek, K. Nammi, A.K. Agarwal, M.E. Tyler, S.J. Haase, and D.J. Beebe. Polarity Effect in Electrovibration for Tactile Display. *IEEE Transactions on Biomedical Engineering*, 53(10):2047–2054, October 2006. ISSN 0018-9294. doi: 10.1109/TBME.2006.881804.

[83] Olivier Bau, Ivan Poupyrev, Ali Israr, and Chris Harrison. TeslaTouch: Electrovibration for Touch Surfaces. In *Proceedings of the 23Nd Annual ACM Symposium on User Interface Software and Technology*, UIST '10, pages 283–292, New York, NY, USA, 2010. ACM. ISBN 978-1-4503-0271-5. doi: 10.1145/1866029.1866074. URL http://doi.acm.org/10.1145/1866029.1866074.

[84] F. Giraud, M. Amberg, and B. Lemaire-Semail. Merging two tactile stimulation principles: electrovibration and squeeze film effect. In *World Haptics Conference (WHC), 2013*, pages 199–203, April 2013. doi: 10.1109/WHC.2013.6548408.

[85] H. Kim, J. Kang, Ki-Duk Kim, Kyoung-Moon Lim, and J. Ryu. Method for Providing Electrovibration with Uniform Intensity. *IEEE Transactions on Haptics*, PP(99):1–1, 2015. ISSN 1939-1412. doi: 10.1109/TOH.2015.2476810.

[86] D.J. Meyer, M.A. Peshkin, and J.E. Colgate. Fingertip friction modulation due to electrostatic attraction. In *World Haptics Conference (WHC), 2013*, pages 43–48, April 2013. doi: 10.1109/WHC.2013.6548382.

[87] R.M. Strong and D. Troxel. An electrotactile display. *Man-Machine Systems, IEEE Transactions on*, 11(1):72–79, 1970. ISSN 0536-1540. doi: 10.1109/TMMS.1970.299965.

[88] Tatsuma Yamamoto and Yoshitake Yamamoto. Electrical properties of the epidermal stratum corneum. *Medical and biological engineering*, 14(2):151–158, March 1976. ISSN 0025-696X, 1741-0444. doi: 10.1007/BF02478741. URL http://link.springer.com/article/10.1007/BF02478741.

[89] H. Fruhstorfer, U. Abel, C.-D. Garthe, and A. Knüttel. Thickness of the stratum corneum of the volar fingertips. *Clinical Anatomy*, 13(6):429–433, 2000. ISSN 1098-2353. doi: 10.1002/1098-2353(2000)13:6<429::AID-CA6>3.0.CO;2-5.

[90] David J. Meyer, Michael A Peshkin, and J E Colgate. Fingertip friction modulation due to electrostatic attraction. In *World Haptics Conference (WHC), 2013*, pages 43–48, 2013. doi: 10.1109/WHC.2013.6548382.

[91] Damijan Miklavcic, Natasa Pavselj, and Francis X. Hart. *Electric Properties of Tissues*. John Wiley & Sons, Inc., 2006. doi: 10.1002/9780471740360.ebs0403.

[92] Teja Vodlak, Zlatko Vidrih, Primoz Pirih, Ales Skorjanc, Janez Presern, and Tomaz Rodic. Functional microanatomical model of meissner corpuscle. In Malika Auvray and Christian Duriez, editors, *Haptics: Neuroscience, Devices, Modeling, and Applications*, volume 8619 of *Lecture Notes in Computer Science*, pages 377–384. Springer Berlin Heidelberg, 2014. ISBN 978-3-662-44195-4. doi: 10.1007/978-3-662-44196-1_46.

[93] D.D. Somer, D. Perić, E.A. de Souza Neto, and W.G. Dettmer. A multi-scale computational assessment of channel gating assumptions within the meissner corpuscle. *Journal of Biomechanics*, 48(1):73–80, 2015. ISSN 0021-9290. doi: 10.1016/j.jbiomech.2014.11.003.

[94] Daine R Lesniak and Gregory J Gerling. Predicting sa-i mechanoreceptor spike times with a skin-neuron model. *Mathematical biosciences*, 220(1):15–23, 2009.

[95] R.J. Lapeer, P.D. Gasson, and V. Karri. Simulating plastic surgery: From human skin tensile tests, through hyperelastic finite element models to real-time haptics. *Progress in Biophysics and Molecular Biology*, 103(2–3):208–216, 2010. ISSN 0079-6107. doi: http://dx.doi.org/10.1016/j.pbiomolbio.2010.09.013. Special Issue on Biomechanical Modelling of Soft Tissue Motion.

[96] Y.C. Fung. *Biomechanics: Mechanical Properties of Living Tissues*. Biomechanics. Springer New York, 1993. ISBN 9780387979472.

[97] EA de Souza Neto, D Peric, M Dutko, and DRJ Owen. Design of simple low order finite elements for large strain analysis of nearly incompressible solids. *International Journal of Solids and Structures*, 33(20-22):3277–3296, 1996.

[98] K.A. Kaczmarek, K. Nammi, A.K. Agarwal, M.E. Tyler, S.J. Haase, and D.J. Beebe. Polarity effect in electrovibration for tactile display. *Biomedical Engineering, IEEE Transactions on*, 53(10):2047–2054, 2006. ISSN 0018-9294. doi: 10.1109/TBME.2006.881804.

[99] Zoran Radivojevic, Paul Beecher, Chris Bower, Darryl Cotton, Samiul Haque, Piers Andrew, Brian Henson, Stephen A. Wall, Ian S. Howard, James N. Ingram, Daniel M. Wolpert, Antti O. Salo, and Tom Xue. 31.1: Invited paper: Programmable electrostatic surface for tactile perceptions. *SID Symposium Digest of Technical Papers*, 43(1):407–410, 2012. ISSN 2168-0159. doi: 10.1002/j.2168-0159.2012.tb05802.x.

[100] M.C. Hegg and A.V. Mamishev. Influence of variable plate separation on fringing electric fields in parallel-plate capacitors. In *Electrical Insulation, 2004. Conference Record of the 2004 IEEE International Symposium on*, pages 384–387, 2004. doi: 10.1109/ELINSL.2004.1380606.

[101] MATLAB. *version 8.2 (R2013b)*. The MathWorks Inc., Natick, Massachusetts, 2013.

[102] M. D. McKay, R. J. Beckman, and W. J. Conover. A comparison of three methods for selecting values of input variables in the analysis of output from a computer code. *Technometrics*, 21(2):239–245, 1979. doi: 10.2307/1268522.

[103] Randall D. Manteufel. *Evaluating the convergence of Latin Hypercube Sampling*. American Institute of Aeronautics and Astronautics, 2000. doi: doi:10.2514/6.2000-1636.

[104] M Vořechovskỳ and D Novák. Statistical correlation in stratified sampling. *Proc. of 9th Int. Conf. on Applications of Statistics and Probability in Civil Engineering–ICASP*, 9:119–124, 2003.

[105] Matjaz Dolsek. Incremental dynamic analysis with consideration of modeling uncertainties. *Earthquake Engineering and Structural Dynamics*, 38(6):805–825, 2009. ISSN 1096-9845. doi: 10.1002/eqe.869.

[106] Eric Vezzoli, Michel Amberg, Frédéric Giraud, and Betty Lemaire-Semail. Electrovibration Modeling Analysis. In Malika Auvray and Christian Duriez, editors, *Haptics: Neuroscience, Devices, Modeling, and Applications*, Lecture Notes in Computer Science, pages 369–376. Springer Berlin Heidelberg, January 2014. ISBN 978-3-662-44195-4, 978-3-662-44196-1. URL http://link.springer.com/chapter/10.1007/978-3-662-44196-1_45.

[107] Michael Wiertlewski and Vincent Hayward. Mechanical behavior of the fingertip in the range of frequencies and displacements relevant to touch. *Journal of Biomechanics*, 45(11):1869–1874, July 2012. ISSN 0021-9290. doi: 10.1016/j.jbiomech.2012.05.045. URL http://www.sciencedirect.com/science/article/pii/S0021929012003260.

[108] Michael Wiertlewski, J. Lozada, and V. Hayward. The Spatial Spectrum of Tangential Skin Displacement Can Encode Tactual Texture. *IEEE Transactions on Robotics*, 27(3):461–472, June 2011. ISSN 1552-3098. doi: 10.1109/TRO.2011.2132830.

[109] Seung-Chan Kim, Ali Israr, and Ivan Poupyrev. Tactile rendering of 3d features on touch surfaces. In *Proceedings of the 26th Annual ACM Symposium on User Interface Software and Technology*, UIST '13, pages 531–538, New York, NY, USA, 2013. ACM. ISBN 978-1-4503-2268-3. doi: 10.1145/2501988.2502020.

[110] J. M. Romano and K. J. Kuchenbecker. Creating realistic virtual textures from contact acceleration data. *IEEE T Haptics*, 5(2):109–119, 2012. doi: 10.1109/TOH.2011.38.

[111] H. Culbertson, J. M. Romano, P. Castillo, M. Mintz, and K. J. Kuchenbecker. Refined methods for creating realistic haptic virtual textures from tool-mediated contact acceleration data. In *Haptics Symposium (HAPTICS), 2012 IEEE*, pages 385–391, 2012. doi: 10.1109/HAPTIC.2012.6183819.

[112] H. Culbertson, J.J. Lopez Delgado, and K.J. Kuchenbecker. One hundred data-driven haptic texture models and open-source methods for rendering on 3d objects. In *Haptics Symposium (HAPTICS), 2014 IEEE*, pages 319–325, Feb 2014. doi: 10.1109/HAPTICS.2014.6775475.

[113] Z. Vidrih and E. Vezzoli. Electrovibration signal design: A simulative approac. *Eurohaptics*, 2016.

[114] 2016. URL www.haptictexture.com.

[115] S.J. Bolanowski Jr, G.A. Gescheider, R.T. Verrillo, and C.M Checkosky. Four chan- nels mediate the mechanical aspects of touch. *The Journal of the Acoustical society of America*, 84(1680), 1988.

[116] Michael Wiertlewski, Daniele Leonardis, David J. Meyer, Michael A. Peshkin, and J. Edward Colgate. A High-Fidelity Surface-Haptic Device for Texture Rendering on Bare Finger.

[117] Roberta L. Klatzky and Susan J. Lederman. Touch. In *Handbook of Psychology*. John Wiley & Sons, Inc., 2003. ISBN 978-0-471-26438-5. URL http://onlinelibrary.wiley.com/doi/10.1002/0471264385.wei0406/abstract.

[118] David J. Meyer, Michael A. Peshkin, and J. Edward Colgate. Modeling and Synthesis of Tactile Texture with Spatial Spectrograms for Display on Variable Friction Surfaces. *IEEE - World Haptics Conference 2015*.

[119] K. O. Johnson, T. Yoshioka, and F. Vega-Bermudez. Tactile functions of mechanoreceptive afferents innervating the hand. *Journal of Clinical Neurophysiology: Official Publication of the American Electroencephalographic Society*, 17(6): 539–558, November 2000. ISSN 0736-0258.

[120] A. B. Vallbo and R. S. Johansson. Properties of cutaneous mechanoreceptors in the human hand related to touch sensation. *Human Neurobiology*, 3(1):3–14, 1984. ISSN 0721-9075.

[121] Roland S. Johansson and Ingvars Birznieks. First spikes in ensembles of human tactile afferents code complex spatial fingertip events. *Nature Neuroscience*, 7 (2):170–177, February 2004. ISSN 1097-6256. doi: 10.1038/nn1177. URL http://www.nature.com/neuro/journal/v7/n2/full/nn1177.html.

[122] A. Moungou, E. Vezzoli, C. Lombart, B. Lemaire-Semail, J. L. Thonnard, and A. Mouraux. A novel method using EEG to characterize the cortical processes involved in active and passive touch. In *2016 IEEE Haptics Symposium (HAPTICS)*, pages 205–210, April 2016. doi: 10.1109/HAPTICS.2016.7463178.